Improved prediction of 3D flows at structures

Y Gasowski
A J Cooper

Report SR 544
July 1999

HR Wallingford

Address and Registered Office: HR Wallingford Ltd. Howbery Park, Wallingford, OXON OX10 8BA
Tel: +44 (0) 1491 835381 Fax: +44 (0) 1491 832233

Contract

This report describes work funded by the Construction Directorate of the Department of the Environment, Transport and the Regions, DETR, under Research Contract CI 39/5/114(CC1417) for which the DETR nominated officer was Mr P B Woodhead and the HR Wallingford nominated officer was Dr S W Huntington. The HR Wallingford job number was DFS 0413. This report is published on behalf of DETR, but any opinions expressed in it are not necessarily those of the funding department. The work was carried out by Y Gasowski and A J Cooper of the Ports and Estuaries Group at HR Wallingford.

Prepared by ......AJ Cooper...... *(name)*

......Section Manager...... *(Title)*

Approved by ...... *(name)*

...... *(Title)*

Date ...23 July 1999...

Summary

Improved prediction of 3D flows at structures

Y Gasowski
A J Cooper

Report SR 544
July 1999

In determining the impact of proposed engineering works at estuary and coastal sites it is necessary to determine the flows around structures (such as training walls, breakwaters and groynes). At present two-dimensional depth-integrated numerical flow models are often employed in preliminary design studies associated with such structures. However, in the presence of a structure the flow may be three-dimensional, with a significant vertical variation in the velocity. In the presence of waves the flow becomes even more complex as breaking waves can drive currents. Presently physical models are employed to determine the impact of such works at the design stage. However a numerical modelling approach may prove to be more cost-effective for such studies.

The present project has combined state-of-the-art wave and flow prediction techniques, using both finite difference and finite element modelling technologies, with the aim being to define the range of studies that might presently be undertaken using numerical modelling techniques. The models have been applied to the following test situations:

- a straight channel with a groyne projecting into the flow. A comparison of 2D and 3D flow modelling techniques is made

- a training wall in an estuary where a gyre has been observed at certain stages of the tide

- a straight beach, tested in the laboratory, where breaking waves create set-up and an undertow current

- a beach including a detached breakwater, behind which breaking wave stresses give rise to a recirculation

- beach cusps, investigated in the UK Coastal Research Facility, that give rise to rip currents in between the cusps

For the flow-only test cases, with no waves, it is found that a two-dimensional depth-integrated model can give very good results, except in the very close vicinity of the structure. For the straight beach the three-dimensional flow modelling can predict well the undertow phenomenon and for the cases with structures in a wave field, two-dimensional modelling again gives good results within the area where the waves have broken.

Summary *continued*

It is considered that state-of-the-art numerical models, sufficiently calibrated by comparison with laboratory and site data, can be used predictively for all of these situations (except in the very close vicinity of the structures).

Contents

Contents continued

Figures

Contents continued

1. INTRODUCTION

1.1 Background

In determining the impact of proposed engineering works at estuary and coastal sites it is necessary to determine the flows around the structures which occur at such sites (such as training walls, breakwaters and groynes). At present two-dimensional depth-integrated numerical flow models are often employed in preliminary design studies associated with such structures. However, in the presence of a structure the flow may be three-dimensional, with a significant vertical variation in the velocity. In the presence of waves the flow becomes even more complex as breaking waves can drive currents. Presently physical models are employed to determine the impact of such works at the design stage. However a numerical modelling approach may prove to be more cost-effective for such studies.

The present study may be seen as continuing and extending earlier DoE/DETR supported studies in the applicability of 3D models (Seed 1997, Spaliviero and Seed 1998) that focused on the modelling of fluvial structures. As in the case of that study the report is intended to be of value to researchers working in the area of flows at structures, as well as being of interest to practising engineers wanting to model such situations. They will benefit from the experience we have gained in applying and developing the modelling tools and from the comparing and contrasting of modelling techniques.

The present project has combined state-of-the-art wave and flow prediction techniques, using both finite difference and finite element modelling technologies, with the aim being to define the range of studies that might presently be undertaken using numerical modelling techniques.

1.2 Objectives

The objectives of the study were as follows:

1 A review of the theoretical aspects of the processes to be studied, especially wave phenomena and breaking, and how they are formulated mathematically has been carried out. This contains the present state of knowledge of the subject.

2 In order to test out the effectiveness of the models and to choose between different model formulations of the processes, it was necessary to select experimental data for model testing.

3 The models used were adapted and developed as required to be able to simulate the observed data with different modelling and process formulations.

4 The models were tested in comparison with the observed data and conclusions drawn about the appropriateness of different model and process formulations.

1.3 Report structure

The report is structured as follows:

Chapter 2 covers theoretical aspects of the processes to be studied especially wave phenomena and breaking. The purpose of this chapter is to describe the present state of knowledge of the processes and the mathematical formulations of the processes that are specific to wave-induced flows and flows at structures. The information is used in the modelling activities described in Chapter 4 below.

Chapter 3 describes the experiments with which the models have been compared. The effectiveness of different modelling techniques must be established, at least in part, by comparison with experiments. These are generally carried out in the laboratory (i e they are physical models) because wave conditions in the field are very variable, in space and time. It is widely believed that models must be able to reproduce adequately the results of such controlled experiments before they can be applied to actual engineering conditions with confidence.

In selecting suitable test cases to model the following factors were considered:

- coverage of a range of conditions (river structure, estuary structure, beach etc)
- availability of adequate standard data (prototype or experimental)
- availability of alternative numerical model simulations
- relevance to practical situations

The following five test cases were chosen for examination:

- a straight channel with a groyne projecting into the flow. A comparison of 2D and 3D flow modelling techniques is made

- a training wall in an estuary where a gyre has been observed at certain stages of the tide

- a straight beach, tested in the laboratory, where breaking waves create set-up and an undertow current

- a beach including a detached breakwater, behind which breaking wave stresses give rise to a recirculation

- beach cusps, investigated in the UK Coastal Research Facility, that give rise to rip currents in between the cusps

The model testing and comparison with experimental data have been carried out:

- to see whether the numerical models are able to represent the phenomena to a satisfactory level of accuracy
- to test whether 2D or 3D modelling is adequate for different situations
- to investigate the effects of different representations (e g of radiation stress terms)

The comparisons between the model predictions and observations are described in Chapter 4. In this way the preferred modelling formulations and techniques are inferred.

Chapter 5 contains a summary of the results and the conclusions of the study.

The numerical models used in the study are described in the Appendix.

2. THEORETICAL BACKGROUND

The purpose of the present chapter is to describe the present state of knowledge of the processes and equations that are specific to wave-induced flows and flows at structures. The information is used in the modelling activities described in Chapter 4 below.

In the present study the effects of waves on structures are modelled in a time-averaged (over the wave period) way. Therefore, rather than a single model that models all of the details of the wave motion and computes at the same time the resulting flow, separate wave and flow models are used. The effects of the breaking waves are incorporated into the flow model by calculating in the wave model the breaking wave stresses (called "radiation stresses"), which produce:

- wave set-up on a beach
- longshore currents
- rip currents
- circulating flows behind structures.

The methods that can be used for modelling the effects of the wave radiation stresses are described in sections 2.4.1 to 2.4.3.

In the present chapter the equations and processes involved in the wave modelling will be described, followed by a presentation of the wave breaking processes and the computation of the radiation stress. This is followed by information about the viscosity and friction that are produced as a result of wave breaking and may be incorporated into the flow model, and a description of turbulence models used to prescribe the viscosity coefficients in the flow modelling.

2.1 Wave equations

The starting point for many wave models is the mild slope (or Berkhoff's) equation. This equation can incorporate the effects of reflection, diffraction, shoaling and refraction (these processes are described below in section 2.2) and can be extended to include the effects of refraction by currents. The equation is based on linearity of the wave height, so wave-breaking phenomena need to be studied by incorporating extra terms in the equation (described in section 2.3).

The simplifying assumptions required for the mild slope equation are the following:

- The fluid is assumed to be perfect (inviscid fluid)
- The flow is considered as irrotational
- Waves are not steep: H/L<<1 (wave height over wave length)
- The bottom gradient is in the order of magnitude lower than h/L (depth over wave length)

Under these conditions the mild slope equation takes the form:

$$\nabla\left(CC_g\nabla\Phi\right)+\omega^2\frac{C_g}{C}\Phi=0$$

It is considered useful to present the available mild slope equation based model that takes into account wave-current interaction. Three models are described in this chapter.

Booij (1981):

$$\frac{D^2\Phi}{Dt^2}+(\nabla.U)\frac{D\Phi}{Dt}+\Phi\frac{D}{Dt}(\nabla.U)-\nabla.\left(CC_g\nabla\Phi\right)+\left(\sigma^2-k^2CC_g\right)\Phi=0 \qquad [1]$$

Liu (1983)

$$\frac{D^2\Phi}{Dt^2} - \nabla\left(CC_g\nabla\Phi\right) + \left(\sigma^2 - k^2CC_g\right)\Phi = 0 \qquad [2]$$

Kirby (1984)

$$\frac{D^2\Phi}{Dt^2} + (\nabla.U)\frac{D\Phi}{Dt} - \nabla\left(CC_g\nabla\Phi\right) + \left(\sigma^2 - k^2CC_g\right)\Phi = 0 \qquad [3]$$

where Φ is the velocity potential
ω is the wave angular frequency
k is the wave number
$C = \omega/k$ is the phase velocity
$\sigma^2 = gk \tanh(kh) = \omega_r$ is the relative frequency
$C_g = \partial\omega/\partial k$ is the group velocity

If we consider periodic monochromatic waves of frequency ω, we can write:
$\Phi = \varphi \exp(-i\omega t)$

The last equation [3] becomes

$$\nabla(CC_g\nabla\varphi) + 2\omega iU\nabla\varphi - U.\nabla(U\nabla\varphi) - (\nabla.U)(U.\nabla\varphi) + (k^2CC_g - \sigma^2 + \omega^2 + i\omega\nabla.U)\varphi = 0 \qquad [4]$$

Considering realistic cases where the current speed is smaller than the phase velocity and the group velocity:

$O(CC_g/|U|^2) >> 1$

Then the previous equation can be simplified as:

$$\nabla(CC_g\nabla\varphi) + 2Ui\omega\nabla\varphi + (k^2CC_g - \sigma^2 + \omega^2 + i\omega\nabla.U)\varphi = 0 \qquad [5]$$

Kostense et al (1988) applied Kirby's equation (1984), (a time-dependent mild slope equation), to some situations involving wave/current interaction. It was shown that this extended equation gave fairly good results and that the effects of diffraction, bottom refraction, current refraction, reflection and dissipation were successfully integrated.

In the ARTEMIS wave model (for details see Appendix), the current is not taken into account. However a term for the energy dissipation due to the breaking is added. The modified equation then becomes:

$$\nabla(CC_g\nabla\varphi) + CC_g\left(k^2 + ik\mu\right)\varphi = 0 \qquad [6]$$

μ = dissipation coefficient
W =dissipation function

with $\mu = \dfrac{W}{\left(CC_g\right)^{1/2}}$

For example the dissipation due to friction in ARTEMIS is:

$$W = \frac{1}{2} f_W \frac{1}{h} \frac{1}{\cosh(kh)^2} U_e \qquad [7]$$

f_W: friction coefficient
U_e: effective wave velocity at the surface

This frictional dissipation term can be added to the current-only friction in the flow modelling. For further details see sections 2.3.3 and 2.3.4

2.2 Wave transformation phenomena

The wave transformation processes of diffraction, refraction, shoaling and reflection will be described in the next four subsections.

2.2.1 Diffraction

Diffraction is the term that refers to wave phenomena that cause energy to travel in directions different to that of the wave rays. A common example of diffraction is the bending of waves around obstacles, so that wave energy is propagated to points lying within geometrical shadows. This is of importance in considering the passage of waves behind breakwaters or through narrow openings into harbours.

What happens when waves pass through an opening between breakwaters depends on the ratio of the width of the opening to the wavelength. When the opening is wide compared to the wavelength, the waves tend to pass straight through, diffracting only slightly outwards as they proceed (see the first figure below). With waves of long wavelength compared to the width of the opening, however the behaviour is different. They tend to spread out in all directions as circular waves centred on the opening (as in the second figure below). In the first case the amplitude of the wave decreases only slightly in the forward direction, whereas in the second the energy is spread almost evenly over the entire semicircle and the amplitude decreases more rapidly in all directions as we proceed further from the opening.

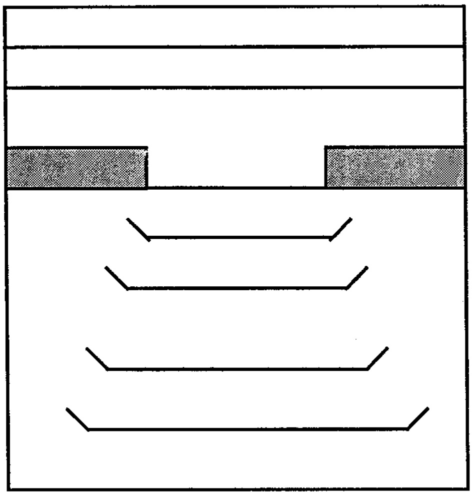

Opening is wide compared to wavelength

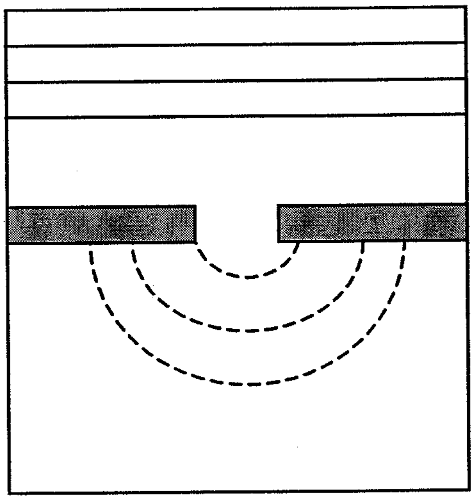

Opening is narrow compared to wavelength

2.2.2 Refraction

a) Wave refraction by depth

Waves are said to refract when the direction in which they are moving changes due to a change in wavelength. The most common example is that of wave rays which, in approaching the shore at an angle, tend to swing perpendicular to the shore, owing to the continuous shortening of the wavelength in shoaling water.

b) Wave refraction by currents

The refraction due to a change in the seabed level is not the only kind of refraction that occurs. In the presence of quite strong currents, significant effects on the wave propagation are likely to occur including a change of wavelength and wave height. These changes of wave height and wavelength, compared to the values that would have been obtained if there had been no currents present, are known as refraction by currents.

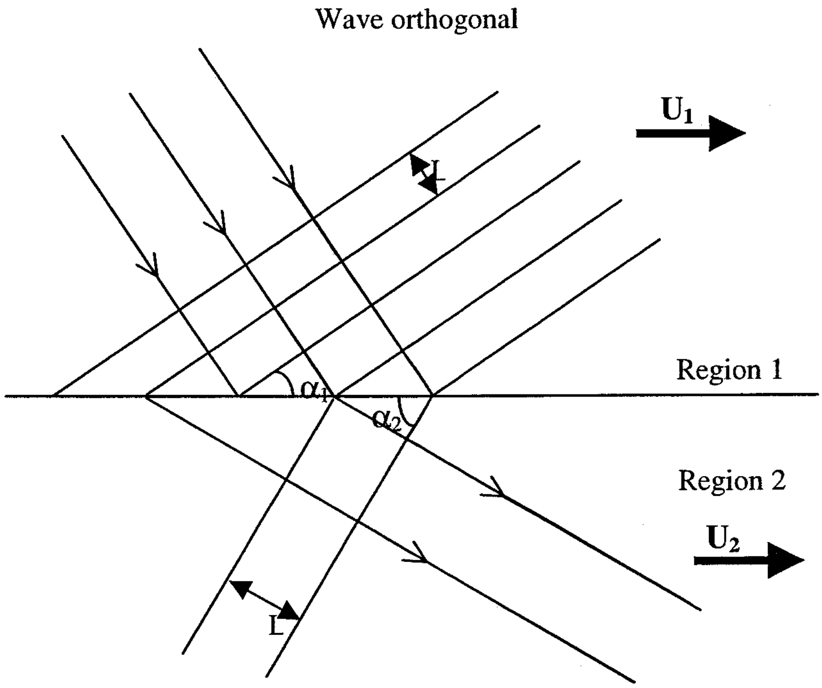

A simple case demonstrates this phenomenon: The waves are propagating over an area of constant depth in a region with a discontinuity in the current velocity but not in the direction.

The change in direction will be determined in a similar way as in the case of the depth refraction, that is, by simply using Snell's law:

$$\frac{\sin\alpha_1}{\sin\alpha_2} = \frac{L_1}{L_2}$$

There is also a change in wave height associated with the refraction by currents. It has been calculated using the principle of conservation of wave action defined by Jonsson. (1978)

Jonsson's derivations led to the following results:

$$\frac{H_2}{H_1} = \left(\frac{n_1}{n_2} \frac{\sin 2\alpha_1}{\sin 2\alpha_2} \right)^{\frac{1}{2}}$$

Where:

$$n_1 = \frac{1}{2}\left(1 + \frac{2k_1 d}{\sinh 2k_1 d}\right)$$

and

$$n_2 = \frac{1}{2}\left(1 + \frac{2k_2 d}{\sinh 2k_2 d}\right)$$

with d the constant depth.

It is clear that this example is an idealised one and that reality is far more intricate since refraction by current and depth refraction are likely to occur simultaneously. Moreover, the current field is never as simple as it is in this case. Therefore a numerical model has to be used to represent both effects. However, current depth refraction is a complex problem as it propagates in an inhomogeneous, anisotropic, dispersive, dissipative and moving medium.

2.2.3 Shoaling

As in the case of refraction with which it is often associated, shoaling is caused by spatial variation in water depth. Shoaling is a phenomenon that frequently occurs in nearshore regions. Waves that are travelling over a seabed with a slope slow down, as the depth becomes smaller. If little or no wave energy is dissipated and since the wave energy flux almost remains constant despite the deceleration, the energy density of the waves must increase. As a result, the waveheight increases as well. This phenomenon is known as shoaling.

2.2.4 Reflection

Wave trains may also interact with reflected waves near to structures. The addition of two trains of equal waves travelling in opposite directions produces standing waves, which oscillate up and down without propagating in any direction. In this pattern, peaks and troughs are found only at certain specific locations half a wavelength apart, and they do not move along. Crests rise vertically, fall vertically and are replaced by troughs; these troughs rise vertically and are replaced by other crests, and so on. The resultant waves, consist of a number of regions where the vertical displacement is maximal, alternating with regions where vertical displacement is zero. The points where the maximum displacement is observed are known as antinodes. They are spaced half a wavelength apart. Starting at the wall where there is an antinode, the first node, that is, where the displacement is zero, is located one quarter wavelength away and the interval between two nodes is half a wavelength.

2.3 Wave breaking theory

In this section, the detailed phenomena involved in the area of study will be described.

Wave breaking is the most obvious and spectacular of all the physical processes that affect surface water waves. It is also the most complex and any thorough attempt to understand the physical processes involved needs to address many different aspects of the phenomenon. Amongst the most important are:

Transformation of waves during breaking:
- Factors influencing the initiation of breaking
- Formation and propagation of a roller and broken wave
- Reformation of unbroken waves after breaking over banks or bars
- Energy exchange between spectral components

Generation of surf zone phenomena:
- Production and dissipation of turbulence
- Water level set-up
- Longshore currents
- Cross-shore currents (undertow)
- Nearshore current circulation patterns
- Low-frequency waves

Effects on solid material:
- Erosion and deposition of seabed sediment
- Erosion of dunes and cliffs
- Forces on breakwaters and seawalls

2.3.1 Classification of breaker types

Galvin (1968) provided a classification of the breaker type depending on the way waves break. A breaker is an individual breaking wave. Breaking waves are mainly classified as spilling, plunging or surging.

a) Spilling breakers: these mostly occur in deep water or on slopes that are very mild. The wave profile is stable apart from the crest where foam is produced and spreads down the front face. It is not normally accompanied with an overturning jet of water.

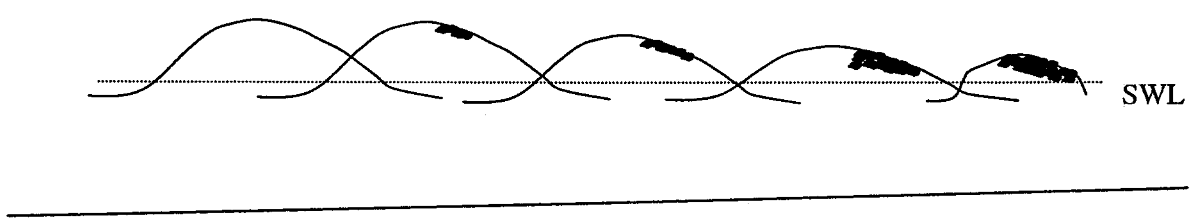

b) Plunging breakers: In contrast to spilling breakers, plunging breakers occur where the waves become strongly asymmetric. They occur when the top of the wave curls over the front face forming a jet that overturns and plunges into the water in front of the face of the wave. An air pocket is enclosed between the jet and the wave face that generates considerable turbulence and a lot of spray and white water. The falling jet of water bounces on the surface of the water ahead of the wave. Plunging breakers are more likely to be found on moderately steep beaches.

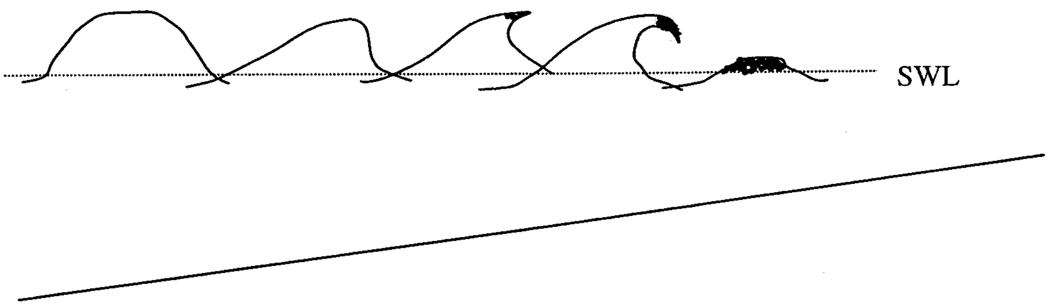

c) Surging breakers: these occur when a relatively small wave near the shoreline builds up a crest as in the previous case, but before the jet forms, the bottom of the waves surge forward up to the water line. They are normally seen on steep beaches close to the water line.

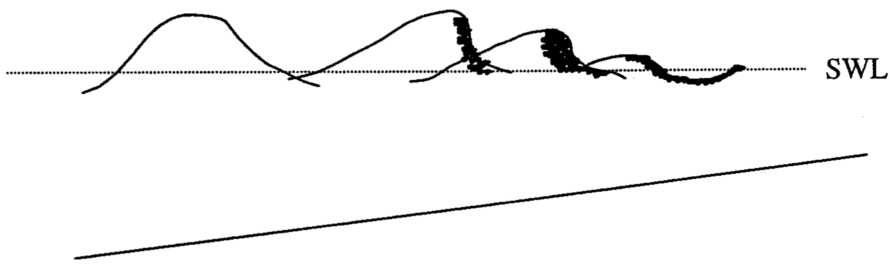

d) Collapsing breakers: a fourth breaker type, namely collapsing breakers can be defined as an intermediate state between the plunging breaker and the surging breaker. However the first three types of breaker listed are the main ones that are observed.

2.3.2 Description of wave breaking

Before breaking, waves have a relatively smooth water surface (figure below). After breaking the wave fronts are usually white and foamy often with a lot of spray and bubbles. Complex processes take place during breaking, involving a rapid change of wave shape and the conversion of wave energy to turbulence and subsequently heat. After a short distance, roughly several times the depth of breaking, the breaking-induced turbulence becomes fully developed and the wave adopts a steady, well-organised profile which is more-or-less independent of the initial breaking behaviour, but still often with white water on the crest face.

Principal regions of the surf zone

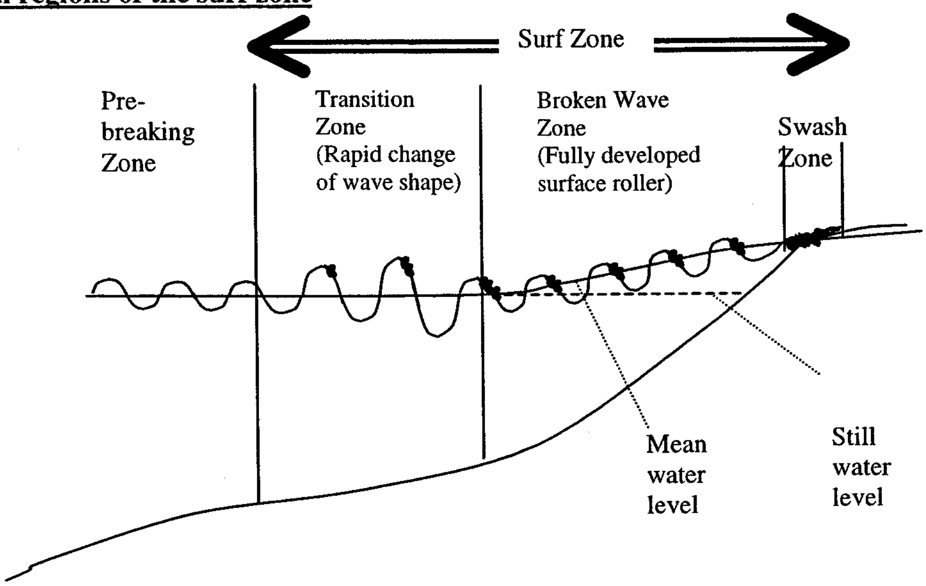

2.3.3 Energy dissipated in wave breaking

After waves break, they carry on propagating shoreward, but in a different manner. Energy is dissipated as the breaking creates turbulence.

A common approach to describe the energy dissipation is to solve the steady state equation governing energy balance for waves advancing towards the shore:

$$\underline{\nabla}(E C_g) = -D_b \qquad [8]$$

With:

- E the mean wave energy density per unit area, which using the linear assumption for small amplitude wave, can be expressed as $E=1/8\rho g H^2$
- ρ the water density
- H the wave height
- D_b the spatial rate of dissipation of wave energy flux by breaking
- C_g the group velocity

The dissipation due to breaking has been studied using the formulation for the dissipation as used in the case of a hydraulic jump (or bore). These phenomena are quite similar, at least from a visual point of view, and the model equations developed for the case of a hydraulic jump are frequently used by engineers to determine the dissipation of energy due to wave breaking.

Battjes and Janssen (1978) used the analogy with a bore connecting two regions of uniform flow to derive the following equation for D', which is the power dissipated per broken wave, per unit width:

$$D' \sim \frac{1}{4}\rho g H^3 \left(\frac{g}{h}\right)^{\frac{1}{2}} \qquad [9]$$

Therefore the equation for the spatial dissipation of wave energy flux by breaking is:

$$D_b = \frac{\lambda \rho g^{\frac{3}{2}} k H^3}{8\pi h^{\frac{1}{2}}} \qquad [10]$$

where λ is an empirical constant of the order of 1, which makes the distinction between the bore process and the breaking process.

The formula derived by Battjes and Janssen is:

$$D = \frac{\alpha}{4} Q_b \bar{f} \rho g H_m^2 \qquad [11]$$

where $\bar{f}$ is the mean frequency of the energy spectrum
α is a constant of the order of 1
Q_b is the probability that at a given point a height is associated with a breaking or broken wave
H_m is the maximum possible wave height

It is worth noting that in 1984 Svendsen derived an expression for λ dependent on the wave crest and the wave height to water depth ratio, H/h.

Dally et al (1984) assumed that the rate of dissipation of broken wave energy is proportional to the difference between the actual energy flux and a lower stable flux level.

$$D_b = \frac{K}{h}\left[EC_g - EC_{gs}\right] \qquad [12]$$

Where K is a non-dimensional decay coefficient (Dally's constant).
h is the still water level.
EC_g is a depth integrated time-averaged actual energy flux.
EC_{gs} is the lower stable flux

It can be assumed, based on the experiment carried out by Horikawa and Kuo (1966), that the stable wave height can be related to the depth by:

$$H_s = \Gamma h \qquad [13]$$

Where Γ is a dimensionless coefficient with a value between 0.35 and 0.4. Dally recommended 0.4 as a value for Γ, and this value has been employed in the present work when the Dally formula has been used.

Girolamo et al (1988) proposed the following alternative values for K and Γ:

Slope	K	Γ
1/80	0.350	0.100
1/65	0.355	0.115
1/30	0.475	0.275

The formula they derived for the rate of dissipation of broken wave energy was derived using the assumption of small amplitude linear waves to obtain E.

This assumption yields:

$$D_b = \frac{\rho g C_g K}{8h}\left(H^2 - \Gamma^2 h^2\right) \qquad [14]$$

Assuming that $C_g = \sqrt{gh}$, the wave energy balance equation can be rewritten:

$$D_b = \frac{\rho g^{\frac{3}{2}} K}{8\sqrt{h}}\left(H^2 - \Gamma^2 h^2\right) \qquad [15]$$

The two models for the dissipation that have been described above (the Battjes and Janssen model and the Dally model) are the two options given in ARTEMIS as well as in FDWAVE. They were both tested in section 4.2 below (detached breakwater case).

The problem of decay of the broken wave energy has also been treated using the concept of eddy viscosity. For instance, Mizuguchi (1981) obtained the following formula for the energy dissipation:

$$D_b = 0.5\rho g \upsilon_e (kH)^2 \qquad [16]$$

where:

v_e: eddy viscosity coefficient
k: wave number

The dissipation and breaking are two phenomena closely linked to the so-called radiation stress that is of the greatest interest to engineers when they want to model the wave-current interaction (see section 2.4).

2.3.4 Representation of the bed friction of combined wave and current flow

Bed friction induced by combined wave/current flow is of great interest to the coastal engineer, since it is the prime factor which balances the wave-driving forces produced by wave breaking in wave-induced nearshore circulation. It is also expected that a combined wave and current flow is more efficient in eroding bottom sediments than either unidirectional flow due to the increase of bed shear stress or oscillatory flow due to additional mass transport. Consequently, several techniques have been devised to evaluate bed friction or the velocity profile near the bed in combined wave/current flow, with varying degrees of accuracy and complexity.

Bijker (1966) was among the first researchers to try to estimate the resultant bed shear stress of combined wave/current flow by considering the fine structure of flow motion near the seabed. His work is still actively used and had been used as a basis to further developments. This model starts from Prandtl's mixing length theory. He assumed the wave-induced orbital motion to have a logarithmic profile in the near-bed region. Then, from any (hypothetical) point above the bed, it is possible to draw a line emanating from the seabed that is tangential to the current velocity profile at this point. Therefore, once the particle velocity is known at that point, the velocity gradient can be estimated and, hence, the shear stress as well as the bed friction factor can be evaluated using the mixing length theory.

The depth-integrated, wave period-averaged variation of the mean flow energy due to bed friction given by Yoo and O'Connor (1988) was represented as:

$$\widehat{D} = -\left\langle \int_0^d \bar{u} \frac{\partial \hat{\tau}}{\partial z} dz \right\rangle - \left\langle \int_0^d \tilde{u} \frac{\partial \hat{\tau}}{\partial z} dz \right\rangle \qquad [17]$$

with:

z	the vertical co-ordinate
d	the water depth
$\hat{\tau}$	the instantaneous value of resultant wave/current shear stress
$\bar{u}$	the current particle velocity
$\tilde{u}$	the wave particle velocity

The first term in the right hand side of equation 17 is the turbulent dissipation rate of the combined flow active along the current direction, and the second one is the turbulent dissipation rate of the combined flow active along the wave direction.

A systematic review of formulations of bed stress under waves and currents is given by Soulsby et al (1993).

2.4 Driving forces, radiation stresses and set-up

In spite of being a relatively new concept, radiation stress plays an important role in a number of oceanographic coastal engineering phenomena. Since this concept is more mathematical than physical, it is useful to give a simplified explanation of what the radiation stress is and what its physical meaning is.

2.4.1 Radiation stress

Since Lamb (1932), it is well known that surface waves possess momentum which is directed parallel to the direction of propagation and the momentum is assumed to be proportional to the square of the wave amplitude.

As stress is equivalent to the momentum flux, the radiation stress may then be defined as the excess flow of momentum due to the presence of the waves. If the momentum equations are time- and depth-averaged, volume forces coming from the gradient of the radiation stress will appear.

The radiation stress is expressed as a stress tensor S with four components:

- S_{xx}: momentum in the x-direction normal to a yz plane
- S_{yy}: momentum in the y-direction normal to a xz plane
- S_{xy}: momentum in the y-direction parallel to a yz plane
- S_{yx}: momentum in the x-direction parallel to a xz plane

S_{xx} and S_{yy} are normal stresses (pressures), while S_{xy} and S_{yx} are shear stresses.

Crapper (1979) has derived general expressions for the radiation stress tensor.

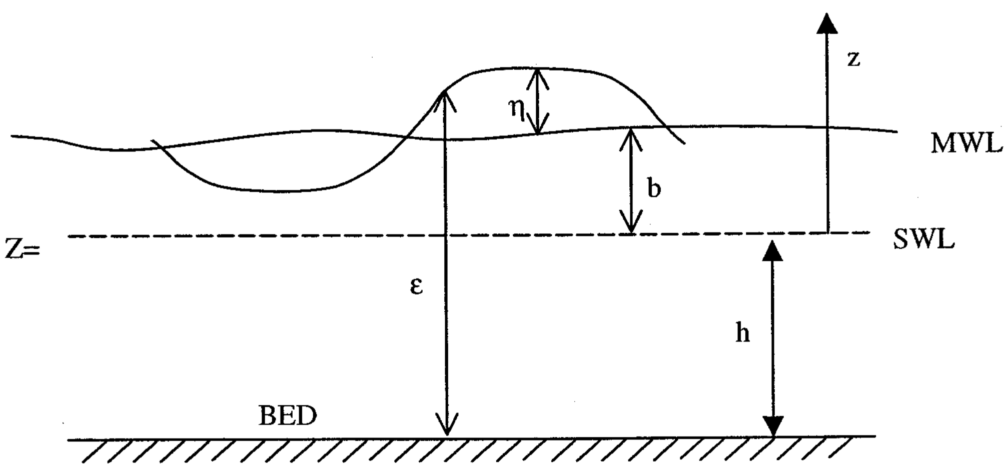

With:

z	vertical co-ordinate (m), zero at still water level (SWL)
ε	water depth (m)
η	height of free surface above mean water level (MWL – includes wave set-up) (m)
b	wave set-up (height of mean water level above still water level) (m)
h	height of still water level (SWL) above bed (m)

So:

$$\varepsilon = \eta + b + h$$

$$\bar{\eta} = 0$$

$$\bar{\varepsilon} = b + h$$

where the overbars indicate a time-averaged value.

The components of the radiation stress are found to take the following form after the governing equations have been averaged in time and through the vertical:

$$S_{xx} = \overline{\int_{-h}^{\varepsilon} \left(p + \rho u^2\right) dz} - \overline{\int_{-h}^{b} p_0 dz} \qquad [18]$$

$$S_{yy} = \overline{\int_{-h}^{\varepsilon} \left(p + \rho v^2\right) dz} - \overline{\int_{-h}^{b} p_0 dz} \qquad [19]$$

$$S_{xy} = S_{yx} = \overline{\int_{-h}^{\varepsilon} \rho uv dz} \qquad [20]$$

Where:

p is the total pressure obtained from the vertical momentum equation:

$$p = \rho g(\varepsilon - z) - \rho w^2 + \frac{\partial}{\partial x}\int_{z}^{0} \rho uw dz + \frac{\partial}{\partial y}\int_{z}^{0} \rho vw dz + \frac{\partial}{\partial t}\int_{z}^{\varepsilon} \rho w dz$$

and p_0 is the hydrostatic pressure: $p_0 = \rho g(b - z)$

u, v are the water particle velocities in the x and y directions, h is the local depth measured from the SWL, and ρ is the water density.

The overbar stands for a time averaged value.

In general, the time dependant term in the expression of the pressure is not taken into account.
The formulae (18)-(20) to define the radiation stress and the forces induced were evaluated in 1964 by Longuet-Higgins and Stewart in the case of progressive gravity waves

$$S_{xy} = S_{yx} = \frac{\rho g H^2 C_g \sin 2\alpha}{16C} \qquad [21]$$

$$S_{xx} = \frac{1}{8}\rho g H^2\left[\left(\frac{2C_g}{C} - \frac{1}{2}\right)\cos^2\alpha + \left(\frac{C_g}{C} - \frac{1}{2}\right)\sin^2\alpha\right] \qquad [22]$$

$$S_{yy} = \frac{1}{8}\rho g H^2\left[\left(\frac{2C_g}{C} - \frac{1}{2}\right)\sin^2\alpha + \left(\frac{C_g}{C} - \frac{1}{2}\right)\cos^2\alpha\right] \qquad [23]$$

C_g is the group velocity
C is the wave celerity
α is the wave direction defined as on the figure below.

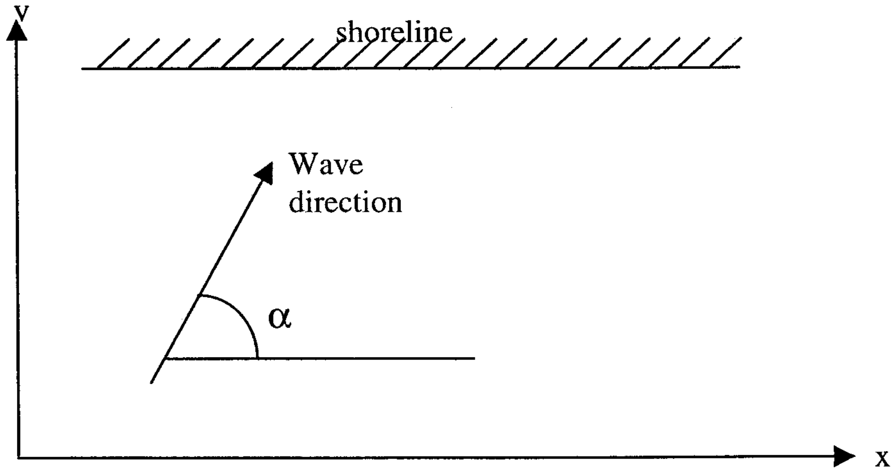

The wave set-up (the rise of mean water level caused by the wave breaking) is then calculated from the onshore time-mean momentum equation:

$$\frac{d\eta}{dy} = \frac{1}{\rho g(h + b + \eta)} \frac{dS_{yy}}{dy} \qquad [24]$$

The driving forces in the x and y directions caused by the gradient of the radiation stresses are respectively:

$$F_x = -\frac{\partial S_{xx}}{\partial x} - \frac{\partial S_{xy}}{\partial y} \qquad [25]$$

and:

$$F_y = -\frac{\partial S_{yy}}{\partial y} - \frac{\partial S_{yx}}{\partial x} \qquad [26]$$

As mentioned before, this set of equations is correct only in the case of progressive waves, which implies neglecting the reflection. This does not introduce major errors in the normal cases of propagation in coastal areas since reflections are usually weak. For more complex situations, equations have been developed for cases where waves cannot be assumed to be progressive (see Copeland (1985) or Bettess and Bettess (1982)).

2.4.2 Calculation methods for radiation stress

Dingemans et al (1987) derived an equation for the radiation stress tensor that is valid not only for purely progressive waves but also for any arbitrary two-dimensional wave field, provided that the waves are linear. They used the wave potential and its conjugate and concluded with the following equation for the radiation stress tensor.

Using the dispersion relation for linear waves: $\omega_r^2 = gk\tanh(kh)$

φ : wave potential

φ^* : conjugate wave potential

ω_r : relative frequency

$$S_{ij} = \frac{\rho}{4g}\left[CC_g \left(\frac{\partial \varphi}{\partial x_i}\frac{\partial \varphi^*}{\partial x_j} + \frac{\partial \varphi^*}{\partial x_i}\frac{\partial \varphi}{\partial x_j} \right) + \omega_r^2 \left(\frac{2g}{C} - 1 \right) \varphi\varphi^* \delta_{ij} + \frac{1}{2}\left(gh - CC_g \right) \frac{\partial^2}{\partial x_m \partial x_m} \left(\varphi\varphi^* \right) \delta_{ij} \right] \quad [27]$$

where:

$$C_g = \frac{\partial \omega_r}{\partial k} = \frac{g}{2\omega_r}\left[\tanh(kh) + kh\left\{ 1 - \tanh^2(kh) \right\} \right]$$

It is well known that when modelling a velocity potential a very fine mesh grid has to be chosen. It is recommended to take ten nodes per wavelength so as to determine the wave pattern with sufficient accuracy. Also the radiation tensor is a function of the spatial co-ordinates that is likely to change considerably from one point to another. The problem associated with this is that the differentiation of the component of the radiation stresses might give inaccurate results. To overcome the difficulty linked with the numerical differentiation of the radiation stress tensor, Dingemans (1987) showed that for a mild bed slope the driving force is closely proportional to the wave energy dissipation per unit area.

Dingemans (1987) showed that it is possible to separate the components of the driving force into three parts. The first term, which is the rotational part of the driving force, is related to the wave energy dissipation and can create both current and set-up. The second term is theoretically not likely to create current. It is called the irrotational term since it can be expressed as the gradient of potential function which is related to the water pressure and, hence, the surface elevation. This term contributes to a set-up of the water level. The third term is neglected in the case of combined refraction/diffraction. Therefore, the driving force can be computed using only the first term, that is to say that the driving force becomes a function of the wave energy dissipation.

The wave dissipation function D is composed of the contribution due to the breaking D_b and the contribution due to bottom friction D_f. It has been assumed for years that all kinds of dissipation produce a force and O'Connor and Yoo (1988) stated that the bottom friction induced by combined wave/current flow is the main force to counterbalance the driving forces produced by the radiation stresses in the wave-induced nearshore circulation.

The question arose from Dingemans' paper where he mentioned that the dissipation due to bottom friction might only generate a vertical circulating flow and, hence, may not play a role in the generation of depth-integrated currents. This is actually not a big issue since the term of bed friction dissipation is much less than the term of breaking dissipation and can therefore be neglected.

The expressions derived by Dingemans et al in 1987 for the irrotational and rotational terms of the driving force induced by the radiation stress are:

$$F_{irr,x} = -\frac{1}{8}\rho g h \frac{\partial}{\partial x}\left(\frac{H^2}{h}\left(\frac{C_g}{C} - \frac{1}{2} \right) \right) \quad [28]$$

$$F_{irr,y} = -\frac{1}{8}\rho g h \frac{\partial}{\partial y}\left(\frac{H^2}{h}\left(\frac{C_g}{C} - \frac{1}{2} \right) \right) \quad [29]$$

$$F_{rot,x} = \frac{D}{C}\cos\alpha \quad [30]$$

$$F_{rot,y} = \frac{D}{C} \sin\alpha \qquad [31]$$

where D is the wave energy dissipation per unit time (m^2/s^3).

Tests were carried out in the present study (see Chapter 4) to investigate the differences in the results obtained using the Dingemans formula (FDWAVE) or the Longuet-Higgins formula (ARTEMIS).

2.4.3 Implementation of radiation stress in numerical models

A major problem is to know how to enter the driving forces in the flow model. In the case of a 2D model it is straightforward, but for a 3D model, a distribution of the forces along the vertical has to be chosen. In the tests in Chapter 4, two methods were chosen.

1 The imposition of the force at the surface (like a wind) was the first attempt. This at first appears to be an unusual approach because the driving forces came from integration along the vertical. It will however create a strong variation of the current along the vertical. The current at the surface will be in the opposite direction to the current at the bottom. It is therefore a sensible choice if, for example, the undertow is very strong.

2 The other method was to give a constant distribution of the driving forces along the vertical but with adding a roller effect at the top. This is a method that takes into account the fact that the driving forces came from integration along the vertical. It does not however create such a large variation of the current along the vertical.

The contribution of the roller can be expressed by approximating the horizontal profile as suggested by Svendsen (1984):

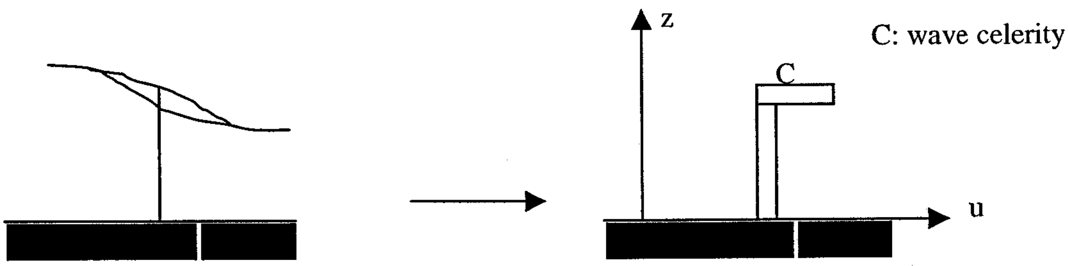

Velocity distribution under
The front of a breaking wave

Approximation for the horizontal
velocities in the surf zone waves

H: Wave height
L: Wave length

The time averaged entrainment force t due to the roller is specified uniform from the wave trough to the mean water level, a layer thickness of H/2.

Introducing the flux of energy D in shallow water:

$$t = \frac{14D}{\rho g H T} \qquad [32]$$

$t_x = t \cos\alpha$
$t_y = t \sin\alpha$

The roller can be computed using the driving forces.

$$t_x = \frac{14}{g}\frac{c}{HT}F_x \qquad [33]$$

$$t_y = \frac{14}{g}\frac{c}{HT}F_y \qquad [34]$$

Using these equations the specification of the wave driving force, including the roller is complete.

2.5 Viscosity and friction

The following equation (following De Vriend and Stive, 1987) is used to obtain the eddy viscosity:

$$\nu_t = K u_* h + M h (D_b/\rho)^{1/3}$$

ν_t = Eddy viscosity coefficient
M = 0.025
K= 0.083
u_*= Shear velocity at seabed
D_b = Wave energy dissipation rate
ρ = Water density

In our case the main factor derives from the wave breaking therefore we did not take into account the effect of the current and the eddy viscosity will be equal only to the second part of the equation.

The viscosity is computed using the equation $0.04h^{0.8333}Hk^{0.333}$.

There were a few tests carried out to estimate this equation using the straight beach case. Two expressions that are often used are:

- $0.008\ h\ (gh)^{0.5}$ [35]
- $0.0267\ H.\ h^{0.8333}\ K^{0.3333}$ [36]

Svendsen (1990) advises for numerical purposes to use a value between $0.008\ h\ (gh)^{0.5}$ and $0.08\ h\ (gh)^{0.5}$.

Equation 35 is nearly the same as equation 36 but with a factor 1.5. Equation 36 is smoother than equation 35, and for this reason equation 36 corrected by a coefficient of 1.5 was used in the tests described in Chapter 3. This equation is only valid in the surf zone, therefore we need to use it in the part of the domain after breaking and set the viscosity elsewhere to a minimum value.

The maximum orbital velocity is also computed because it will be useful for computing the friction in the flow model (which is the sum of wave and current parts, see section 2.3.4):

W=Hkc/(2sinh(kd))

$$u_m = \frac{H\omega_r}{2\sinh(kd)}$$

u_m= peak wave orbital velocity at the sea bed
ω_r: relative frequency
k: wave number
c: phase velocity
H: wave height
d: water depth

$\alpha = 0.72$
W = peak wave orbital velocity (m/s)
U = Current speed (m/s)
n=1
With the effect of wave breaking, the friction coefficient is multiplied by the quantity :

$$\left(1+\alpha\frac{W}{U}\right)^{n}$$

2.6 Turbulence models

The aim is to create a model of the turbulence for fluctuation on the mean value of the current. These displacements on a small scale cannot be represented by the mesh and the time step, so they are represented in the flow model by terms taking the form of a viscosity.

Usually these are the models used to represent the turbulence

- algebraic relation
- mixing length model
- k-ε model

Where the model is one of flow only (without the effect of waves) then the mixing length model (very frequently used in estuaries and coastal zones) or the k-ε model (used in river flow cases) are most often used. The mixing-length model assumes that there is equilibrium between the generation and dissipation of the turbulence. Therefore it is much quicker in modelling than the k-ε model which computes the generation, dissipation and transport and diffusion of the turbulence energy. The algebraic and mixing-length models have been used below for cases with wave-driven flows. The imposition of the turbulence via an algebraic relationship may be best where the turbulence is being imposed on the flow (e g by the action of wave breaking).

a) Algebraic relation

This basic model considers that the eddy viscosity is specified (often a constant value). It is reliable if the main factors for the flow are the pressure gradient and the transport.

b) Mixing-length model

The horizontal diffusion coefficients may be specified by the user or related to the vertical coefficients.

$$\upsilon_Z = f(Ri) lm^2 \sqrt{\left(\frac{\partial u}{\partial z}\right)^2 + \left(\frac{\partial v}{\partial z}\right)^2} \qquad \text{where} \qquad Ri = -g\frac{\frac{1}{\rho}\frac{\partial \rho}{\partial z}}{\left(\frac{\partial u}{\partial z}\right)^2 + \left(\frac{\partial v}{\partial z}\right)^2}$$

Ri is the Richardson number
f is a damping velocity function
lm is the mixing length
The bed shear stress is modelled as a quadratic function of the velocity

Where

ΔZ is the distance between the first point used for the calculation at Z_f and the bed.
D: granulometry
The granulometry is connected to the Chezy coefficient by:

$$Ch = \frac{26.4}{D^{1/6}}\left(\frac{D}{h}\right)^{1/24} h^{1/6}$$

c) k-ε model

k: kinetic turbulent energy
ε : dissipation
P: turbulent energy production term
G: source term due to gravity forces

$$k = \frac{1}{2}\overline{u_i' u_i'}$$

$$\varepsilon = \upsilon \overline{\frac{\partial u_i'}{\partial x_j}\frac{\partial u_i'}{\partial x_j}}$$

$$\overline{-u_i u_j} = \nu_t \left(\frac{\partial u_i}{\partial x_j} + \frac{\partial u_j}{\partial x_i}\right) - \frac{2}{3}k\delta_{ij}$$

$$-\overline{u_i' T'} = \frac{\nu_t}{P_{rt}}\frac{\partial T}{\partial x_i}$$

k and ε are derived from the convecting equations
where

$$\frac{\partial k}{\partial t} + u_i \frac{\partial k}{\partial x_i}\left(\frac{\upsilon_t}{\sigma_\varepsilon}\frac{\partial k}{\partial x_i}\right) + P + G - \varepsilon \qquad [37]$$

$$\frac{\partial \varepsilon}{\partial t} + u_i \frac{\partial \varepsilon}{\partial x_i} = \frac{\partial}{\partial x_i}\left(\frac{\upsilon_t}{\sigma_\varepsilon}\frac{\partial \varepsilon}{\partial x_i}\right) + C_{1\varepsilon}\frac{\varepsilon}{k}\left[P + (1 - C_{3\varepsilon})G\right] - C_{2\varepsilon}\frac{\varepsilon^2}{k} \qquad [38]$$

with

$$P = \upsilon_t \left(\frac{\partial u_i}{\partial x_j} + \frac{\partial u_j}{\partial x_i}\right)\frac{\partial u_i}{\partial x_j}$$

$$G = \beta \frac{\upsilon_t}{Pr_T} g \frac{\partial T}{\partial z}$$

and

$$\beta = -\frac{1}{\rho}\frac{\partial \rho}{\partial T}$$

Pr_T is the Prandtl number

$$\upsilon_t = C_\mu \frac{k^2}{\varepsilon}$$

The values of the constants are:

C_μ	$C_{\mu T}$	Pr_T	$C_{1\varepsilon}$	$C_{2\varepsilon}$	$C_{3\varepsilon}$	σ_k	σ_e
0.09	0.09	1.0	1.44	1.92	0 if G>0 1 if G≤0	1.0	1.3

3. DESCRIPTION OF THE EXPERIMENTS

The effectiveness of different modelling techniques must be established, at least in part, by comparison with experiments. These are generally carried out in the laboratory (i e they are physical models) because wave conditions in the field are very variable, in space and time. It is widely believed that models must be able to reproduce adequately the results of such controlled experiments before they can be applied to actual engineering conditions with confidence.

The selection of the test cases was guided by the following factors

- coverage of a range of conditions (river structure, estuary structure, beach etc)
- availability of adequate standard data (prototype or experimental)
- availability of alternative numerical model simulations (e g SSIIM)
- relevance to practical situations

The reasons for the selection of the individual cases are:

a) Straight beach

This case tests the breaking and radiation stress simulation of the wave model and the ability of the three dimensional flow model to represent the resulting mean flow circulation in the vertical plane

b) Detached breakwater

This case adds an offshore structure to the case above. The wave model has to simulate diffraction phenomena and a mean flow circulation in the horizontal plane results

c) Beach cusps

This is a case designed to produce a rip-current phenomenon. Comparisons were made with measurements from the UK Coastal Research Facility.

d) Groyne

This case refers to earlier HR work supported by DoE/DETR. As well as experimental measurements, the 3D code SSIIM was previously applied in this case.

e) Estuary training wall

This case extends the test case (d) to an unsteady case of an estuary training wall where a gyre forms during the ebb tide. ADCP measurements were made over the course of a tide.

Of these cases the first three are predominantly driven by waves and the last two are current-only examples. Descriptions of the test cases are given below and the comparison with numerical model testing is reported in Chapter 4.

The theoretical background required for the understanding of the flow processes involved in these test cases has been expounded in Chapter 2 above. The results of the comparison tests using numerical simulation methods are described below in Chapter 4.

3.1 Straight beach

A comparison was carried out with the work of Cox and Kobayashi (1996) on wave height and set-up on a straight beach.

Cox and Kobayashi (1996) performed an experiment using regular waves in the Precision Wave Tank at the University of Delaware. The flume was 33m long, 0.6m wide and 1.5m deep and it had a fixed coarse grain bed with a slope of 1:35. The wave height was 0.13m and wave period was 2.2s. The velocity profile through the vertical, the set-up and the wave height were measured.

3.2 Detached breakwater

Mory and Hamm (1996) measured currents behind a detached breakwater in a wave tank.

The horizontal dimensions of the wave basin were 30m by 30m. The bed was separated into three parts:

- A horizontal bed in the offshore region which was 4.4 m wide and 0.33 m deep
- An underwater plane beach with a constant slope (1:50) between 0.33 m and 0.0 m (still water level)
- An emerged plane beach with a constant slope (1:20), cresting at +0.066 m

A breakwater 6.66m long and 0.87m wide was built parallel to the shoreline and was screwed to the border of the basin, as shown in the figure below. The offshore side of the breakwater was supposed to be low reflective.

The incident wave generated offshore was regular and the wave height at the wave marker was 7.5 cm, the period was 1.7 seconds and the incidence was normal to the shoreline.

The depth-averaged current, the wave height and the set-up were all measured.

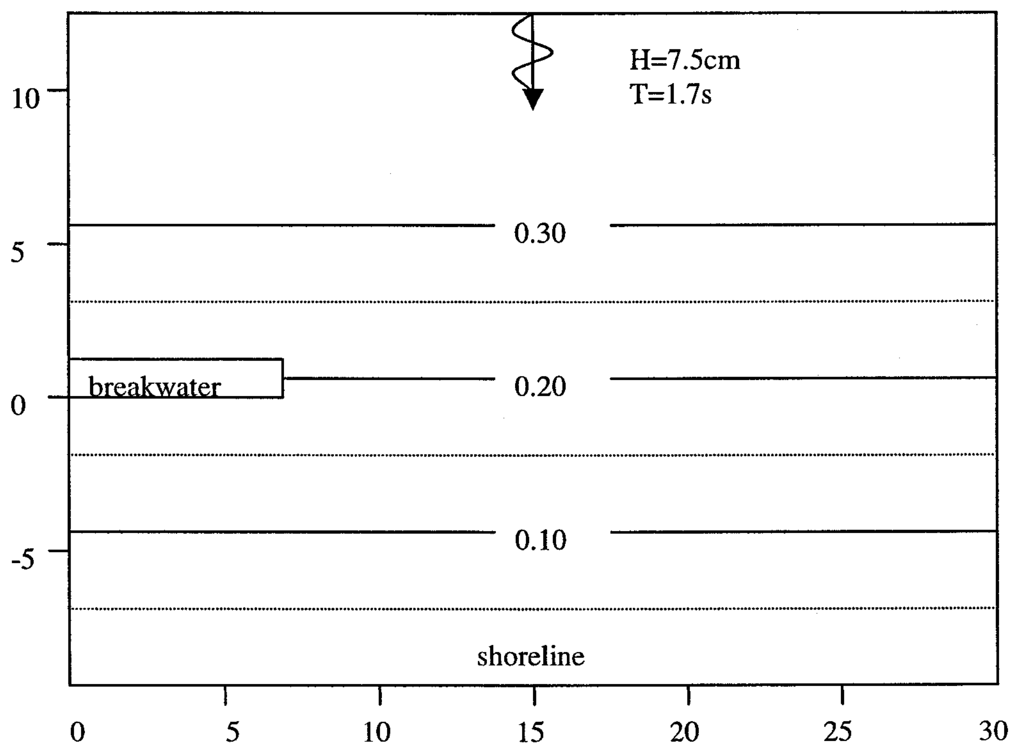

3.3 Beach cusps

Wave-induced currents at cusped beaches are important for large-scale horizontal mixing processes. In this test, data were measured on the nearshore currents due to a sinusoidal multi-cusped beach installed in the UK Coastal Research Facility (UKCRF), see figure below for the model layout. Horizontal spatial patterns of the currents have been determined by digital image analysis of the motions of neutrally buoyant markers. For normally incident regular waves, combinations of rip and longshore currents gave rise to a steady system of multiple circulation cells. Oblique incident waves generated a stable meandering longshore current. Detailed information on the depth profiles of rip and meandering nearshore currents was obtained using Sontek Acoustic Doppler Velocimeters (ADVs). The profiles indicate that the outflowing rip current is nearly horizontal with low frequency oscillations evident. The meandering current is steady and has a logarithmic profile near the bed.

At multi-cusped beaches, waves do not break uniformly, and so the excess mass and momentum fluxes lead to the production of nearshore currents. For normally incident waves at a multi-cusped beach, longshore currents are generated parallel to the beach contours and directed from cusp crests to troughs where they feed into rapidly flowing offshore jets (rip currents). In turn, these are balanced by inflowing currents at the cusp crests. Thus a system of primary nearshore circulation cells is established at a multi-cusped beach by normally incident regular waves. For oblique incident waves, the excess fluxes predominate in one alongshore direction, and so a meandering longshore current occurs instead of a primary nearshore circulation system. For all regular waves, whether normally incident or oblique, a system of secondary circulation cells is generated in the shallowest water, inshore of the breaker line and encompassing the swash zone.

The UKCRF has plan dimensions 27m (cross-shore) x 36m (alongshore) with a working area of 20m x 15m. Waves are generated using a 72 paddle wave-maker; longshore currents may be recirculated using 4 pumps. The mean water level at the paddles was 0.5m.

The multi-cusped beach had overall dimensions of 12m alongshore and 5m across-shore. It consisted of three sinusoidal cusps situated on a 1:20 plane beach, with the still water depth given by

$$h(x,y) = s\left[(x_L - x) - A\sin\left(\frac{\pi(x_L - x)}{x_L}\right)\left(1 + \sin\left(\Phi - \frac{2\pi y}{R}\right)\right)\right]$$

where x is the distance measured onshore from the cusp's toe (located 5m onshore from the toe of an underlying plane beach of slope, s=0.05), y is measured alongshore from the edge of the cusps, $x_L = 5$m is the cross-shore length of the cusps, A=0.75 m is the amplitude of the sine wave used to generate the cusped profile above the plane beach, R = 4 m is the longshore wave length of a single cusp and $\Phi = 3\pi/2$ is a phase angle. The three cusps were therefore located within $0 \leq x \leq 5$ m and $-12 \leq y \leq 0$ m (see the figure below). The product of A and s represented the maximum height of cusp possible for the above configuration; a larger value would have resulted in a shoal being created. The choice of formula was based on earlier laboratory-based work by Da Silva Lima (1981) and Borthwick and Joynes (1992) who modelled a single circulation cell in the vicinity of a half-sinusoidal beach. The bathymetry around the cusps is shown in Figure 3.1.

In the numerical model, the cusps were given a roughness length $R_h = 0.017$ m, whereas the surrounding plane beach and offshore flat were set to a roughness $R_h = 0.001$ m.

The tests took place in March 1996 over a 20-day test period, which was divided into two phases. During the first phase (lasting approximately 8 days), the overall spatial pattern of wave-induced currents was recorded using neutrally-buoyant markers and dye, and the wave distribution was recorded using a moveable wave gauge (after dry running the positionner traverses). In the second phase (lasting 12 days) 3-D velocity component measurements were taken using ADVs with particular emphasis on the vertical profiles in a rip and meandering nearshore currents at selected intervals along a cusp trough and a cusp crest.

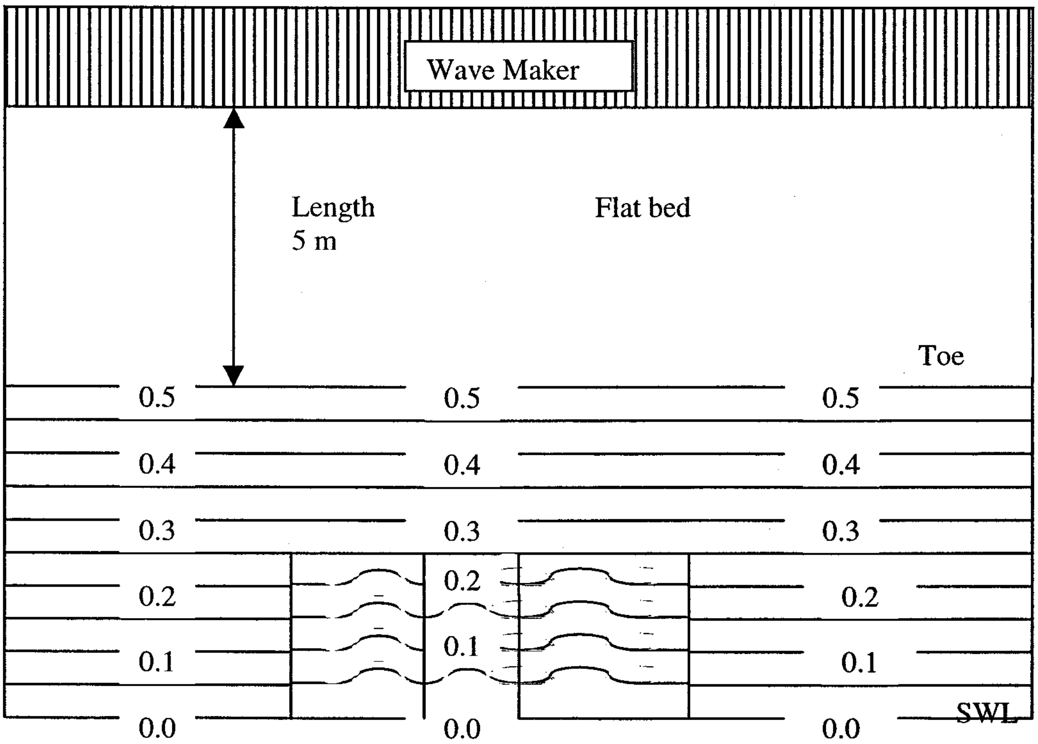

Three wave conditions were considered, with the mean water level at the wave-maker fixed at 0.5 m. The wave parameters are summarised below where T is regular wave period, T_p is random wave peak period, H is offshore (regular) wave height, H_s is significant offshore wave height and θ is the incident wave angle.

Case A Regular waves T = 1.0s H = 0.1 m θ = 0°

Case B Regular waves T = 1.2s H = 0.125 m θ = 0°

Case C Oblique waves T = 1.2s H = 0.125 m θ = 20°

The measurements demonstrated that regular waves normally incident to the multi-cusped beach caused nearshore circulation cells to develop. The primary cells consisted of fan-shaped inflowing currents which run up to the cusp peak, longshore currents from cusp peak to trough, and narrow jet-like rip currents which flow offshore at the cusp troughs. The outflowing rip currents are nearly horizontal (especially at the region of maximum velocity) with low frequency oscillations evident. The high velocity rip currents last a short distance offshore of the wave breakers. Within the range of tests considered, peak current velocities were in the order of 50 cm/s. Oblique incident waves produced an extremely stable meandering nearshore current, with a logarithmic velocity profile near the bed.

3.4 Groyne

The characteristics of the physical model were:

Flow rate: 0.131 m^3/s
Depth: 0.18 m
Groyne: 0.2 m high (the groyne was therefore unsubmerged).
Length of the groyne: 0.4 m
Width of the flume: 2.3 m
Length of the flume: 15 m

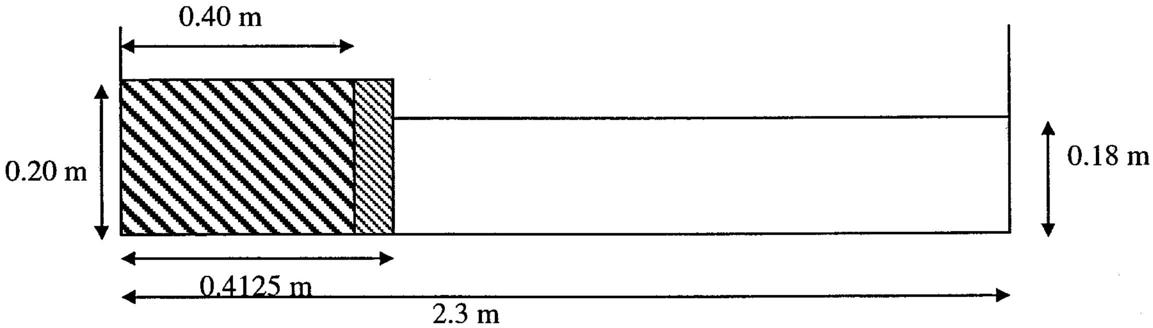

The majority of the tests were carried out in the General Purpose Flume at HR Wallingford. The GP flume has a test section 15.24m long by 2.3m wide and 0.6m deep. A pump with a capacity of about 0.13 m^3/s supplied the water to the flume, which was then discharged back into a sump, thus producing recirculating conditions.

The length of the re-circulation zone was assessed by using a fine thread fixed to the tip of a rod. At the end of the recirculation zone the predominant velocities were those caused by eddies generated in the shear layer between the recirculation zone and the main flow. Thus the flows were unsteady in this region and it was difficult to determine the extent of the recirculation zone exactly. In this test, the length of the zone was found to be between 3m and 4m (16.5 to 22.5 times the length of the groyne). The flow was monitored using a Sontek and a Minilab. The results were much more accurate with the Sontek but, when it was not available, the Minilab was used.

3.5 Estuary training wall

An important gyre during the ebb tide was observed at Trinity Quay, Felixstowe over a period of several years. Observations were made in 1995 of the tidal currents, both in the horizontal and vertical directions, using a vessel-mounted ADCP (Acoustic Doppler Current Profiler).

4. MODEL TESTING AND RESULTS

The model testing and comparison with experimental data for the test cases described in Chapter 3 has been carried out:

- to see whether the numerical models are able to represent the phenomena to a satisfactory level of accuracy
- to test whether 2D or 3D modelling is adequate for different situations
- to investigate the effects of different representations (e g of radiation stress terms)

A description of the flow models (TELEMAC and TIDEFLOW) and the wave models (ARTEMIS and FDWAVE) that were used in these tests is provided in the Appendix.

4.1 Straight beach

The straight beach case was modelled using only ARTEMIS for the wave model, however comparisons were made with earlier results from another model developed at HR Wallingford (the nearshore profile model, COSMOS-k/t, Peet and Damgaard, 1998). The flow field (including the vertical variation of the current) was modelled with TELEMAC-3D, and was also compared with COSMOS-k/t.

The domain was widened from 0.6m to 3m for the ARTEMIS wave model compared with the physical model. This was needed in order to ensure that the results in the area of interest were not contaminated by spurious effects caused by the side walls. The mesh used for the ARTEMIS simulation had 12900 nodes and 25344 elements. This amount of mesh refinement was needed because solution of the mild slope equation, on which ARTEMIS is based, gives reliable results only with 10 or more elements per wavelength.

A discussion of the results is provided here, the results are presented in Figures 1.1 to 1.5.

4.1.1 Wave height

Two tests were carried out, with and without the smoothing of the wave height. Smoothing of the wave height is a process that may be very useful because ARTEMIS models the phase of the wave; consequently if any reflection from the beach occurs, then a variation in the wave height may appear (standing wave component). In Figures 1.1 and 1.2, which show the simulation of the wave height along the central line of the physical model, it is easy to see the difference caused by the smoothing, as there is a strong variation of the wave height in the case without smoothing. The result for the wave height without the smoothing was slightly better than with the smoothing, however when the driving forces for the case without the smoothing were imported into the flow model they showed strong variations (Figure 1.3). Consequently for input to the flow model, only the forces coming from the wave model with smoothing were used.

Comparisons were carried out of the wave height, the water level set-up and the variation of the current through the vertical, as computed using ARTEMIS/TELEMAC-3D, COSMOS-k/t and observed.

In Figure 1.2, a comparison of the wave height with the HR COSMOS-k/t model and with experimental data is shown. The wave height is slightly overpredicted, but the value is of the right order of size. COSMOS-k/t gives a better answer but is very similar to the ARTEMIS result. Obviously the result cannot be perfect because it is impossible to run ARTEMIS with dry areas. Therefore a limit for dry areas has to be set which will act like a wall. In this case, the water behind this line cannot be taken into account. The set-up could also affect the result. The wave model is run with a horizontal water level, which is not the case when the set-up appears. This could also create a certain difference with the experimental results.

4.1.2 Wave set-up

As stated above, the driving forces come from the differentiation of the radiation stresses, which is not the best way to compute these forces, as it could create a high value for the driving force if the radiation stress changes in a relatively small distance. The TELEMAC-3D flow model was run with 2580 nodes and 4864 elements in the horizontal and with 8 layers in the vertical. The width for the flow model was 0.6m as in the experiment. A band in the middle of the wave model was chosen which seemed not to be affected by the side wall boundaries. The time step was equal to 0.02 second and the model was run for 3000 seconds in the 2D model and 1000 seconds for the 3D model. It is worth noting that the 3D model became steady before the 2D model.

In Figure 1.4, a comparison of the set-up from the different models is shown. Pechon (1996) concluded that it is better to correct the driving forces by a factor of 0.7. The impact of the roller was also analysed and the distribution of the force was varied. There are different ways to impose the driving forces, at the surface or along the vertical. Figure 1.4 shows that the worst results occurred for the driving forces imposed at the surface or for the driving forces plus the roller but without modifications. The best result occurred for the 2D flow model with a correction of 0.7 for the driving forces.

In conclusion, the 3D model of the driving forces (corrected by a factor of 0.7) with the roller and the 2D model (corrected by a factor of 0.7) gives a good representation of the set-up. Even though the results vary between the 2D and the 3D model, they do not differ greatly.

4.1.3 Currents

In Figure 1.5, there is a comparison of the velocity between TELEMAC-3D, observations and COSMOS-k/t along the vertical at 5m and 2.6m from the still water dry land. Unfortunately there are no experimental data at 2.6m for comparison.

The velocity using TELEMAC with the driving forces distributed along the vertical is slightly underestimated at 5m. It is interesting to see that a better result for the vertical profile of the velocity occurs for the driving forces imposed only at the surface. The COSMOS-k/t model gives a larger current variation than that observed.

This test has demonstrated the value of adopting the multiplying factor of 0.7 to the wave-driving forces resulting from ARTEMIS, as proposed by Pechon (1996), and the sensitivity of the resulting velocity field to the selection of the vertical distribution of the driving forces. The best combination of currents and water level set-up is obtained with a uniform distribution through the vertical, enhanced by representation of the roller effect. In addition it was found that for practical applications it is necessary to use the wave smoothing option in ARTEMIS, because reflections can otherwise have too large an effect on the wave driving forces.

4.2 Detached breakwater

The detached breakwater test case was modelled using both ARTEMIS and FDWAVE as the wave model, and also with PISCES. Comparisons were carried out of the wave height, the set-up and the current variation through the vertical. Flow modelling was carried out using both TELEMAC-2D and TELEMAC-3D. The results from these tests are presented in Figures 2.1 to 2.8.

4.2.1 Wave heights

Although there were few experimental results for the wave height, ARTEMIS and FDWAVE both appeared to provide a good representation of the wave height. The mesh used for ARTEMIS had 6669 nodes and 12880 elements. In Figure 2.1, a representation of the wave field from ARTEMIS is shown, including the breaking ratio, showing the location of the breaker line. The result seems to be fairly good except for the area in front of the breakwater where there is too much reflection, making the wave height too high.

4.2.2 Wave set-up

The wave-driving forces computed in a variety of ways from ARTEMIS and from FDWAVE, which are represented in Figure 2.2, are very different. The result coming from the differentiation of the radiation stress in ARTEMIS (red) and the result from FDWAVE (pink) are the direct outputs of the wave models. The other curves represent the driving forces computed using other formula. These curves represent the driving forces computed from the dissipation. The variables used to compute the dissipation came from the ARTEMIS results. The Battjes curve should be similar to the FDWAVE curve as they use the same equation for the dissipation but unfortunately they are different. After the breaking the results are similar but before the breaking there is a greater difference. The problem is in estimating the location of the breaker line (Figure 2.1). It is relatively easy to visualise this line, using for example, the breaking ratio but unfortunately the breaker line does not follow a regular curve and it is quite difficult to represent it. The curve representing the Mizuguchi model (black) also appeared to be good after the breaking. On the other hand the Dally's curve (green) was much too small.

The ARTEMIS forces (derivative), the FDWAVE forces (Battjes) and the forces coming from the derivative of the Battjes dissipation were tested in the flow models. The forces in this last case were set equal to 0 at about 10 m from the still water dry land. It would have been better to follow the breaker line exactly but this was difficult to achieve and therefore this was the best way to remove the force which appeared in front of the breakwater due to the occurrence of reflection.

It is interesting to see that the forces computed using the derivative of the radiation stresses are completely different from the forces computed by the other models. For each one the peak of the force occurs just after breaking, but using the derivative method the value of the force stays nearly constant after the breaking.

The flow model (TELEMAC) was run with 1626 nodes and 3604 elements. The time step was 0.5 second and it was run for 120 seconds. The 3D model used 12 layers

The water level set-up was computed for several profiles

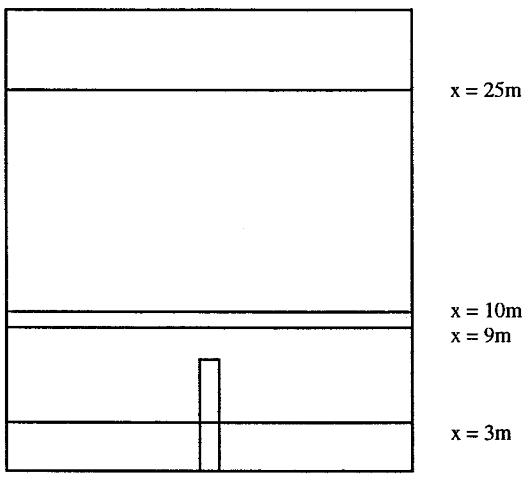

Presentation of each curve:

Name	Resarte07	Resarte 1	Resartediss	Resfdwave07	Resfdwave1	Res3darterol	Res3dfd	Res3fdrol
2d model	X	X	X	X	X			
3d model						X	X	X
Forces from	ARTEMIS	ARTEMIS	ARTEMIS	FDWAVE	FDWAVE	ARTEMIS	FDWAVE	FDWAVE
Forces Multiplied	0.7	1	1	0.7	1	1	1	1
Roller						X		X
Forces Applied						vertical	surface	vertical

Resartediss represents the forces which were computed using the dissipation calculated with the Battjes formula and with the ARTEMIS results.

The first way to analyse this result is to compare the shape of the curves. Obviously the curve representing the dissipation derived from ARTEMIS is the worst result because there are too many oscillations.

Offshore the set-up should be nearly equal to 0 but all the 3D model results give a clearly negative value. This is because there are boundary walls around the domain, so the volume cannot vary and if the level increases close to the shore it should decrease offshore.

The set-up results coming from FDWAVE after the breaking are quite similar for the same wave-driving force, whether the flow model used is 2D or 3D and whichever distribution of the force in the vertical direction is input. The set-up is more or less the same for each of these models.

The same phenomenon occurs for results for the set-up using wave-driving forces computed from ARTEMIS. The set-up depends not only on the forces but on the friction as well. It is also interesting to see the importance of the coefficient for the driving forces. 0.7 or 1 could give a very different result. Therefore this coefficient should be well defined. However, apart from the curve representing the dissipation derived from ARTEMIS, all the curves are quite similar and all give a reasonable answer.

In Figure 2.3, there is a comparison of the set-up for different profiles and in Figure 2.4, a comparison with the experimental data along the line x=9m is shown. The curve representing the dissipation using ARTEMIS is obviously not in good agreement with the data and two other models overestimate the set-up (the 2D flow model and 3D flow model with roller using the wave-driving forces from ARTEMIS). It is also worth noticing that, with the exception of the experimental measurement closest to the shore, all the other curves give a good representation of the set-up. There is a maximum difference of 3 mm between the numerical data and the experimental data which is quite satisfactory. It is interesting to see that the ARTEMIS result with the forces multiplied by 0.7 gives a very accurate result.

In summary the set-up is well represented using FDWAVE or ARTEMIS if corrected by a coefficient of 0.7. The 2D and the 3D models give fairly similar set-up apart from the set-up offshore which is quite well modelled by the 3D model when it is not too far offshore.

4.2.3 Currents

In Figure 2.5, there are vector diagrams representing the current behind the breakwater for different model results and measurments. There is a quiescent area in the experimental model which is not very well modelled in the numerical models. The current around this quiescent area does not give a good result either. The results obtained from ARTEMIS are relatively good except for those in the domain above this either. The results obtained from ARTEMIS are relatively good except for those in the domain above this quiescent area. The current is generally stronger in the experimental data than in the numerical models. A few models were tested, in the paper written by Pechon, 1996, but none of them gave an accurate representation of the current.

It was also interesting to obtain a representation of the current at different layers. It allows the effect of the friction and the effect of the roller to be visualised.

The TELEMAC-3D model using wave-driving forces computed from ARTEMIS results gives an accurate result for the current behind the breakwater. The other part of the domain which is not the area for the comparison and which was not detailed as much as behind the breakwater gives a result for the current which is less accurate (Figure 2.6).

Figures 2.7 and 2.8 show the results of inputting the forces at the surface or distributing the force through the depth and adding a roller effect. The results are quite different. Unfortunately there were no experimental data available to compare with the velocity distribution through the vertical.

This case has shown again the value of applying a factor of 0.7 to the driving forces as obtained using ARTEMIS. It has shown too that the use of the standard driving force output from ARTEMIS, making use of the derivative of the radiation stress gives a result at odds with the other techniques used to create the wave-driving forces, in that beyond the breaker line the wave-driving force is approximately constant.The TELEMAC-3D model using wave-driving forces computed from ARTEMIS results gives an accurate result for the current behind the breakwater. The other part of the domain which is not the area for the comparison and which was not detailed as much as behind the breakwater gives a result for the current which is less accurate.

4.3 Beach cusps

Simulations of the case of the cusps in the UKCRF have been carried out using PISCES, FDWAVE, ARTEMIS and TELEMAC-2D and TELEMAC-3D. The results for the beach cusp tests are presented in Figures 3.1 to 3.16.

4.3.1 Wave heights

The ARTEMIS wave simulation made use of 77022 nodes and 152842 elements. Several tests were carried out. One with the smoothing, one without and one with a wave coming with an angle (20 degrees).

Using FDWAVE, the number of nodes is smaller, because the equations solved do not need so many nodes per wavelength and the run time is considerably quicker.

4.3.2 Wave set-up

The driving forces coming from the wave models give very different answers (Figure 3.2). It is clear to see that the forces coming from ARTEMIS are much larger than those coming from FDWAVE.

For the 2D model three tests were carried out:

FDWAVE + TIDEFLOW (PISCES)
FDWAVE + TELEMAC-2D
ARTEMIS + TELEMAC-2D

In the first part of the study, the comparison is carried out only between the results coming from FDWAVE.

4.3.3 Currents

In Figure 3.3, a comparison for Case A between PISCES, TELEMAC2D and the experimental model is carried out. The value of the peak of velocity is smaller in the numerical models than in the experimental model. The direction of the current is not very accurate.

In Figure 3.4, the same comparison is shown for Case B, which is similar to Case A (same direction of propagation). The values of the peak velocity are still less accurate (by 15 %), but in TELEMAC the direction is not precisely representative of the physical model. In PISCES, the velocity is still smaller (by 25 %) but the direction is quite good. The values used were perhaps not recorded at the same point, because the co-ordinates of each of the measured points were not given. Therefore the percentage given is not entirely reliable but gives a good range of values.

In Figure 3.5, a comparison for Case C (waves propagating with an angle) is shown. The current is nearly the same for the peak values of TELEMAC and the experimental model (with 8 % difference). The direction is also fairly good. In PISCES the values of the peak velocity are smaller (by 18%) but the direction of the flow is the same as in the physical model.

From the results it appears that with a wave propagating at an angle not equal to 0 (normal incidence), TELEMAC will give good results. This is due to the boundaries (Figure 3.6). In TELEMAC there is a boundary which does not allow the flow to go into the domain. Therefore, there is a large recirculation in the whole domain, which does not affect the current along the shore. If there is no wave angle, then the domain is divided into two large parts, which are very different from the physical model. It is interesting to see that even though the result of the current is not accurate near the boundaries, further from them, around the cusps, the result of the current seems fairly precise.

In the second part of this study, only Case A is studied because it is the most typical case even though as was said before, it is fairly difficult to model.

Three 3D cases were carried out. They represent the forces imported into TELEMAC using the results from ARTEMIS and FDWAVE. The distribution of the force is either at the surface or along the vertical but with a roller effect.

First a comparison between the 2D and the 3D flow model results using FDWAVE and ARTEMIS is carried out. In Figure 3.7, the 2D and the 3D results for each wave model are similar. The 2D model of ARTEMIS is closer to the 3D model of ARTEMIS than to the 2D model of FDWAVE. However differences remain between the 2D and the 3D model. The 3D model of FDWAVE with the roller is closer to the 2D model than to the 3D model with forces applied at the surface. The current in this last case is stronger than in the 3D model with the roller.

The distribution of the force is a major problem in this case. The comparison between the 3D results of FDWAVE with the force at the surface, or along the vertical, show that there is a strong difference.

The problem of symmetry is more apparent when the driving forces are imposed at the surface, because sections A and C should give exactly the same answer but in Figure 3.8, 3.9 and 3.10, the 3D result is different. This is particularly true for the Figure 3.9. A result like this one is to be expected. If all the forces were applied at one point, then the model would be less stable than if these forces were applied throughout the vertical.

In Figure 3.11, the comparison of the depth-integrated result is carried out. The results from ARTEMIS are relatively accurate compared with the results from FDWAVE. The velocity is of the correct order and the direction is fairly reliable.

At the point A (location shown in Figure 3.12), the current along the vertical was measured. In Figures 3.13, 3.14 and 3.15, there is a comparison of the numerical results with the experimental data for the point A. The best result comes from ARTEMIS which provides a good result for the current.

For this test, the results coming from ARTEMIS seem to be the most accurate. The difference could come from the interpolation on the new mesh. Because FDWAVE and ARTEMIS do not use the same mesh then when the results are interpolated onto the mesh used by TELEMAC, a small shift in the position could appear. For a case, like this one, where the symmetry is very important, that could modify the results.

It is difficult to obtain other experimental data for this problem. For instance section B in the domain of interest is only 10 cm deep and for this depth at least five points would be needed to resolve the current. Furthermore, it is necessary to keep in mind that this numerical model is a wave period averaged model, so the current should also be integrated through this period. All these conditions mean that it is difficult to obtain accurate measurements.

In Figure 3.16 the secondary current behind the cusps is represented. It was impossible to reproduce this current due to the assumptions made for this case. A wave-averaged flow model is used and therefore it was not possible to represent effects that occurred in the swash zone.

This case is the most time consuming in terms of the run time. Because of the cusps, the water level (around them) is very shallow (Figure 3.1). This, together with the wavelength criteria (at least 12 nodes per wavelength), makes the run time longer. For example, each run of ARTEMIS lasts about 30 hours. The machine should also have a large RAM because the length of the vector used in ARTEMIS is very large.

This case has shown how the important features of the observed flow have been reproduced in 2D and 3D flow models. The wave-driving forces were greater in ARTEMIS than FDWAVE and the ARTEMIS simulations were generally more accurate than FDWAVE in this case. The results of simulation with PISCES were similar to those using FWAVE and TELEMAC2D. It was also found that the 2D models gave very similar results to the depth-integrated results found with the 3D models.

4.4 Groyne

The groyne test case was used for both an unsubmerged and a submerged groyne. The results of these tests are presented in Figures 4.1 to 4.8.

4.4.1 Unsubmerged groyne

The results of simulation of the groyne case using TELEMAC were compared with earlier studies carried out by Seed (1997). He used another flow modelling software – SSIIM. This program solves the Navier-Stokes equation with the k-ε model on a three-dimensional structured grid. SSIIM: (Sediment Simulation In Intakes with Multiblock Option) was developed by Nils Olsen at the Norwegian Institute of Technology, 1994,University of Trondheim. It uses a control volume method to solve the k-ε model. It has been used to model river flows with sediment transport. SSIIM solves the Navier-Stokes equation on a three dimensional structured grid, which is non-orthogonal in plan but regular in the vertical direction.

Many tests were carried out on this problem because, despite the apparently straightforward nature of this case, it is unfortunately quite complicated. The first problem is the resolution of the model. In order to obtain a good resolution around the groyne, the size of the mesh needs to be very small, as previously found by Seed. Therefore the model can take longer to run. The other problem was deciding where to start the model. The starting point should not be too close to the groyne, in order to avoid reflection from the groyne, nor too far away in order that a finer mesh can be used.

The domain used for the TELEMAC modelling was the same size as the experiment (15m x 2.3m); Seed used a much smaller domain (8m long).

Two tests were carried out with the 2D model, with slightly different meshes. In the first case, the entrance was quite close to the groyne and the boundaries were set as prescribed boundary values. The discharge was specified at the entrance and the elevation at the exit. This model produced some oscillations at the entrance. A simple way to avoid these oscillations was to impose a radiation-type boundary condition at the entrance (Thompson boundary condition) as was done in the second case.

a) First case:

In Figure 4.1, a comparison between the 2D and the 3D models is shown. The length of the recirculation zone with the 2D model has a value equal to approximately 4.8 m, which is 12 times the length of the groyne. However the recirculation length in the 3D model is about 8 times the length of the groyne. The width of the recirculation is approximately 0.68m, which is 1.7 times the length of the groyne. The recirculation width is estimated from the maximum width of the plan velocity contour ($V/V_{mean}= 0.5$) at mid-depth. Using this formula, the width is slightly different and the new length is about 1.45 times the length of the groyne for the 2D model and about 1.2 times for the 3D model. The theoretical study carried out by Todten in 1975 found that the recirculation zone had a maximum width of 1.67 L and a maximum recirculation length of 12.5 L (L: length of the groyne). Therefore the 2D case gives an accurate result and the 3D model is not as precise. As it is possible to see, just in front of the groyne the velocity profile does not does not appear to be very accurate, therefore another test was carried out using another mesh (coarser around the groyne). In Figure 4.2, a comparison is carried out between the two 3D models which shows an improved result with the coarse mesh. The new length of recirculation is now 5.6 m (14 times the length of the groyne), and the width is 1.4 times the length of the groyne.

The mesh used for the model and the length of the recirculation is shown in Figure 4.3.

In the vertical profile, (Figure 4.4), the general pattern of the flow from the experimental data is:

- A general reduction of velocities
- Velocities higher near the bed than at the surface
- No reverse flow

Comparison of the results between TELEMAC-3D and the experimental data

The top figure represents the flow close to the wall (10-cm from the wall). The numerical results are not very accurate. This may be mainly due to the friction. The velocity at the bottom is much higher than in the model. On the other hand the depth-average velocity seems to be similar. The velocity is nearly zero at the free surface in the physical model and therefore it balances the velocity at the bottom. There is no reverse flow; this is a main difference compared with the SSIIM simulations.

In the next figure, 20 cm from the wall, the results are better. The velocity close to the groyne is still underestimated but the value of the current is now in the same order. On this graph only the velocity along the x direction is represented but the direction of the depth-integrated current using TELEMAC shows that the direction of the current close to the groyne has now a significant y-component. This effect is increasingly influential approaching the tip of the groyne and therefore it means that even with a 30 % change in the x component, the norm of the vector representing the velocity will not be greatly affected.

The results of the flow in the section passing by the tip of the groyne should be interpreted cautiously. The flow varies widely between the left and the right corners of the tip. Even in the physical model there is a difference of almost 50% between the left and right corners. It is quite difficult to give a reliable comparison of the value of the current. However, the direction is not the same in both cases. In TELEMAC, the direction is mainly following the y direction whereas in the physical model the direction is mainly in the x direction. This could also be due to the shape of the groyne. In the physical model the shape of the tip of the groyne is semi-circular whereas in TELEMAC it is straight.

In the fourth and fifth cases, the comparison is more accurate, except for the section in the "continuity" of the tip. The velocity is underestimated in the numerical model but elsewhere the current is fairly well modelled. The velocity at the bottom is quite good which means that the friction coefficient has a reasonable value. Therefore the high value of the current in the top figure cannot be explained by the friction coefficient. There is probably an effect of the friction of the wall, which is not taken into account, but the numerical models do not seem to be very reliable close to the wall. The results are much better with TELEMAC than with SSIIM, but still need improvement. In the other part of the domain, TELEMAC gives very good results.

Comparison of the plan velocity vectors at different depths.

As was said in the previous chapter, TELEMAC results are accurate enough if not too close to the boundary. In Figure 4.5 and 4.6, around the tip of the groyne, the current is not well represented. In the upstream part of the model, the norm and the direction of the current are more or less accurate, but downstream the model underestimates the velocity and the direction is significantly different. It is worth noting that there are no main differences when the layers are compared. It is also interesting to note that the SSIIM model and the TELEMAC model have almost the same direction

In Figure 4.7, there is a representation of the velocity along the vertical. Even though TELEMAC3D does not give a noticeable variation, the velocity is in the same order as for the experimental values.

b) Second case:

In this case the Thompson formulation of the boundary conditions (a form of radiating boundary condition) was applied. The free surface is represented in Figure 4.8 to show that with these new boundary conditions, the oscillations have almost disappeared.

Two friction formulations were tested for this case:

A Chezy coefficient, 60, as in the 3D model
A Nikuradse coefficient: 0.1 (corresponding almost to a Chezy equal to 10)

This Nikuradse coefficient is rather high for this case but it will give an idea of the influence of the friction.

It is quite interesting that the length of the recirculation zone behind the groyne is considerably smaller with the Nikuradse coefficient. It is nearly half of the distance with the Chezy coefficient. It shows also that if this value equal to 0.1 accurately represents any flow in a port or in an estuary, then for a specific case like this one, the value must be completely different. The width in the Nikuradse model is equal to 0.52; with the Chezy model it is equal to 0.59 m. The ratio in each case is 1.3 for Nikuradse and 1.47 for Chezy.

It is also worth noting that with a high friction then the model has fewer oscillations than without friction.

The mean depth of the entire domain also differs: 0.188 m for Nikuradse and 0.182 m for Chezy

4.4.2 Submerged groyne

A test was also carried out using a submerged groyne using TELEMAC3D.

This test was run in similar conditions to the previous test except that the water level was increased up to 0.25 m. The discharge is also slightly different, 0.135 m^3/s instead of $0.131 m^3/s$. The height of the groyne is 0.2 m which means that the depth of water above the groyne is about 0.05 m.

Unfortunately the model has problems functioning. The problem seems to derive from the description of the groyne. TELEMAC is not the most suitable software for this case. Having a vertical wall is quite difficult to model, because the only way of describing it is by using the bathymetry and this leads to an interpolation between the node attached to the groyne and the groyne just in front or behind it.

4.5 Estuary training wall

Modelling tests were carried out to model the flows near to the training wall using a model of the Stour Orwell estuary. The bathymetry is shown in Figure 5.1. The results are presented in Figures 5.2 to 5.7.

The purpose was to represent the mean spring tide. The data used for this model came from the 19 July 1995. The comparison used the graph representing the current that was measured between:

HW-0.3 to HW+0.3 (Figure 5.2)
HW+0.5 to HW+1.5 (Figure 5.3)
HW+2.0 to HW+3.1 (Figure 5.4)
HW+4.5 to HW+5.3 (Figure 5.5)

The current was measured over a time interval of one hour. Therefore the velocity at the beginning of the measurement period may be different to that one hour later. To be able to compare these results, it was assumed that the velocity during the interval was constant and equal to the velocity at the middle of the time interval. This assumption was relatively correct in a part of the domain where the current has the same direction for the ebb or the flow but it was not accurate where the gyre appears.

Three 2D models and three 3D models were used for this case. The TELEMAC software provided the results.

4.5.1 Results from the 2D model

The k-ε model and the constant viscosity models of turbulence were used:

Two viscosity coefficient values were tested. One test was run with a low viscosity coefficient ($0.01 m^2/s$) and the other test was run with a high viscosity coefficient ($1\ m^2/s$).

The results from these models are very similar. It is relatively difficult to notice any difference between any of these models.

The comparison of these results with experimental data shows that the 2D model seems to be in the same range of magnitude for the velocity as the observed data.

4.5.2 Results from the 3D model

The turbulence model used for the 3D case was the mixing-length model. The horizontal viscosity coefficient was taken equal to $1\ m^2/s$. The difference between these tests came from the friction which was not the same (0.001 and 0.1 for the roughness length, Figure 5.6 and 5.7).

The comparison was carried out for the flow at the surface and the depth-integrated flow. The comparison shows that usually the 3D flow, with the small roughness length coefficient overpredicts the experimental results. It is particularly true for the flow at the surface.

The second result with the high roughness length coefficient is much better. A few points were compared in the domain along the time. The current velocity was in the correct range of order. A mean tide was also used to study the impact of the tide. The diminution of the amplitude of the current appeared which was expected.

The anti-clockwise circulation forming near the northwesterly end of the quay appears in each numerical model with more or less effect. The 3D models with a small friction have a large domain representing this circulation whereas the 3D model with the high friction has a relatively small domain.

For this test, the better results came from the 2D results and from the 3D model with a high friction. However this 3D model underestimates the size of the gyre. The 2D models seem to be slightly more reliable. This problem is very similar to the groyne case. As the bathymetry changes considerably between the dredged and the non-dredged area, it could be represented like a submerged groyne, which was difficult to model in the submerged groyne case. However these results are accurate slightly further. On the other hand, the 3D model was not necessary for this model because the velocity along the vertical is almost constant and in the same direction. In the gyre, where the velocity is almost equal to zero, then there could be a change of direction between the surface current and the bed current.

5. SUMMARY AND CONCLUSIONS

In this report the impact of structures on the flow field has been analysed using several numerical models in two and three dimensions. The experimental data (current velocity, wave height and set-up) were compared with the results of the numerical models. The PISCES, TELEMAC and ARTEMIS models were the ones mainly used for the tests. ARTEMIS seems to be the best program to obtain the wave height in theory, but it can be time-consuming to run and the wave-driving forces it produces are not entirely reliable. On the other hand FDWAVE (used in PISCES) is quicker to run, but it does not take fully into account all the wave transformation phenomena.

The results from the models as applied to the test situations can be summarised as:

5.1 Straight beach

This test has demonstrated the value of adopting the multiplying factor of 0.7 to the wave-driving forces resulting from ARTEMIS, as proposed by Pechon, and the sensitivity of the resulting velocity field to the selection of the vertical distribution of the driving forces. The best combination of currents and water level set-up is obtained with a uniform distribution through the vertical, enhanced by representation of the roller effect. In addition it was found that for practical applications it is necessary to use the wave smoothing option in ARTEMIS, because reflection from the beach can otherwise have too large an effect on the wave-driving forces.

5.2 Detached breakwater

This case has shown again the value of applying a factor of 0.7 to the driving forces as obtained using ARTEMIS. It has shown too that the use of the standard driving force output from ARTEMIS, making use of the derivative of the radiation stress gives a result at odds with the other techniques used to create the wave-driving forces, in that beyond the breaker line the wave-driving force is approximately constant. The TELEMAC-3D model, using wave-driving forces computed from ARTEMIS results, gives the most aaccurate result for the current behind the breakwater.

5.3 Beach cusps

This case has shown how the important features of the observed flow, with rip currents, have been reproduced in 2D and 3D flow models. The wave-driving forces were greater in ARTEMIS than FDWAVE and the ARTEMIS simulations were generally more accurate than FDWAVE in this case. The results of simulation with PISCES were similar to those using FDWAVE together with TELEMAC2D. It was found that the 2D models gave very similar results to the depth-integrated results found with the 3D models.

5.4 Groyne

It was relatively straightforward to obtain a general flow pattern, but to describe the current in the close vicinity of the groyne was a much tougher task. Even though the flow was successfully represented, the flow at the tip of the groyne did not reproduce the observed direction in the physical model. The roughness coefficient has a major effect for the length of the recirculation. It is also important in this case that a sufficiently long lead-in section is modelled to ensure the flow is not too affected by the groyne upstream.

5.5 Estuary training wall

The comparison with experimental data was not a simple task. However, it seems that the size of the gyre was slightly underestimated using the numerical model.. The friction and the model (2D or 3D) had a major impact on the current. The turbulence law that was chosen had almost no effect on the pattern of the flow.

5.6 General comments

The present project has combined state-of-the-art wave and flow modelling techniques, with the aim being to define the range of studies that might presently be undertaken using numerical modelling techniques and how the available models should be applied. The guidance derived from the tests carried out in this project can be summarised as:

The interaction between the wave model and the flow model is particularly time-consuming because the mesh is not usually the same for the flow and wave models. This means that the variables have to be interpolated on a new mesh. Moreover, to obtain a good degree of accuracy, the driving forces and the viscosity must be computed for the correct domain. This means that the formula for the viscosity after breaking is only valid behind the breaking line. As the location of the breaking line is difficult to model, it is therefore a problem to impose the viscosity (for example) at the correct point. The user has the choice whether to get an exact representation of the breaking line, which is time consuming, or to give an approximate line representing the breaking line and giving the appropriate values for the variables.

The driving forces computed using the dissipation (Dingemans) give better results than those using the derivative of the radiation stresses. This explains why the results obtained from FDWAVE are generally better than those from ARTEMIS. A distribution of the driving forces along the vertical with a roller is more appropriate than the forces imposed at the vertical. It is not however entirely perfect and a better distribution along the vertical should be sought.

The viscosity using the equations by Svendsen seems to be reliable for the turbulence.

The friction formulation was also tested; it was found that the value of the global friction had a greater effect than the friction from the breaking, therefore the priority is to obtain a correct value for the global friction.

The first comment about these results is the difficulty in recognising a 2D or a 3D problem. The models that seemed to be three-dimensional may in fact be more two-dimensional than the case with the breakwater, for example. Hence, before choosing a 2D or a 3D model, it is useful to know the purpose of the study. To model the undertow, the 3D results are very useful.

The results are wave-period integrated, so the strongest currents may not be fully represented with these numerical models. For example, due to this problem, it was not possible to model the secondary recirculation current behind the cusps. However this is only a first reliable step to model the flow around the structure. It is also a comparatively quick method that can be used to estimate the value of the current.

The models represented in this report produced accurate results in terms of wave height and set-up. The current was usually slightly underestimated.

For the flow-only test cases with no waves it was found that a two-dimensional depth-integrated model could give very good results except in the very close vicinity of the structure. For the straight beach the modelling can predict well the undertow phenomenon and for the cases with structures in a wave field two dimensional modelling again gives good results within the area where the waves have broken.

5.7 Overall conclusions

Benefits from the present study include a more confident modelling capability of flows driven by waves at structures resulting from the testing and comparison of the numerical models with laboratory experiments. Formulations that are appropriate for the wave-driving forces have been chosen and it has been found advisable to include the contribution from the roller when three-dimensional flows are to be simulated.

Based on the results of this study it is concluded that state-of-the-art numerical models, sufficiently calibrated by comparison with laboratory and site data, can be used predictively for all of the situations studied, except in the very close vicinity of the structures, where vertical accelerations (ignored in the flow models described here) may be important. For a channel flow situation the area of important vertical accelerations will not normally extend more than one water depth away from the structure.

During the study a number of programming developments have been found necessary and these are directly usable for studies:

- The wave-driving forces taken from the wave model (ARTEMIS or FDWAVE) have been incorporated into the TELEMAC-2D and TELEMAC-3D flow models.

- The wave-driving forces may need to be computed from the dissipation rate, rather than from differentiation of radiation stress

- The factor of 0.7 may need to be applied to the radiation stresses computed from ARTEMIS

- In 3D the possibilities include a uniform distribution of the driving force through the vertical with or without the addition of a roller effect.

- Also in 3D a viscosity formulation is computed and incorporated in the flow model

Future applications of this work will lead to the more routine application of three-dimensional modelling to the simulation of wave-driven flows at coastal structures. Three-dimensional models will also be used much more frequently in the future for engineering problems in rivers and estuaries. In order to model up to the very close vicinity of structures it will be necessary to use models that take full account of the three-dimensional flow field (the present generation of hydraulic three-dimensional models assume the pressure to be hydrostatic).

6. ACKNOWLEDGEMENTS

We wish to thank Harwich Haven Authority for the provision of ADCP current data measured in 1995, for the region of the gyre at the training wall near to Trinity Terminal. We would also like to thank Dr Alistair Borthwick of the Oxford University Engineering Department for providing data from the experiment on beach cusps carried out in the UKCRF.

The contribution to this work of Eric Michel from the University of Lyon is gratefully acknowledged.

We would like to thank Mr Ian Heijne of WS Atkins for his helpful and constructive comments on this report.

7. REFERENCES

- Arcilla A.S., Lemos C.M., Surf-zone Hydrodynamics. Centro Internacional de metodos numericos en ingeniera, Barcelona.

- Battjes J.A. and Janssen, Energy loss and set-up due to breaking of random waves. Proc. 16th Int. Conf. on Coastal Engineering, ASCE, Vol. 1, pp 649-660, 1978.

- Benque J.P., Cunge J.A, Feuillet J., Haugel A. and Holly F.M., ASCE. J Waterways, ports, coastal ocean div./108 (WW3), pp 396-417.

- Berkhoff J.C.W., Computation of combined refraction-diffraction. In Proc. 13rd International Conference on Coastal Engineering, pages 471-490, Vancouver, 1972.

- Berkhoff J.C.W., Booij N., Radder A.C., Verification of numerical wave propagation models for simple harmonic linear waves. Coastal Engineering, 6,1982, 255-279.

- Bettess P., Bettess J.A., A generalisation of the radiation stress tensor. Applied Math. Modelling, Vol.6, 1982.

- Bijker E.W., The increase of bed shear in a current due to wave motion. Proc 10th. Conf. Coastal Eng., ASCE, 1, pp 746-765, 1966.

- Booij N., A note on the accuracy of the mild slope equation Coastal Engineering, Vol. 7, 1983.

- Booij N., Gravity waves on water with non-uniform depth and current. Delft University of Tech., Dept Civil Eng., Rep. 81-1, 1981.

- Borthwick A.G.L., Cruz Leŏn S., Adaptive hierarchical meshing for localised modelling of shallow flows.

- Copeland G.J.M., A practical alternative to the mild-slope wave equation. Coastal Engineering, 9, pp125-149, 1985.

- Peet A.H, Damgaard J.S., COSMOS-k/t, Modelling cross-shore sediment transport within the surf-zone. Internal HR report, TR 38, 1998.

- Cox D.T., Kobayashi N., Undertow profiles in the bottom boundary layer under breaking waves. Proc. 25th Int. Cont. on Coastal Eng. ASCE, Orlando, 1996.

- Crapper G.D., Energy and momentum integrals for progressive capillary gravity waves, J. Fluid Mech., 94, pp 13-24, 1979.

- Dally W.R., Dean R.G. and Dalrymple R.A, A model for breaker decays on beaches, 19th Int. Conf. Coastal Eng., pp 82-98, 1984.

- De Vriend H.J. and Stive M.J.F., Quasi 3D modelling of nearshore currents. Coastal Engineering 11, 565-601, 1987.

- Dingemans M.W., Radder A.C., De Vriend H.J., Computation of the driving forces of wave-induced currents. Coastal Engineering, 11, pp 539-63, 1987.

- Gaillard P., Numerical modelling of wave-induced currents in the presence of coastal structures. Coastal Engineering 12, 63-81, 1988.
- Galvin C.J., Breaker type classification on three laboratory beaches, J.Geophysical res., Vol 73, pp 3651-3659, 1968.
- Girolamo P.D., Kostense J.K. and Dingemans M.W., Inclusion of wave breaking in a mild-slope model. Computer Modelling in Ocean Engineering, Schrefler and Zienkiewicz (eds) Rotterdam, p221-229, 1988.
- Jonsson I.J., Wave boundary layer and friction factors. 10th Int. Conf. Coastal Eng., pp 127-148, 1966.
- Jonsson I.J., Combinations of waves and currents in stability of tidal inlets by P. Bruun Elsevin, Amsterdam, pp 162-203, 1978.
- Jonsonn I.J. and Christoffersen J.B., Coastal Engineering, pp 1103-1117, 1984.
- Kirby J.T., A note on linear surface wave-current interaction over slowly varying topography, J. Geophys.,89 (C1):745-747, 1984.
- Kirby J.T., Propagation of weakly non-linear surface water waves in regions with varying depth and current. Univ, Delaware, Newark, USA, Research report no CE-83-37, 1983.
- Kirby J.T., Dalrymple R.A., An approximate model for non-linear dispersion in monochromatic wave propagation models. Coastal Engineering 9, 545-561, 1986.
- Kostense J.K., Dingemans M.W.,Van Den Bosh , Coastal Engineering, pp 32-46, 1988.
- Lamb M., Hydrodynamics, 6th edition, Cambridge U.Press, 1932.
- Li B., A generalised conjugate model for the mild slope equation. Coastal Engineering 23, 215-225, 1994.
- Li B. and Madrell R.J., A three dimensional model for wave induced currents. Coastal Engineering, pp 2297-2307, 1994.
- Li B., Anastasiou K., Efficient elliptic solvers for the mild-slope equation using the multigrid technique, Coastal Engineering, 16, 245-266, 1992.
- Liu, P.L-F., Wave-current interactions on a slowly varying topography, J. Geophys. Res., 88 (C7), 4421-4426, 1983.
- Longuet-Higgins and Stewart, Radiation stresses in water waves; a physical discussion with applications. Deep Sea Research,Vol.11, pp 529-562, 1964.
- Mizuguchi M., An heuristic model of wave height distribution in surf zone. Proc. 17th Int. Conf. On Coastal Eng., ASCE, Vol1, pp 277-289, 1981.
- Mory M., Hamm L., Wave, set-up and currents around a detached breakwater submitted to regular or random wave forces, 1996. Submitted to the Coastal Engineering.
- O'Connor B. and Yoo D., Mean bed friction of combined wave/current flow. Coastal Eng., 12, pp 1-21, 1988.

- Olsen N.R.B., SSIIM. A three-dimensional numerical model for simulation of water and sediment flow, HYDROSOFT-94, Porto Carras, Greece.
- Panchang V.G., Cushman-Roisin B., Pearce B.R., Combined refraction-diffraction of short waves in large coastal regions. Coastal Engineering, 12, 133-156, 1988.
- Panchang V.G., Pearce B.R., Solution of the mild slope wave problem by iteration. Applied Ocean engineering, 13, pp187-199, 1991.
- Pechon P. and Teisson C., Numerical modelling of three-dimensional wave-driven currents in the surf-zone. Coastal Engineering, pp 2502-2512, 1994.
- Pechon P. et al, Intercomparison of wave-driven currents models. LNH report, 1996.
- Radder A.C., On the parabolic equation method for water wave propagation J. Fluid Mech.,95, 159-176, 1979.
- Seed D.J., River training and channel protection. HR Wallingford Report, SR480, 1997.
- Soulsby R.L., Hamm L., Klopman G., Myrhaug D., Simons R.R. and Thomas G.P. Wave-current interaction within and outside the bottom boundary layer. Coastal Eng., 21,41-69,1993
- Southgate H.N., Prediction of wave breaking processes at the coastline. Internal report HR, 1995.
- Southgate H.N., Review of wave breaking in shallow water. Conference on Wave Kinematics and Environmental Forces, London, UK, 24-25 March 1993.
- Spaliviero F. and Seed D., 3D modelling of hydraulic structures. HR Wallingford Report, SR545, 1998.
- Svendsen A., Wave height and Set-up in the surf-zone, Coastal Eng., Vol 8, pp 303-329, 1984.
- Svendsen A. and Putrevu U., Nearshore circulation with 3D current profiles. Paper 116. 22nd international conf. On Coastal Eng, 1990.
- Yoo D. and O'Connor B., Mathematical modelling of wave-induced nearshore circulations. Coastal engineering, pp 1667-1681, 1986.
- Yoo D., Mathematical modelling of wave-current interacted flow in shallow waters. PhD thesis, University of Manchester, 1986.
- Yoo D. and O'Connor B., Mean bed friction of combined wave/current flow, Coastal Eng., 12, pp 1-21, 1988.

Figures

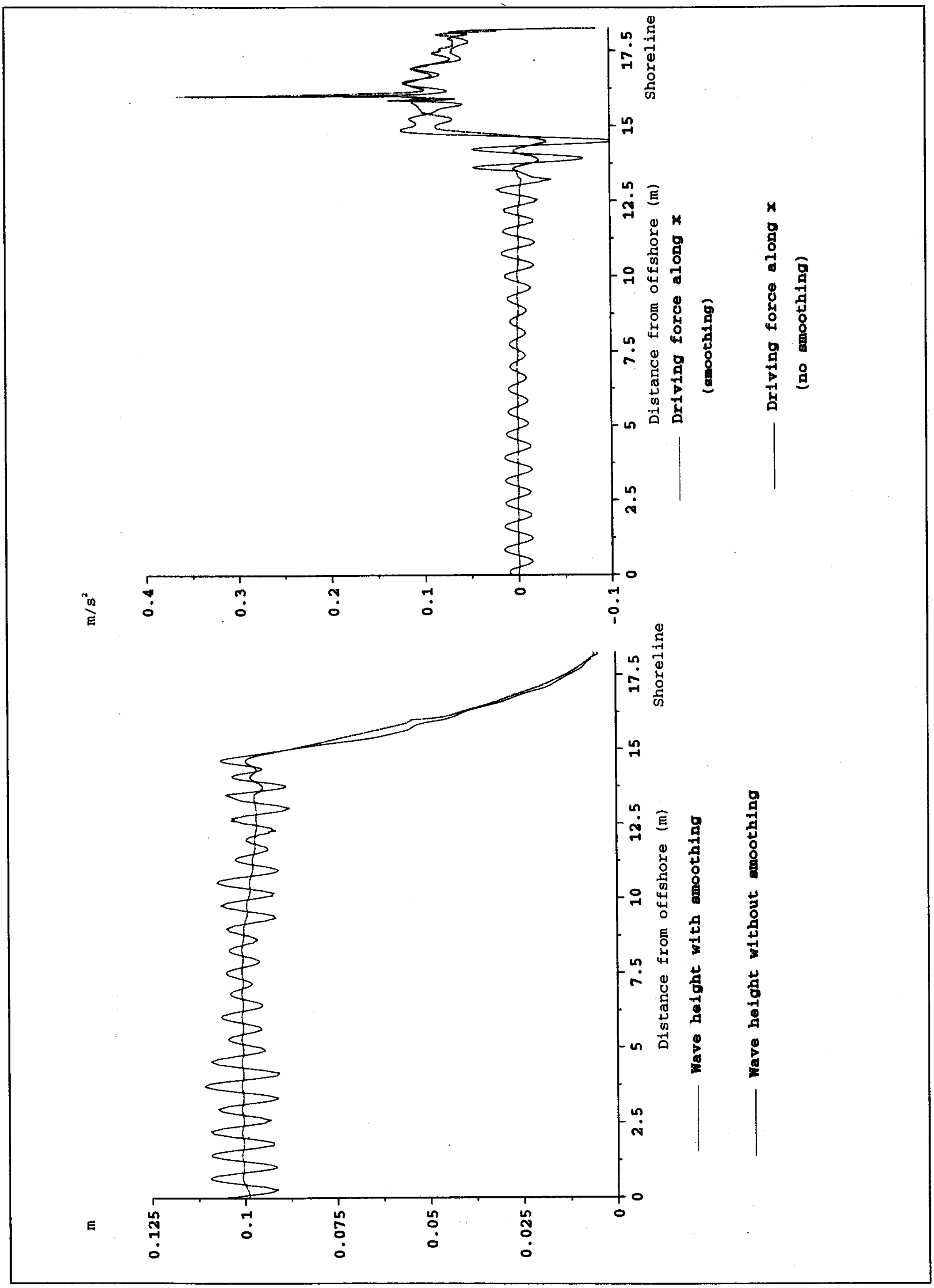

Figure 1.1 Comparison of the wave height using the smoothing criteria

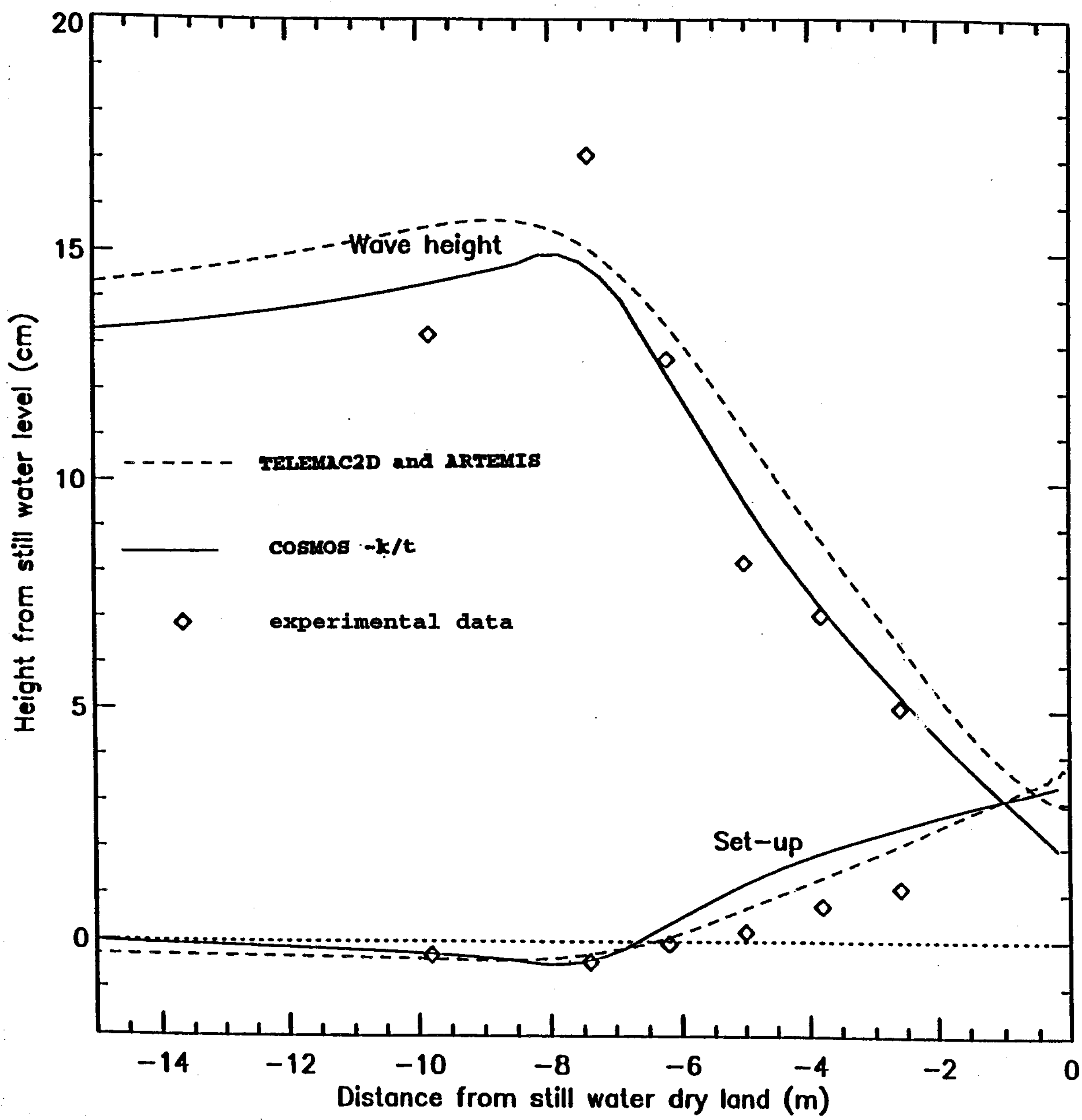

Figure 1.2 Comparison of the wave height with experimental data

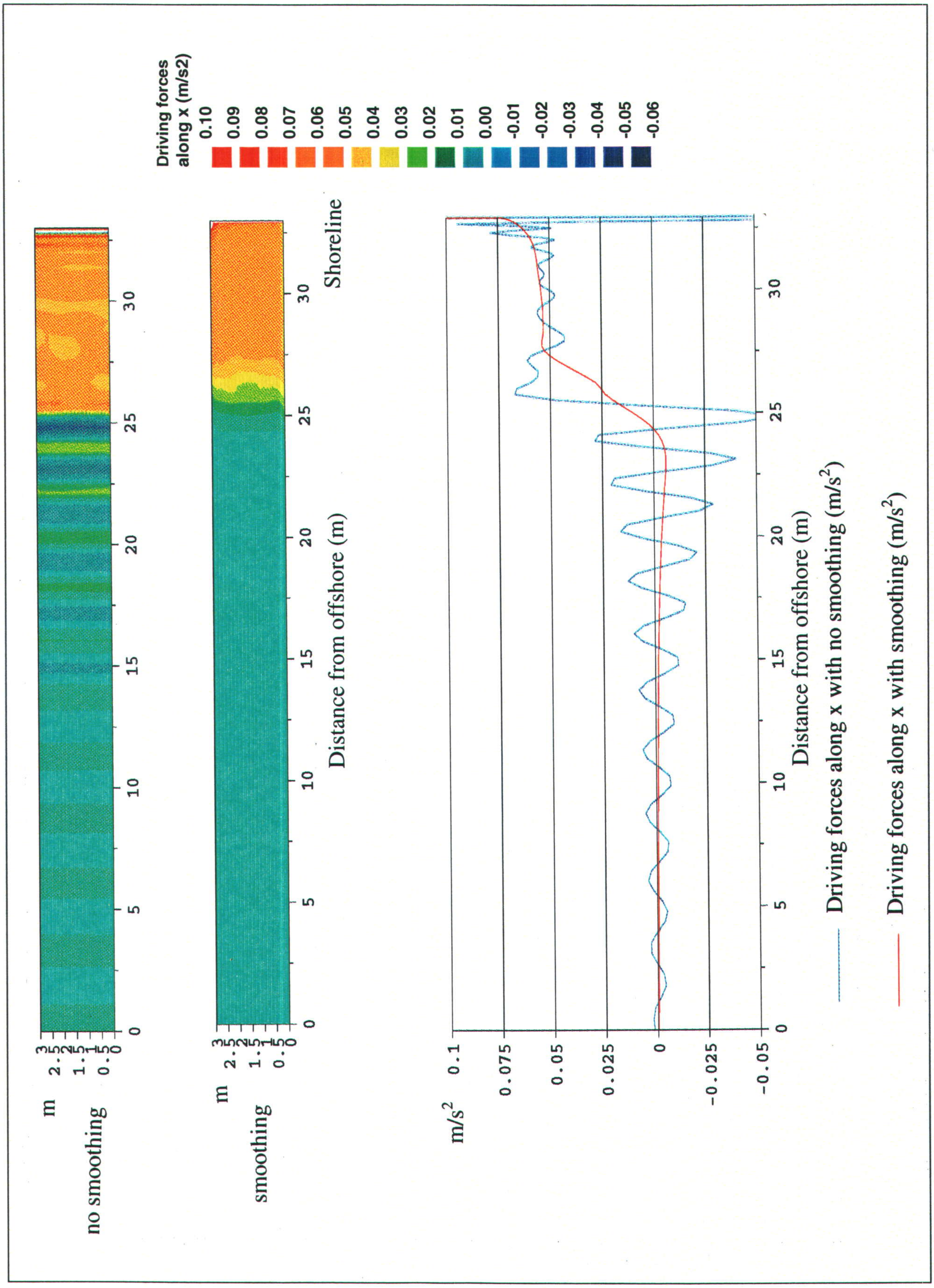

Figure 1.3 **Representation of the driving forces**

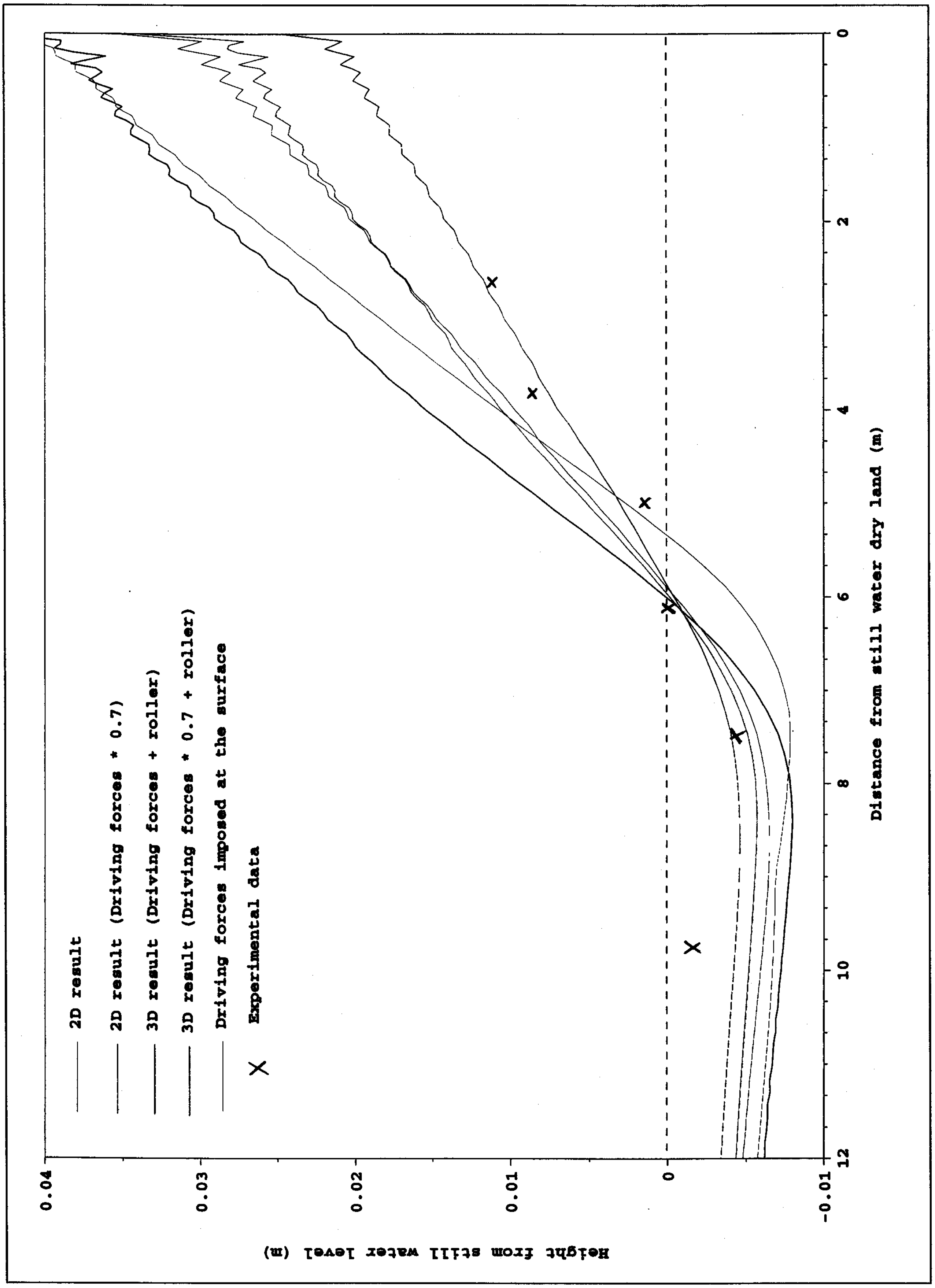

Figure 1.4 Comparison of the set-up

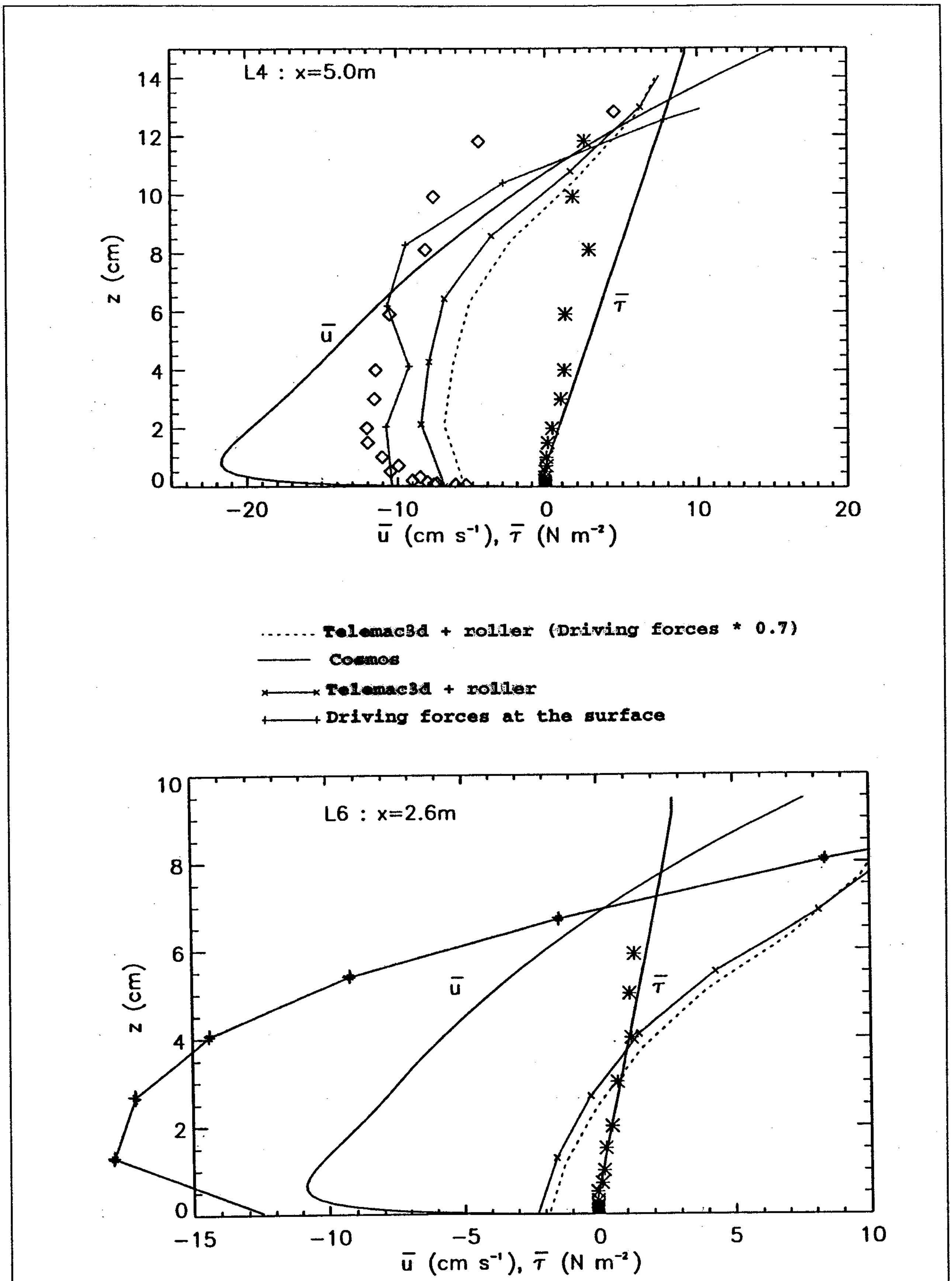

Figure 1.5 **Comparison of the vertical velocity profile, for varying distances from dry land**

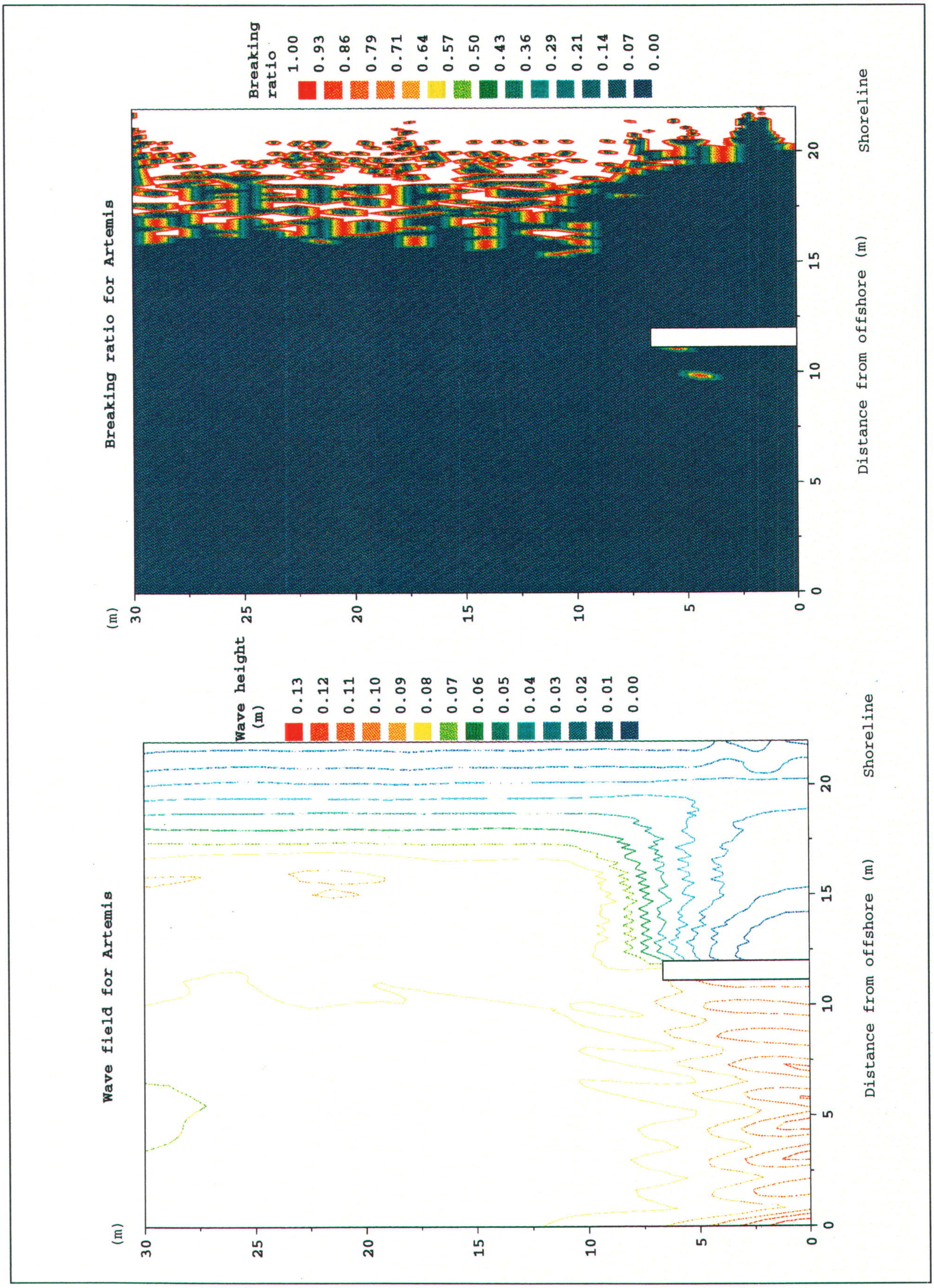

Figure 2.1 Wave field for ARTEMIS

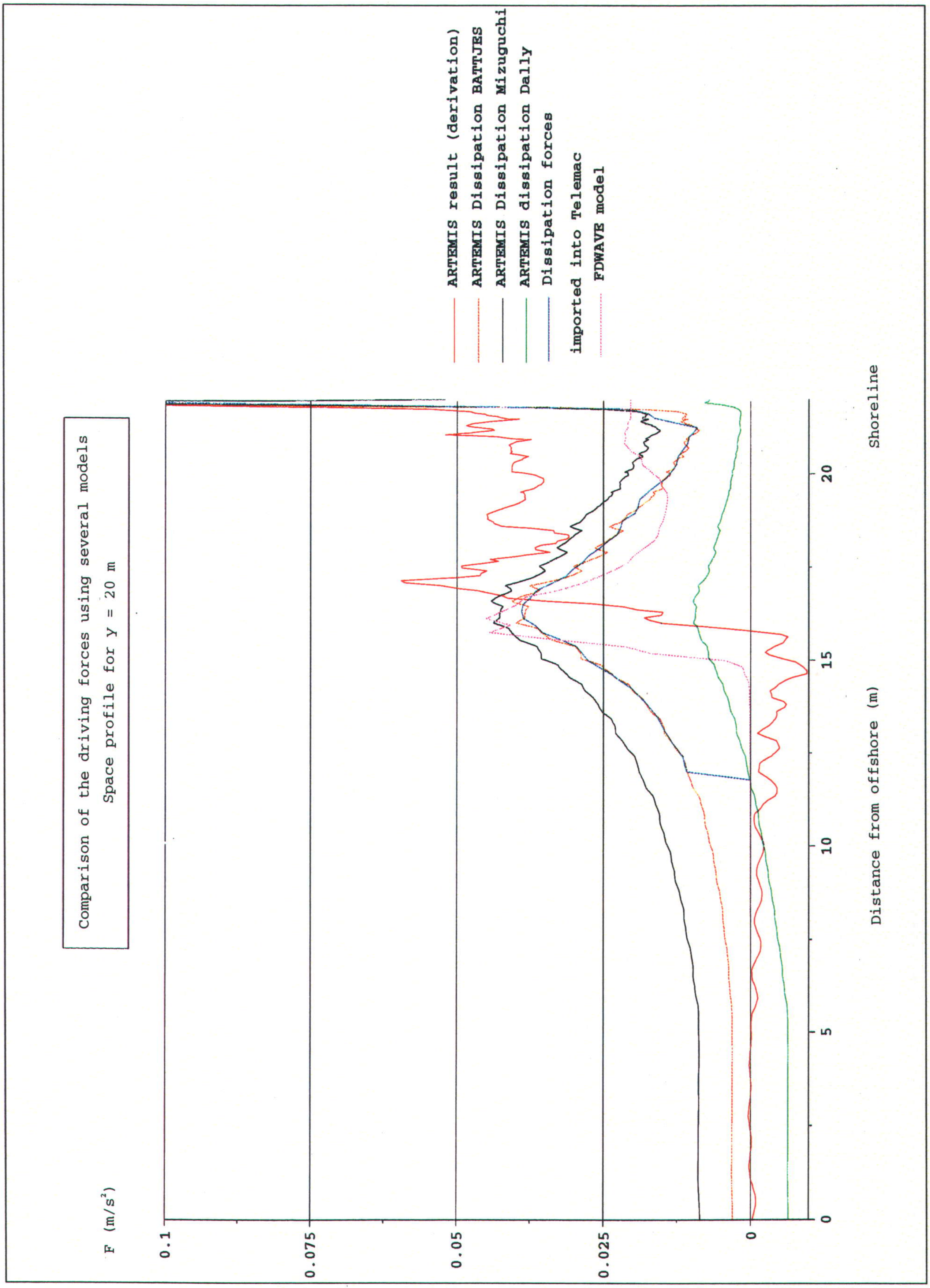

Figure 2.2 Driving forces for several models

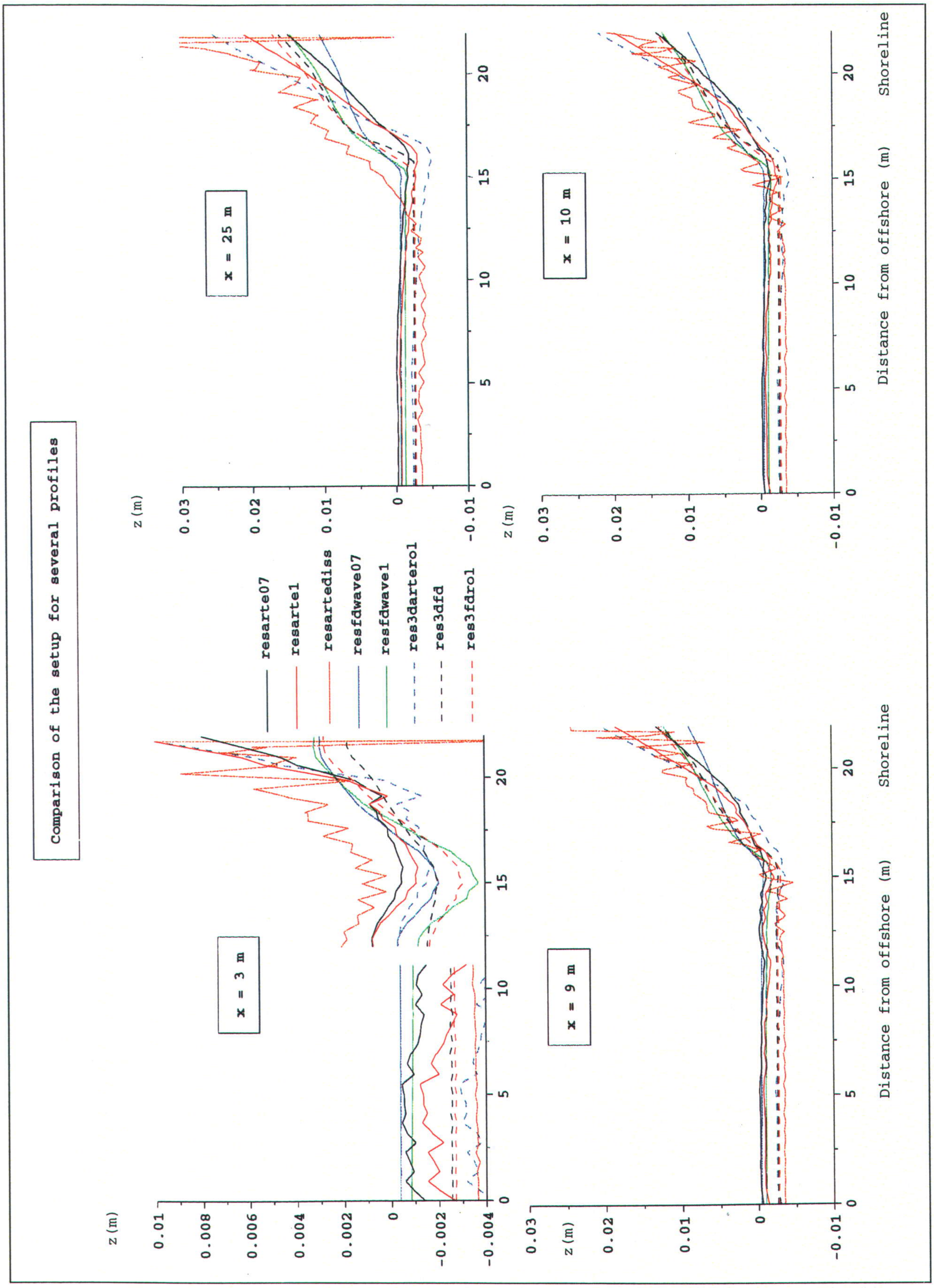

Figure 2.3 Representation of the set-up for several profiles

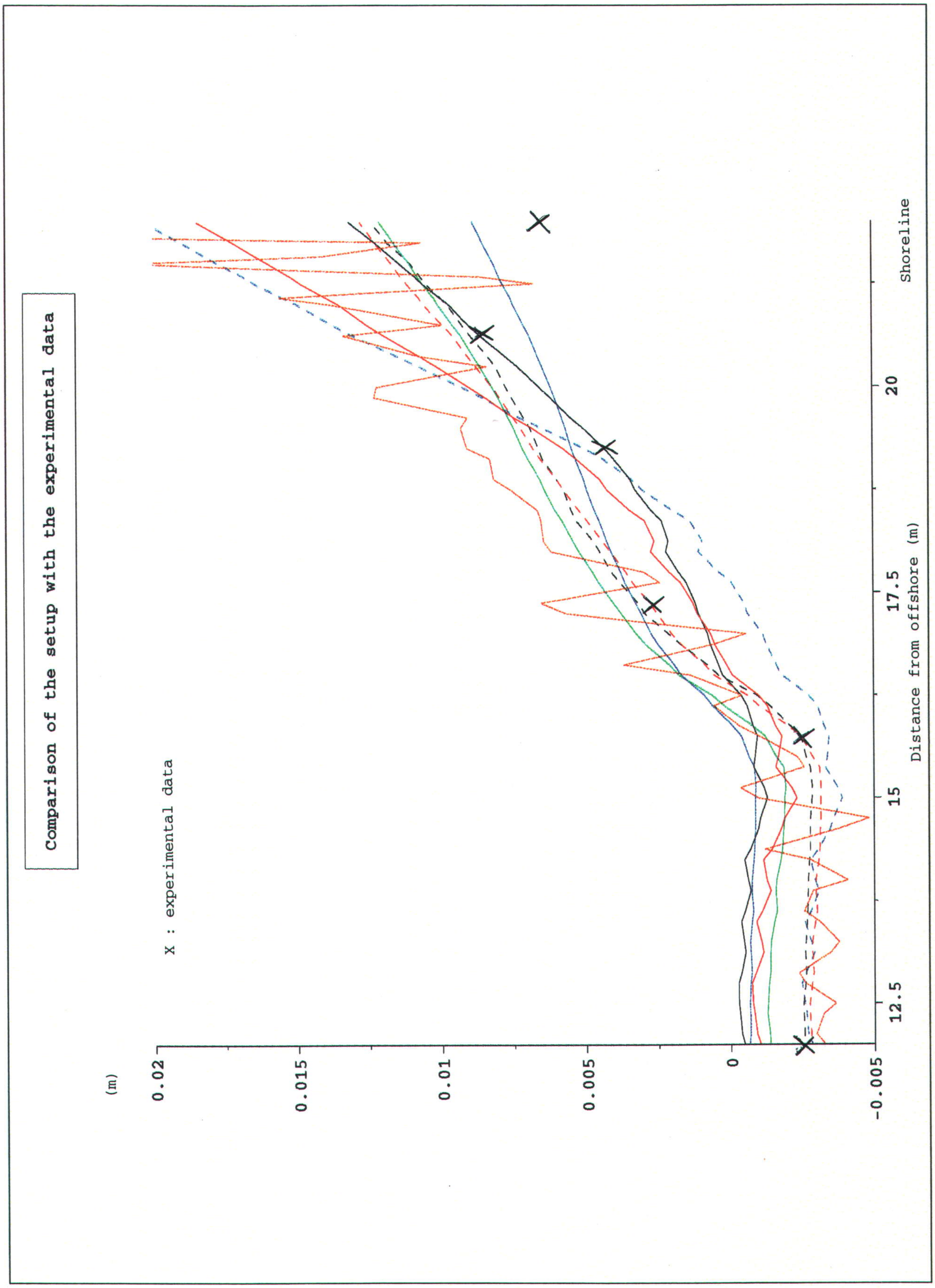

Figure 2.4 Representation of the set-up for x = 9 m

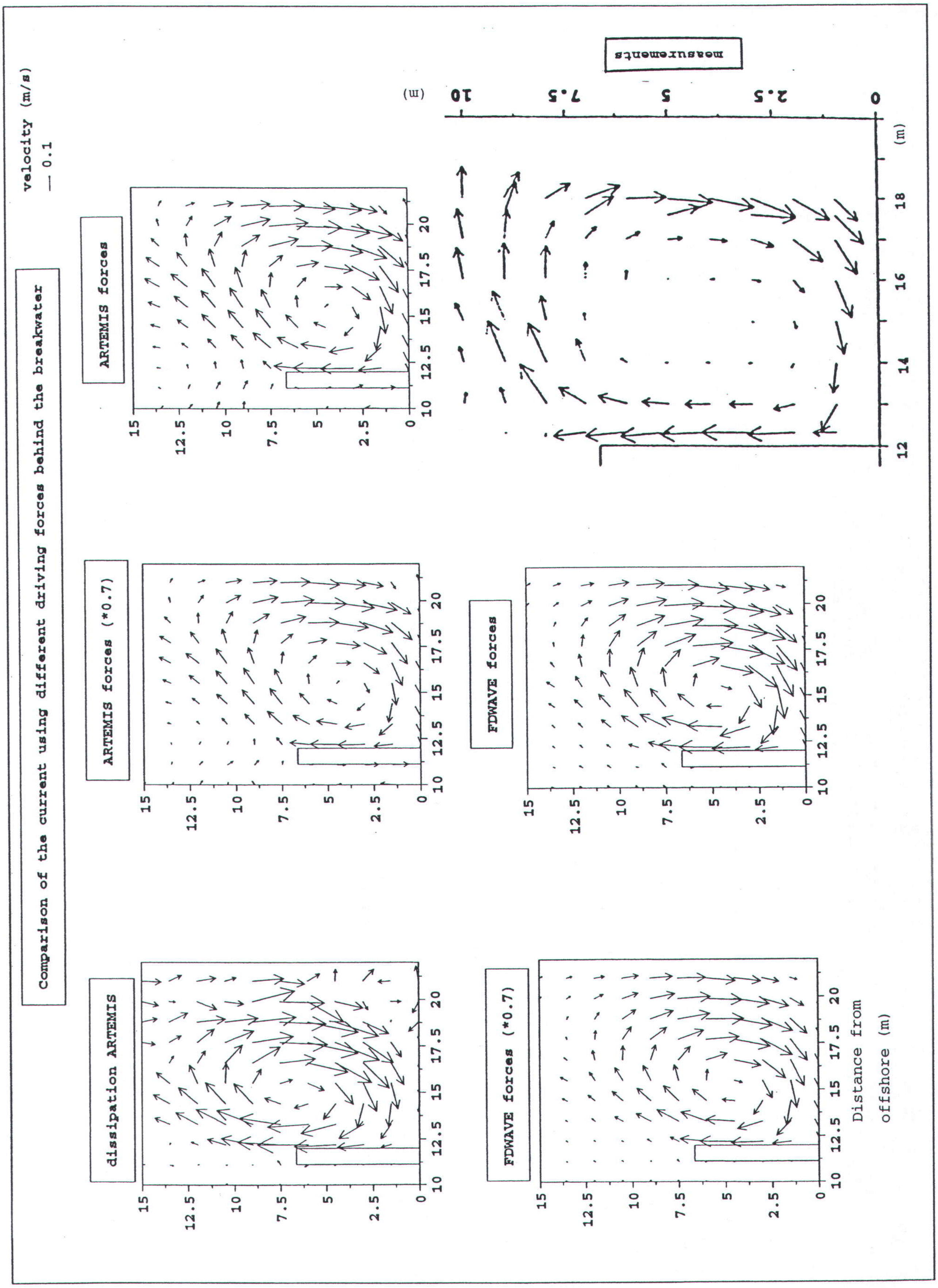

Figure 2.5 **Representation of the current behind the breakwater**

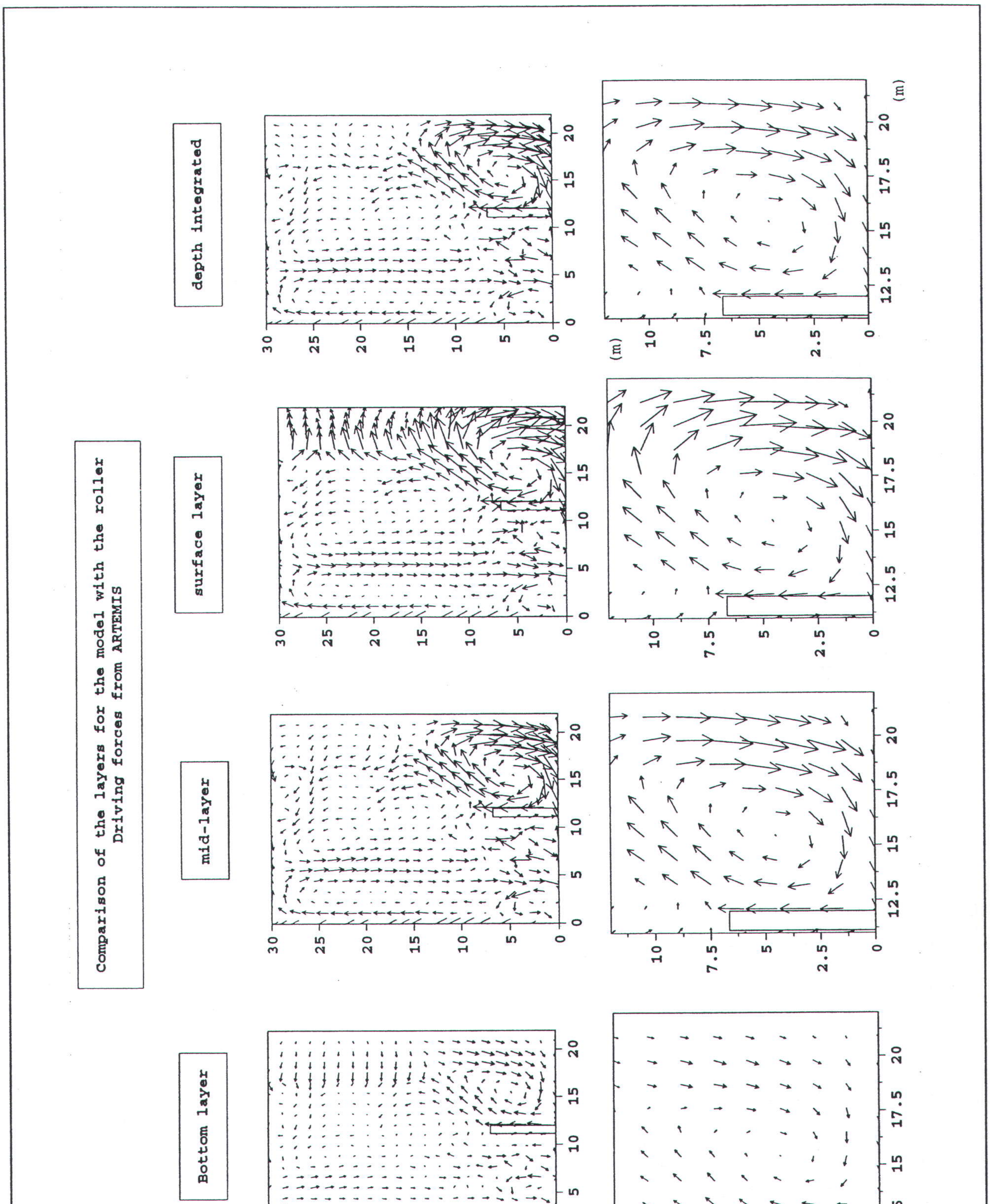

Figure 2.6 **Current using the driving forces of ARTEMIS with the roller**

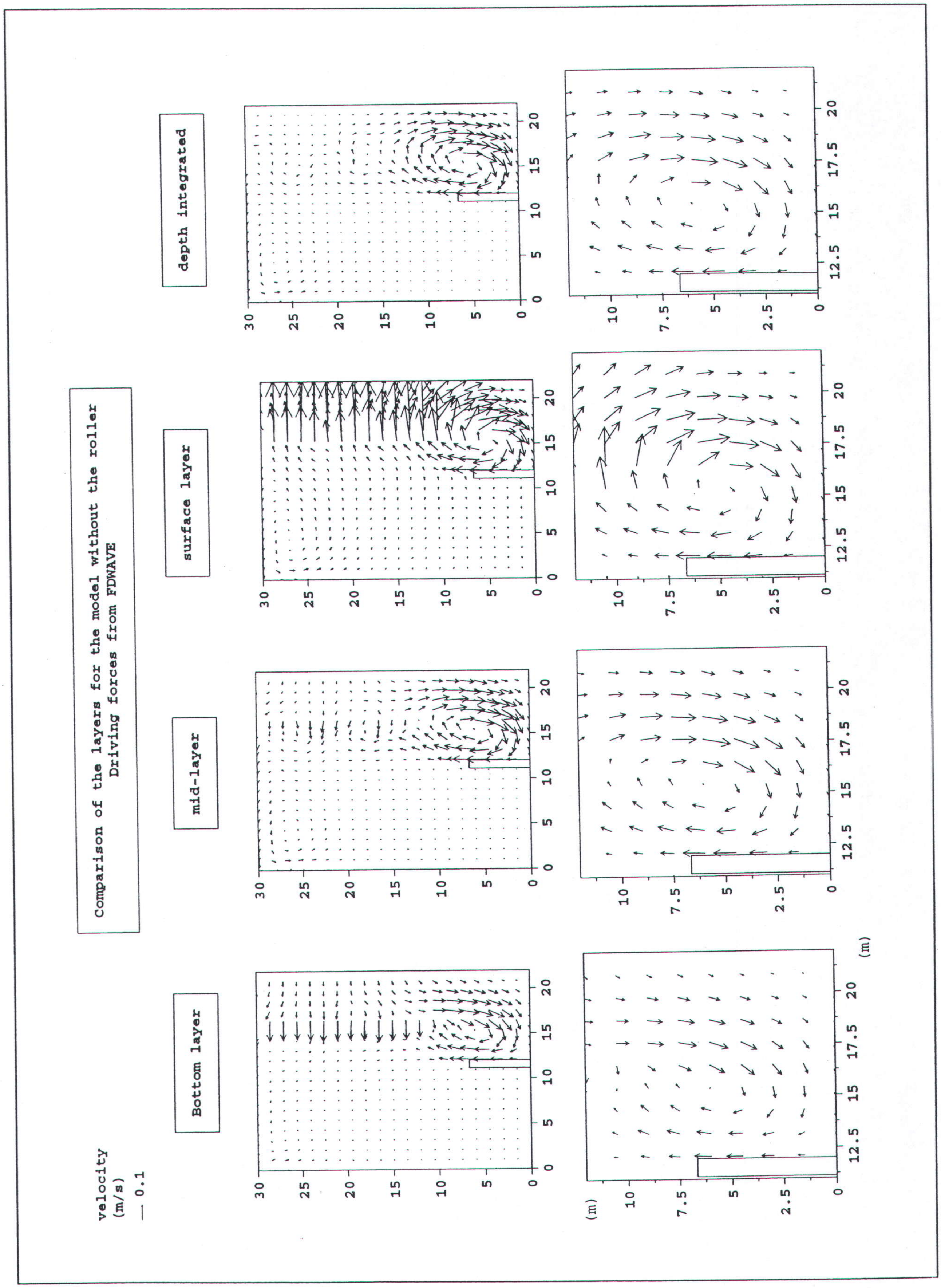

Figure 2.7 Current using the driving forces of FDWAVE imposed at the surface

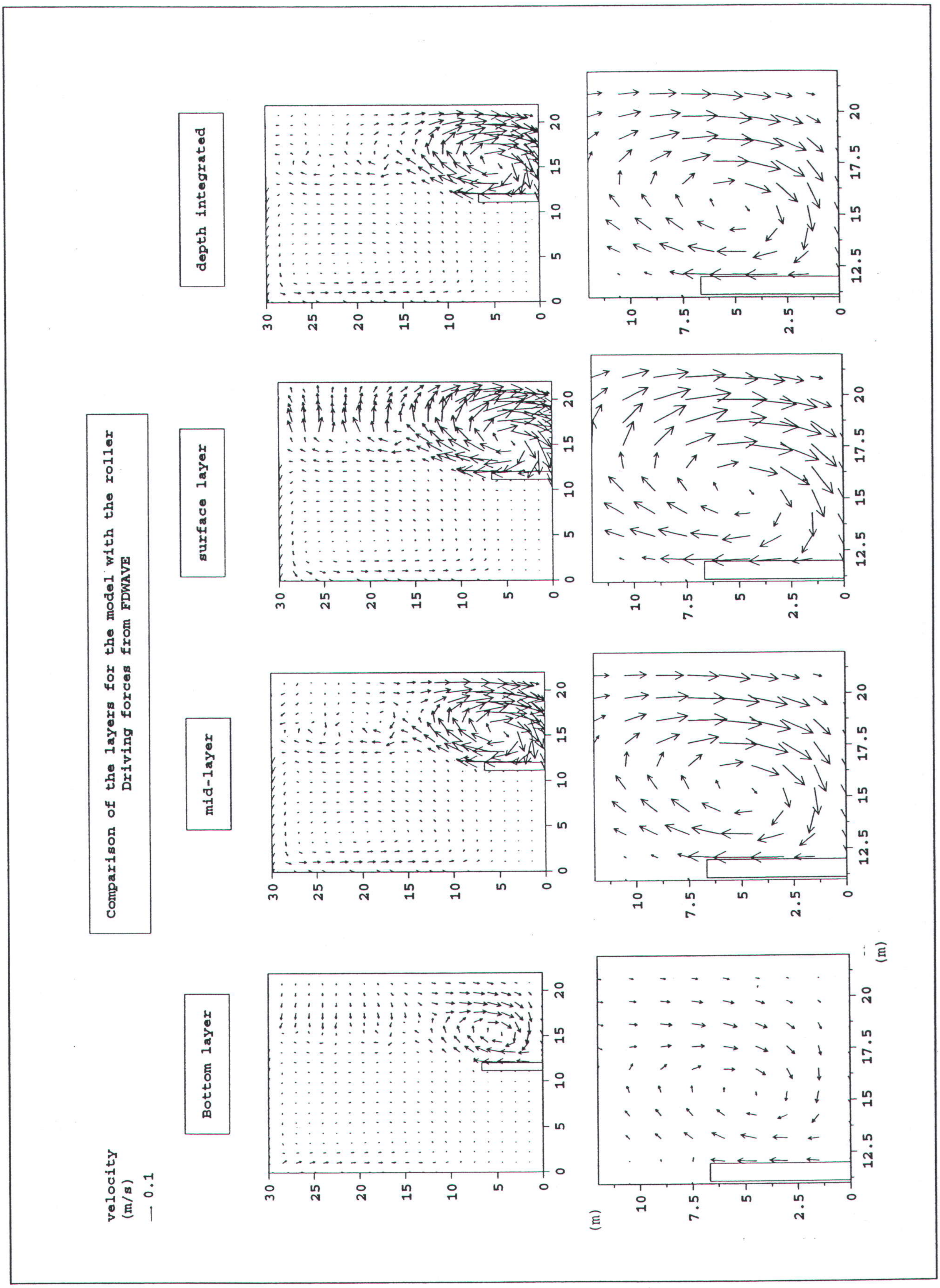

Figure 2.8 Current using the driving forces of FDWAVE with the roller

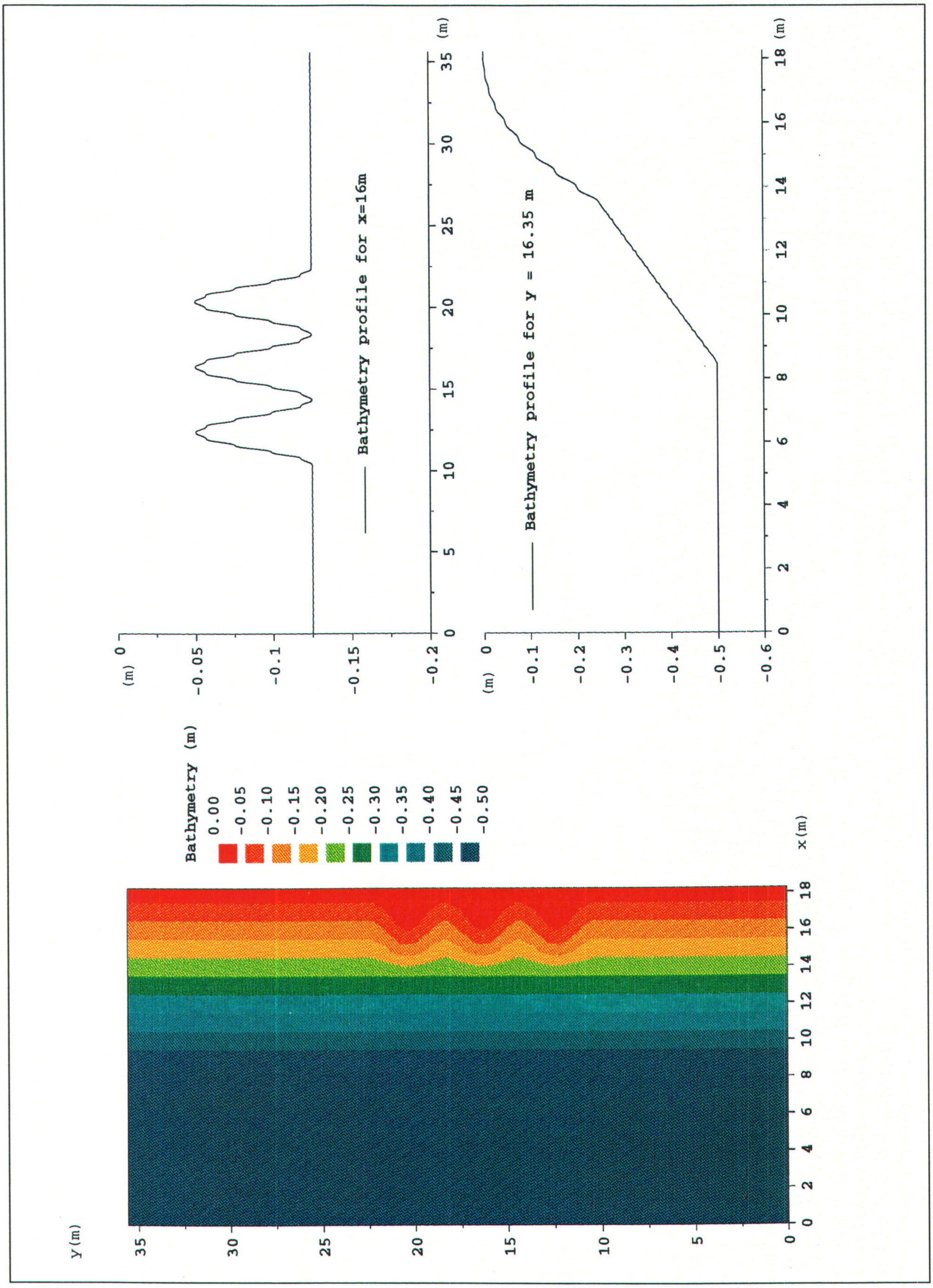

Figure 3.1 Bathymetry around the cusps

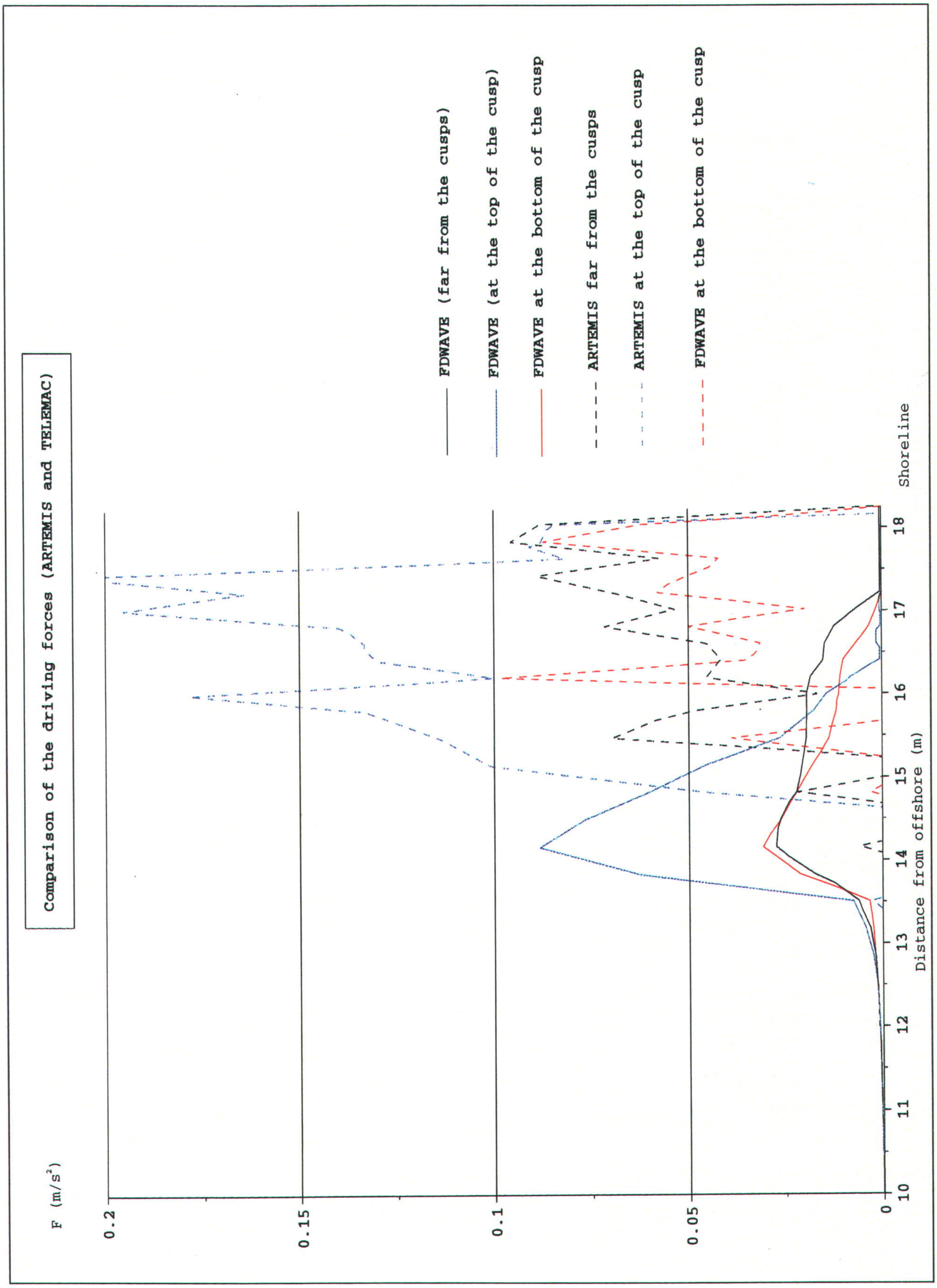

Figure 3.2 Driving forces

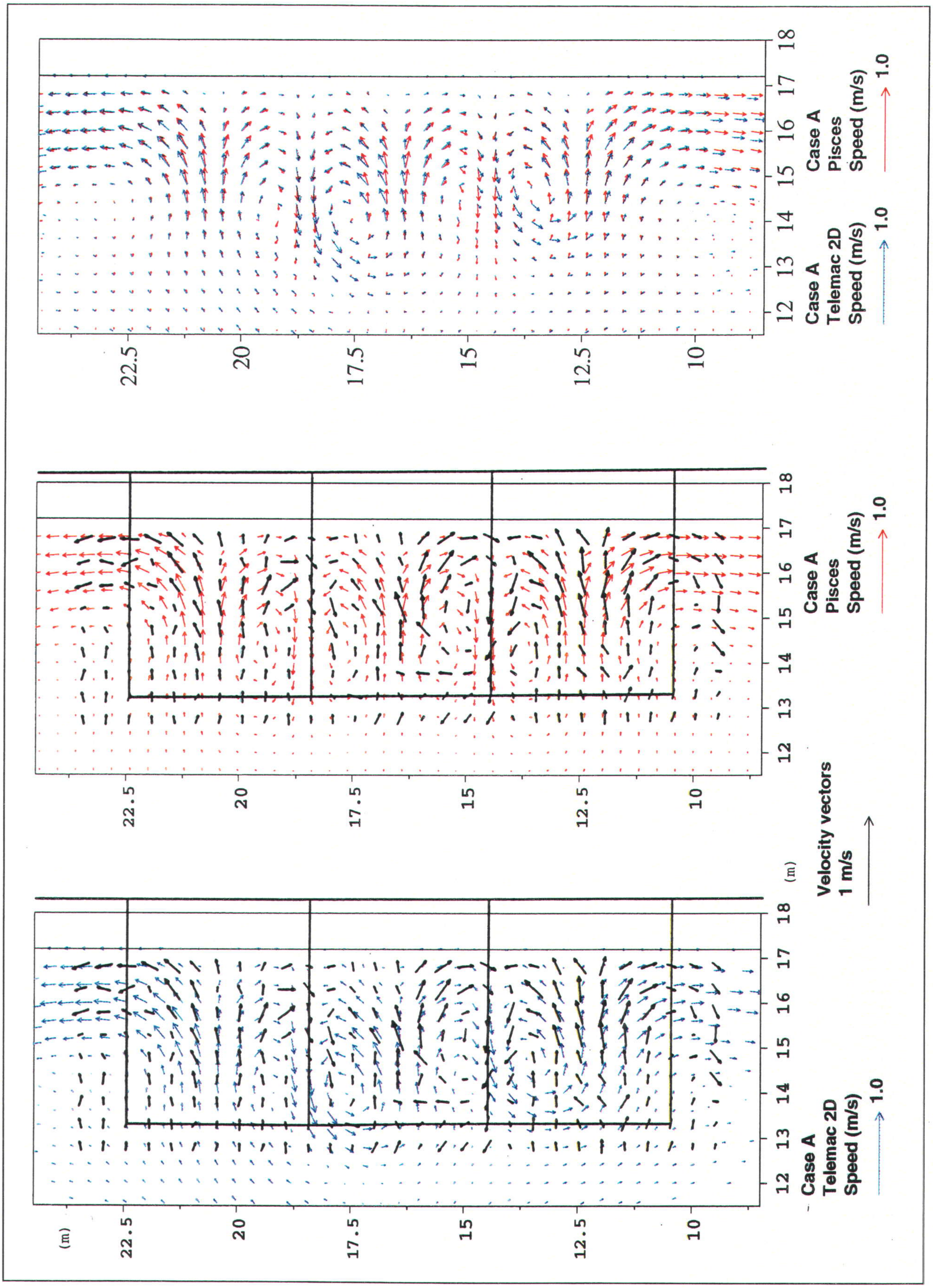

Figure 3.3 **FDWAVE/TELEMAC-PISCES for Case A**

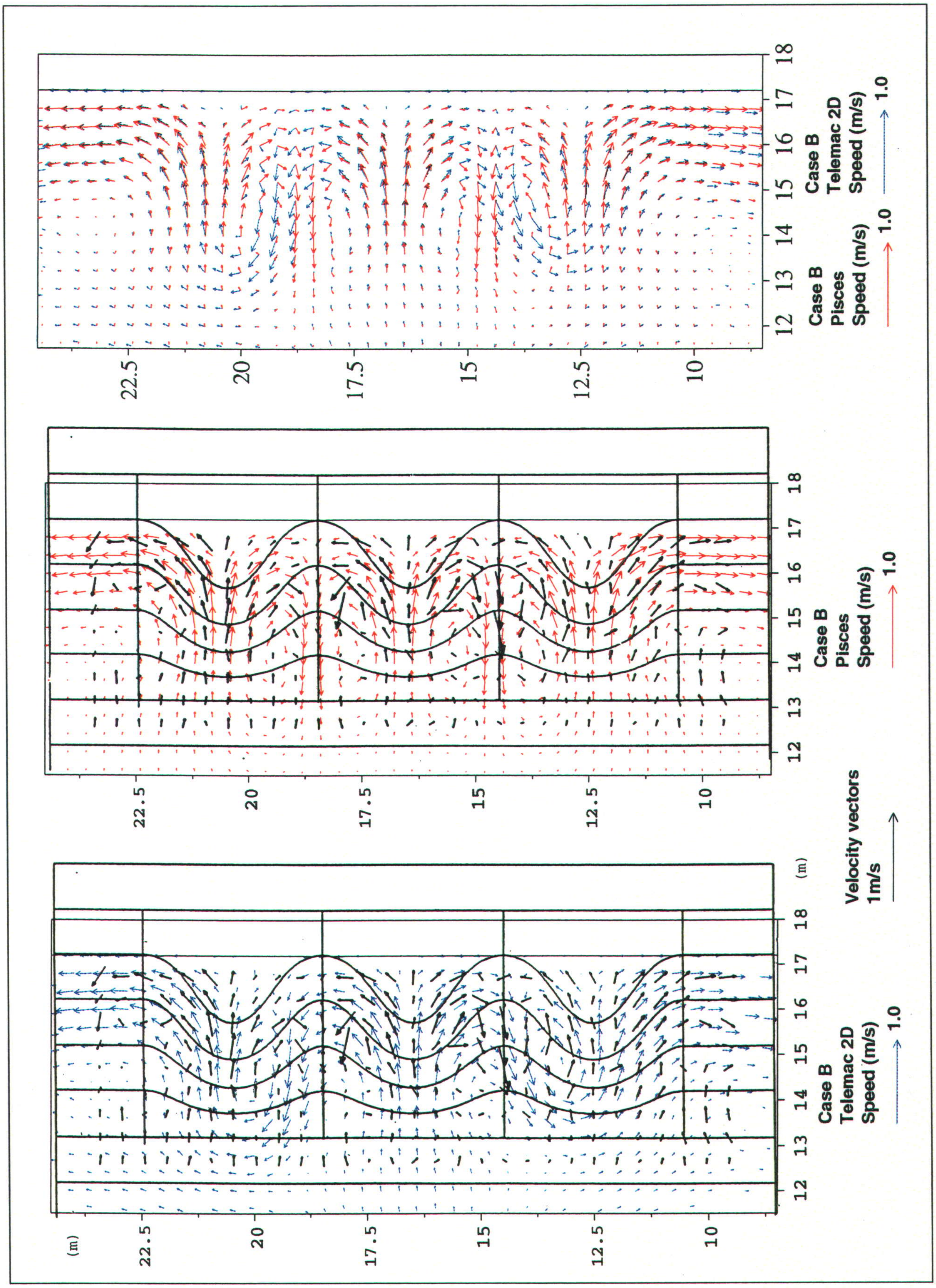

Figure 3.4 FDWAVE/TELEMAC-PISCES for Case B

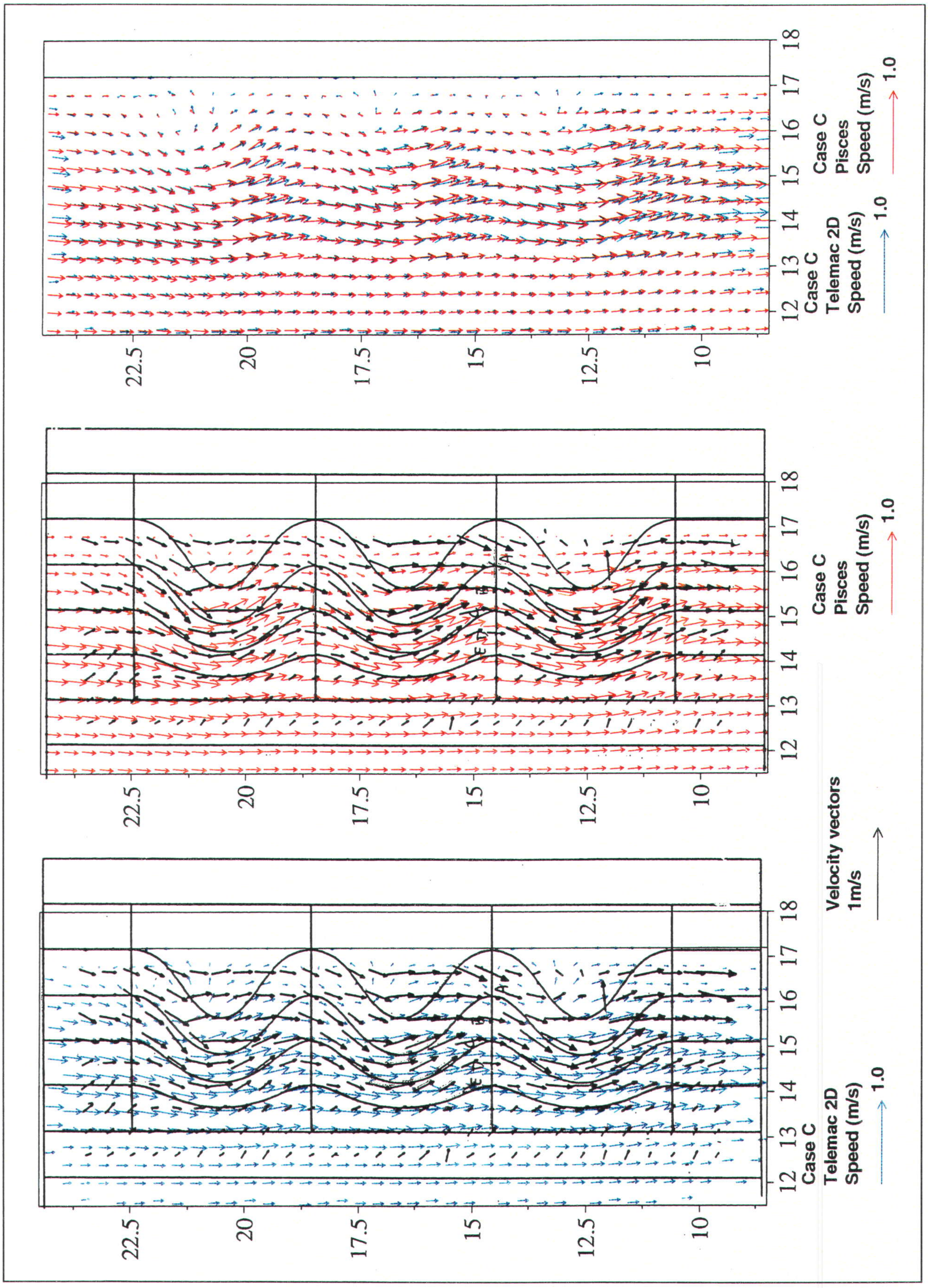

Figure 3.5 FDWAVE/TELEMAC-PISCES for Case C

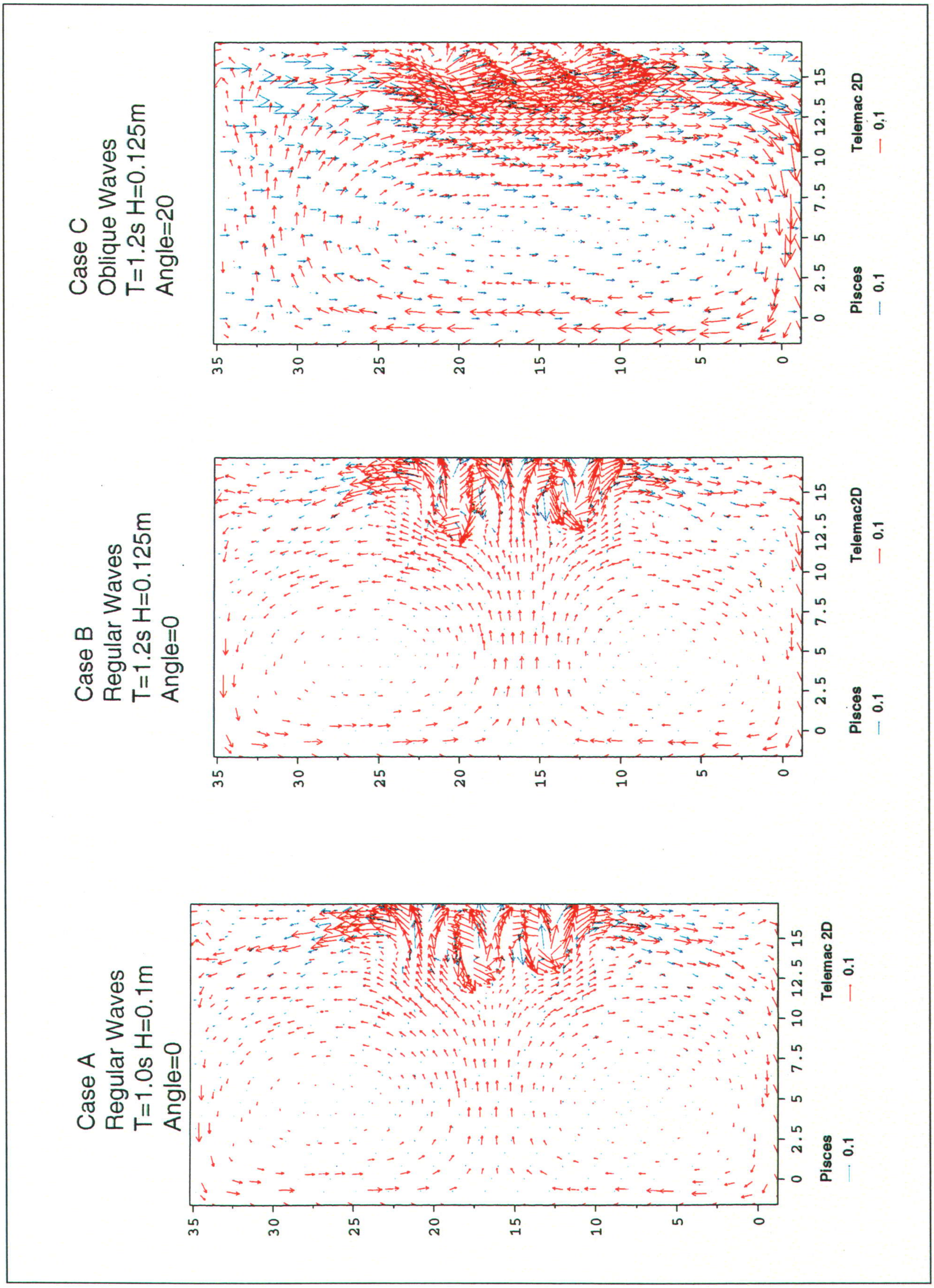

Figure 3.6 **Comparison of the three cases for the entire domain**

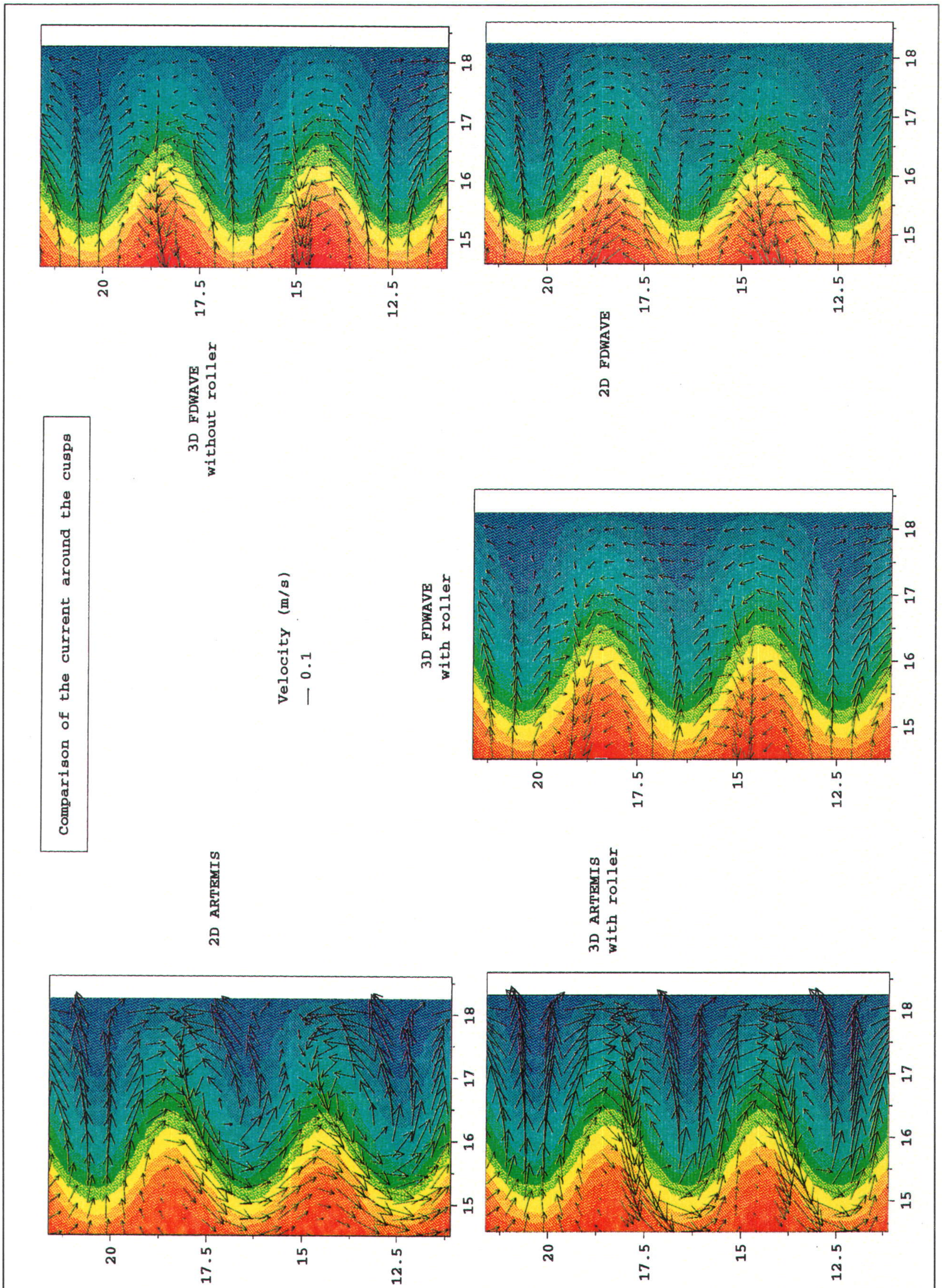

Figure 3.7 Comparison of the current around the cusps (2D and 3D)

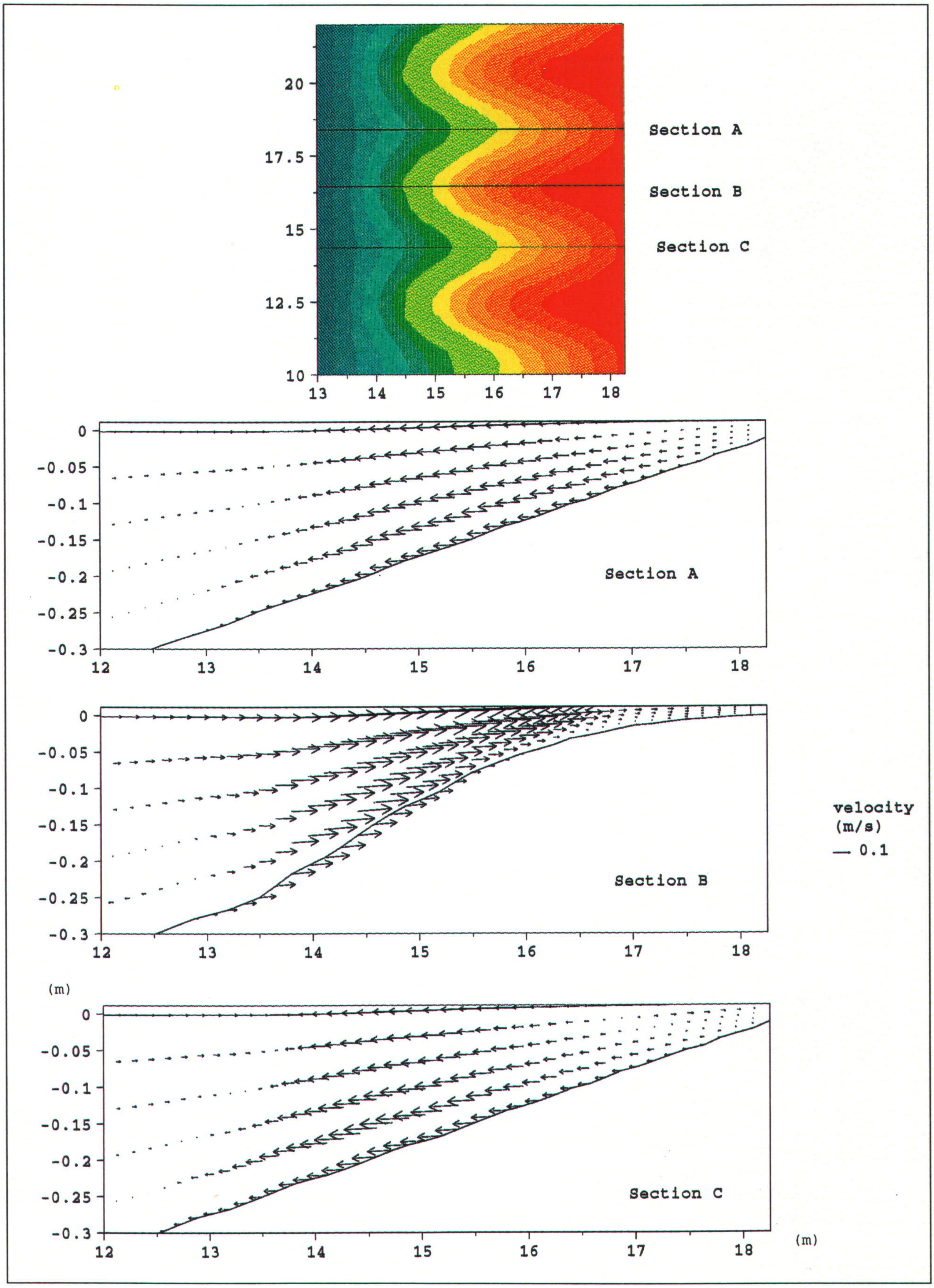

Figure 3.8 Current using the driving forces of FDWAVE with the roller (vertical profile)

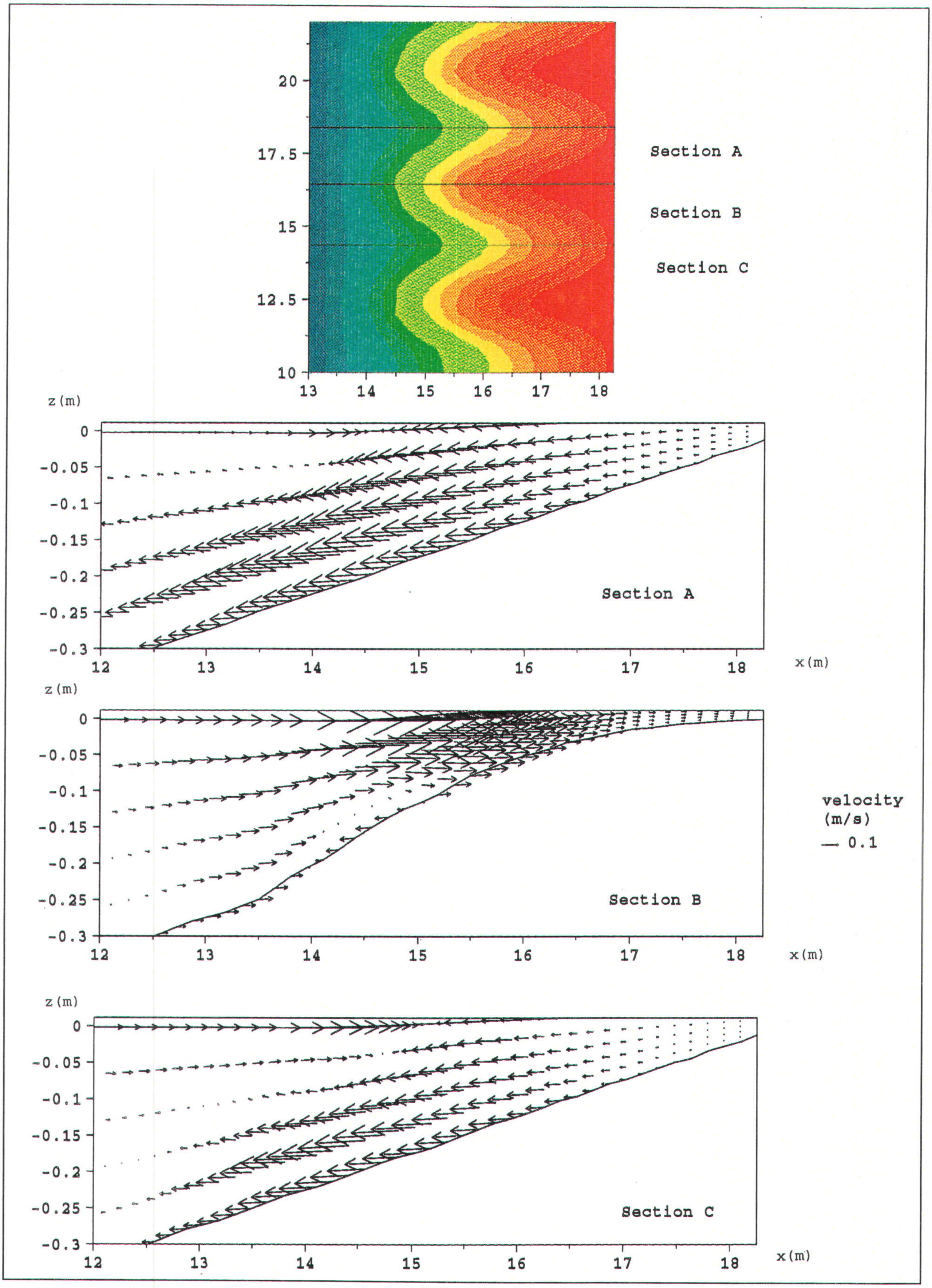

Figure 3.9 **Current using the driving forces of FDWAVE imposed at the surface (vertical profile)**

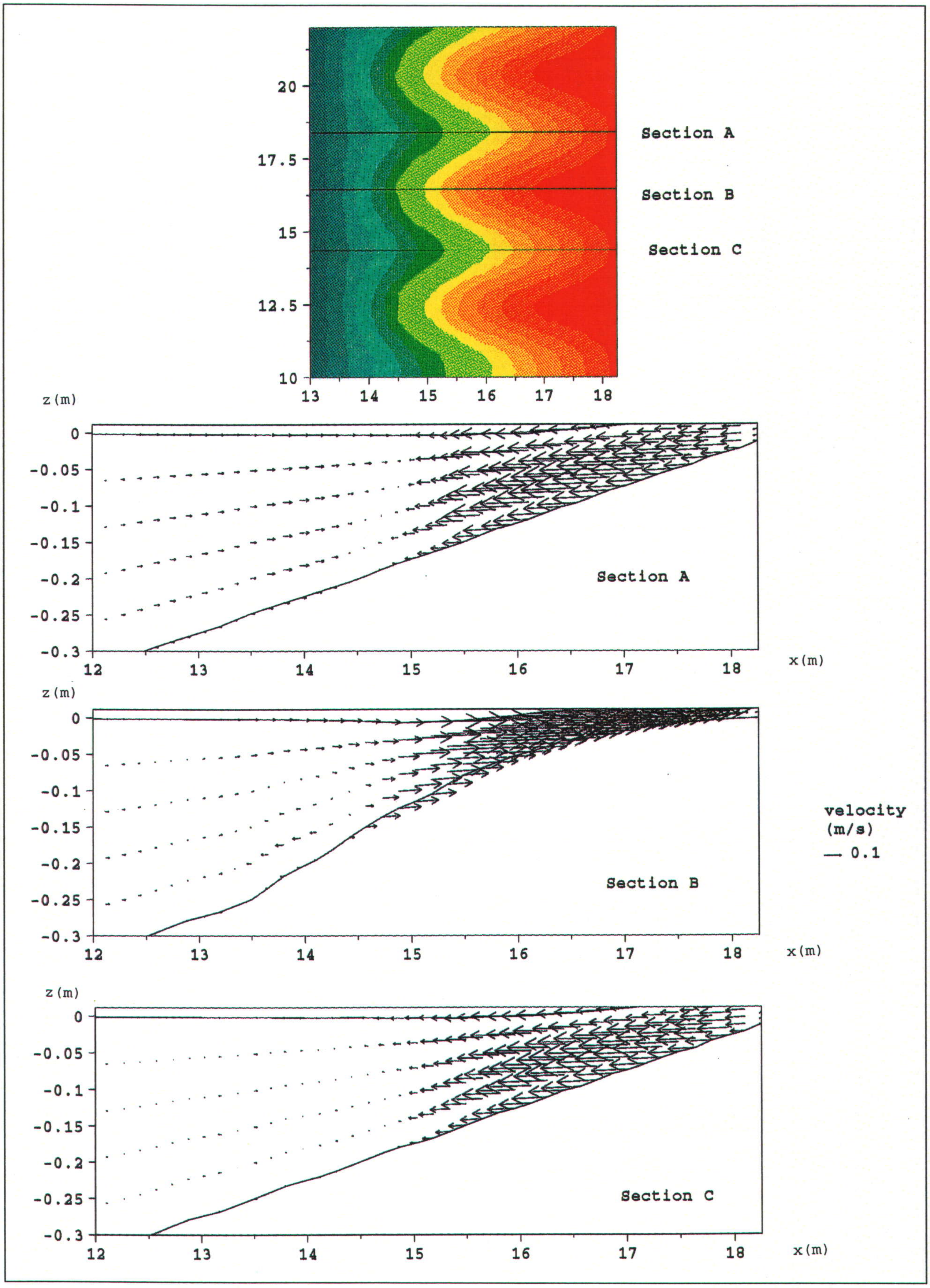

Figure 3.10 **Current using the driving forces of ARTEMIS with the roller (vertical profile)**

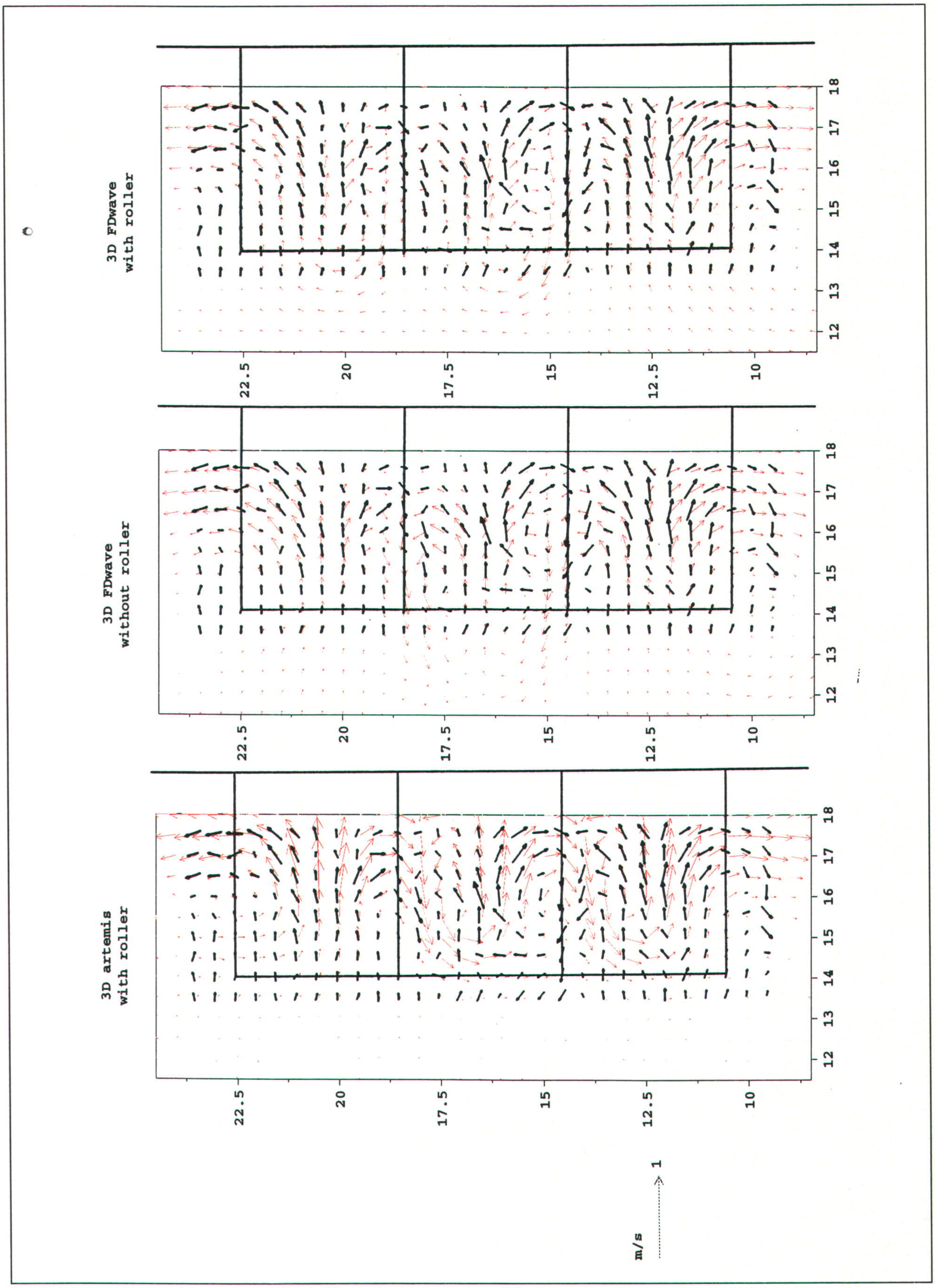

Figure 3.11 Depth integrated current for the 3D models

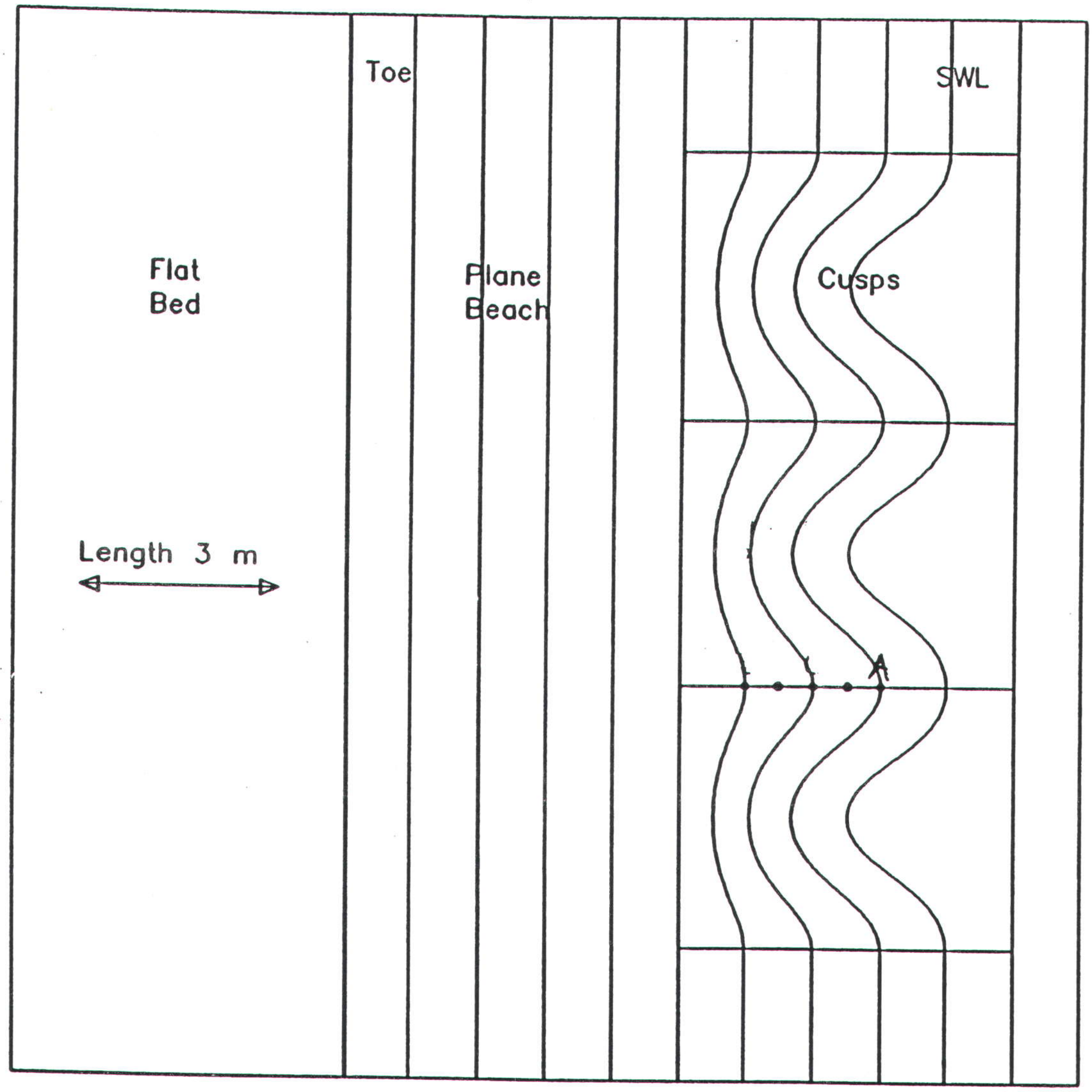

Close-up of ADV locations: detailed measurements of vertical profile

Figure 3.12 **Description of the measurement point A**

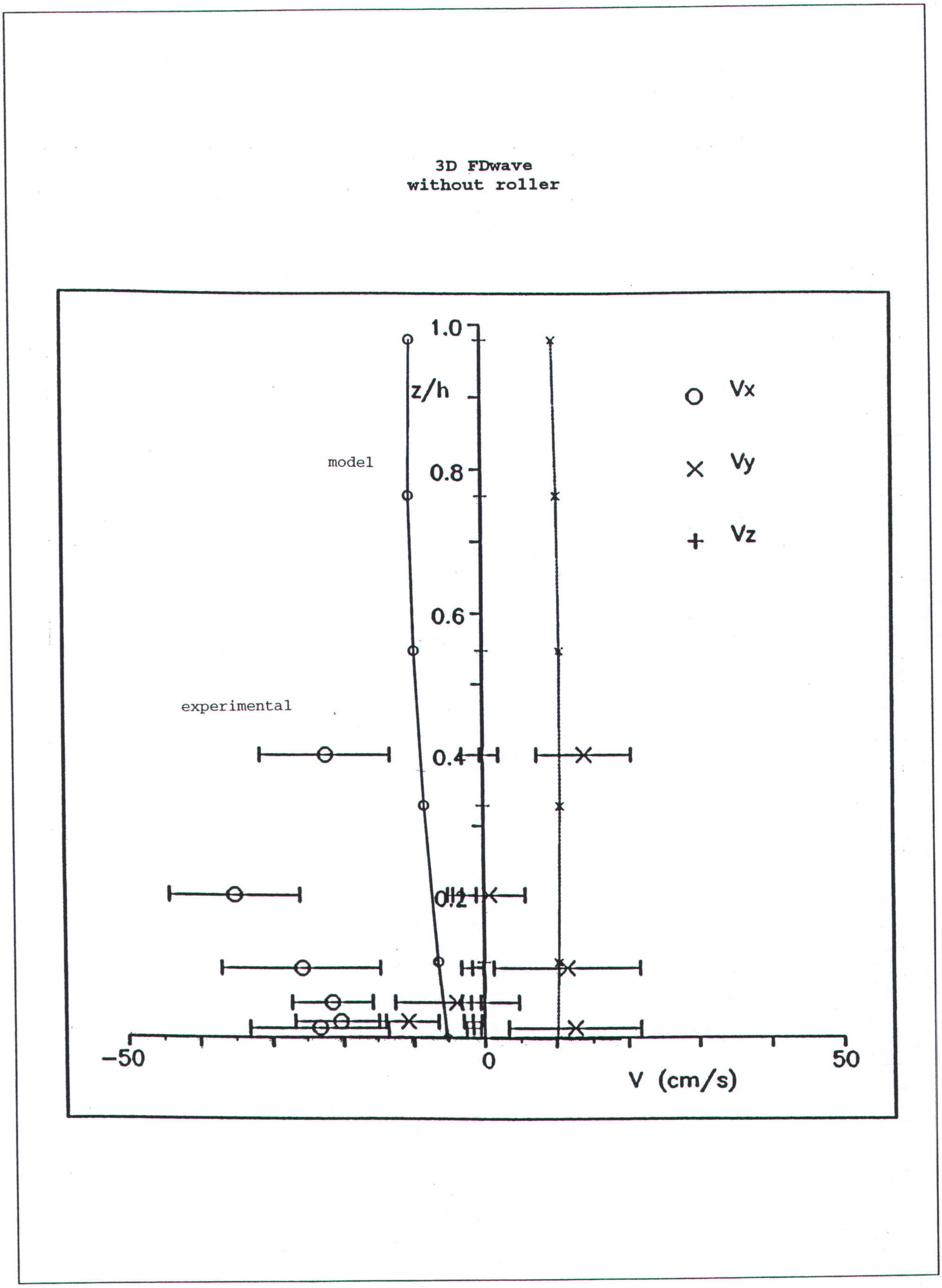

Figure 3.13 Vertical profile at A. Driving forces from FDWAVE at the surface

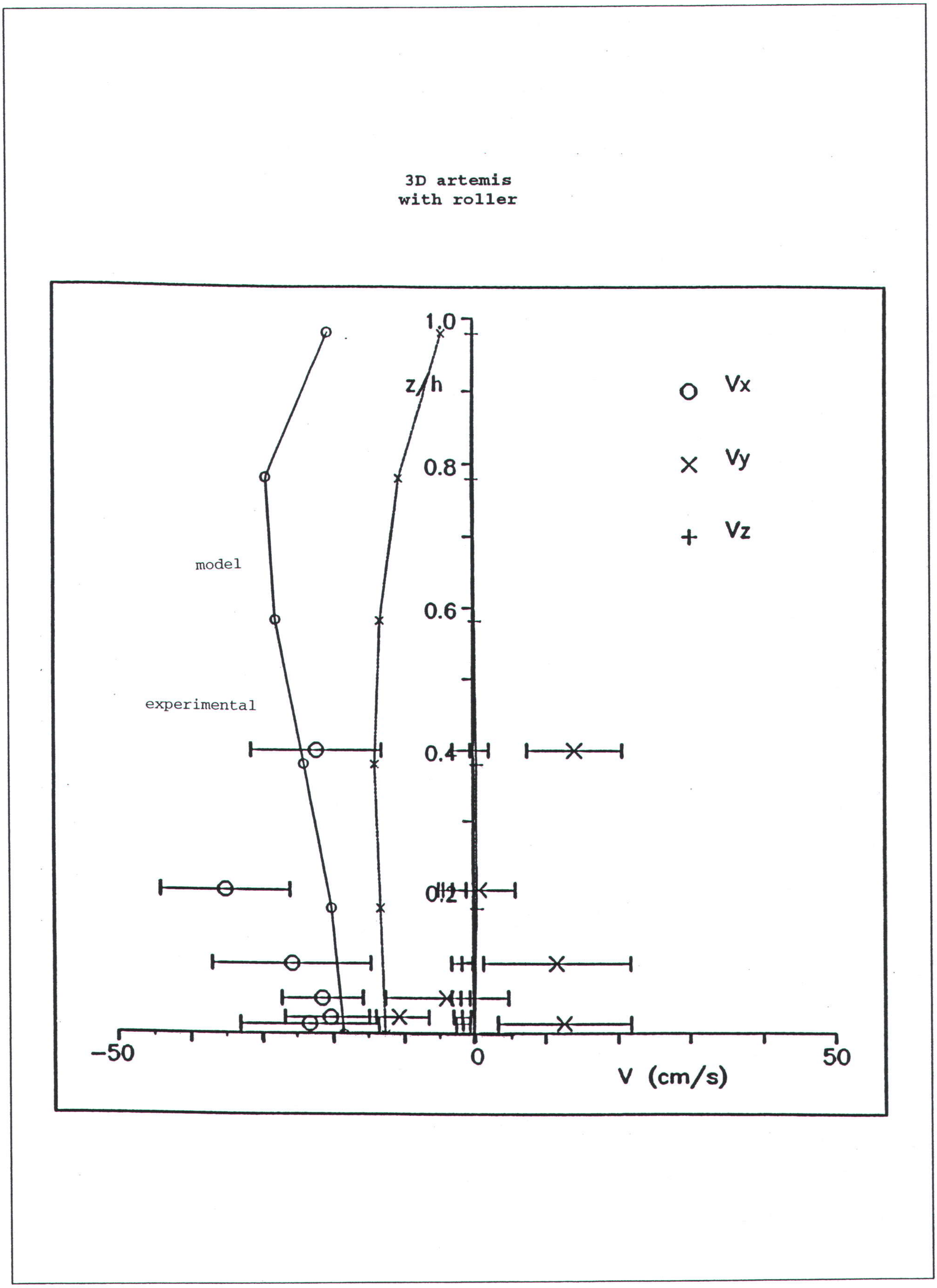

Figure 3.14 Vertical profile at A. Driving forces from ARTEMIS with the roller

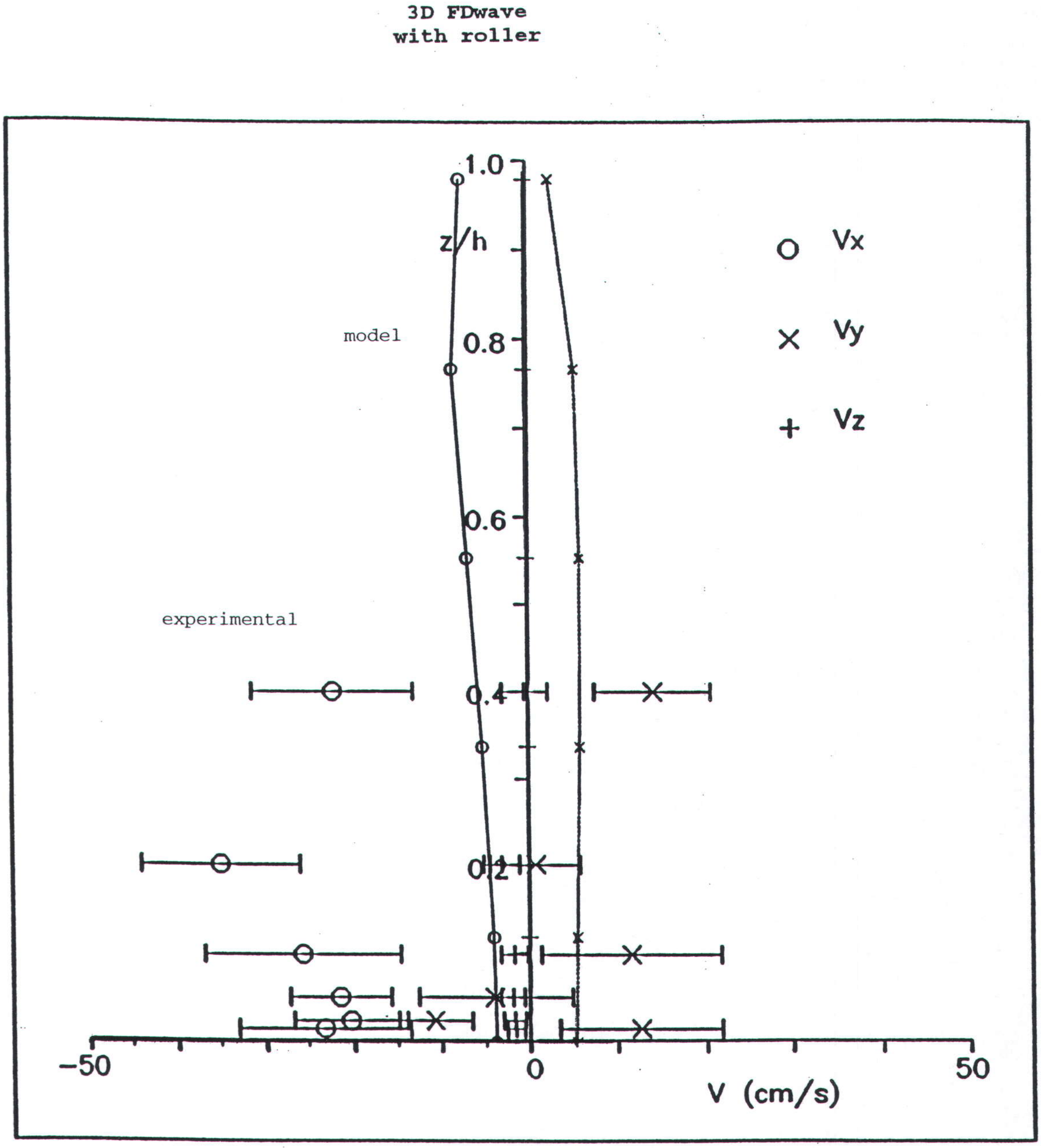

Figure 3.15 Vertical profile at A. Driving forces from FDWAVE with the roller

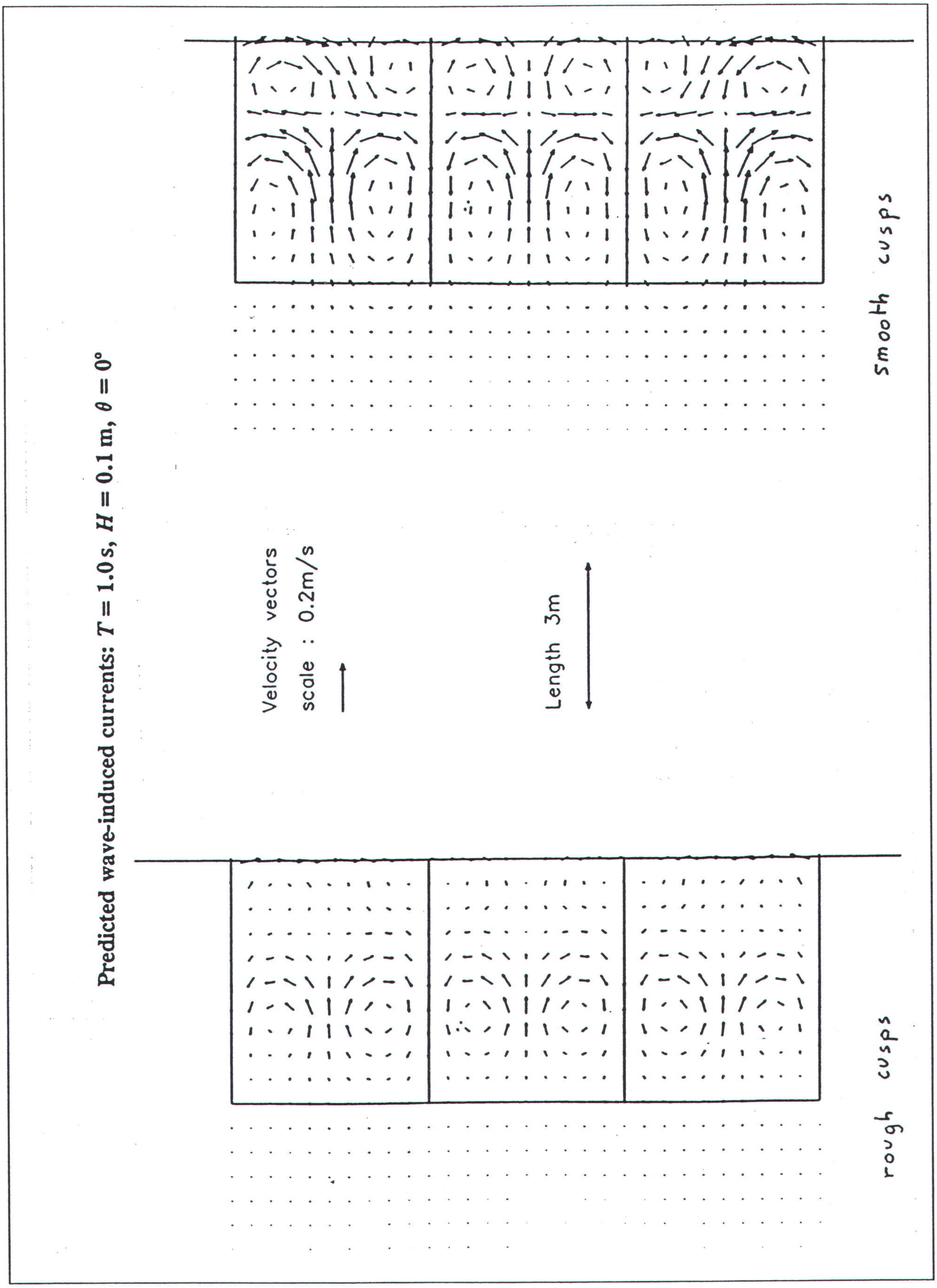

Figure 3.16 **Secondary recirculation current behind the cusps**

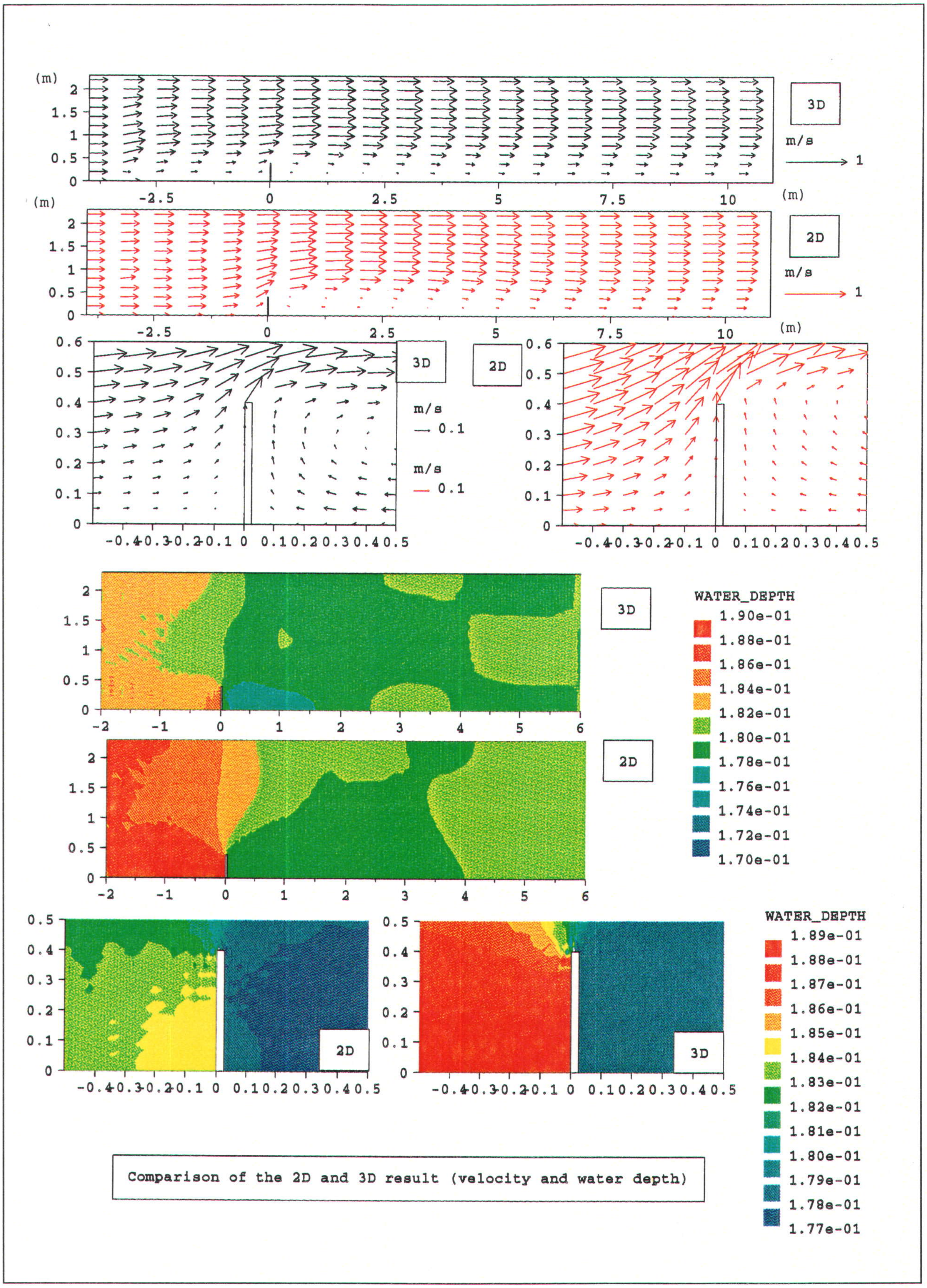

Figure 4.1 Comparison of the 2D and the 3D results

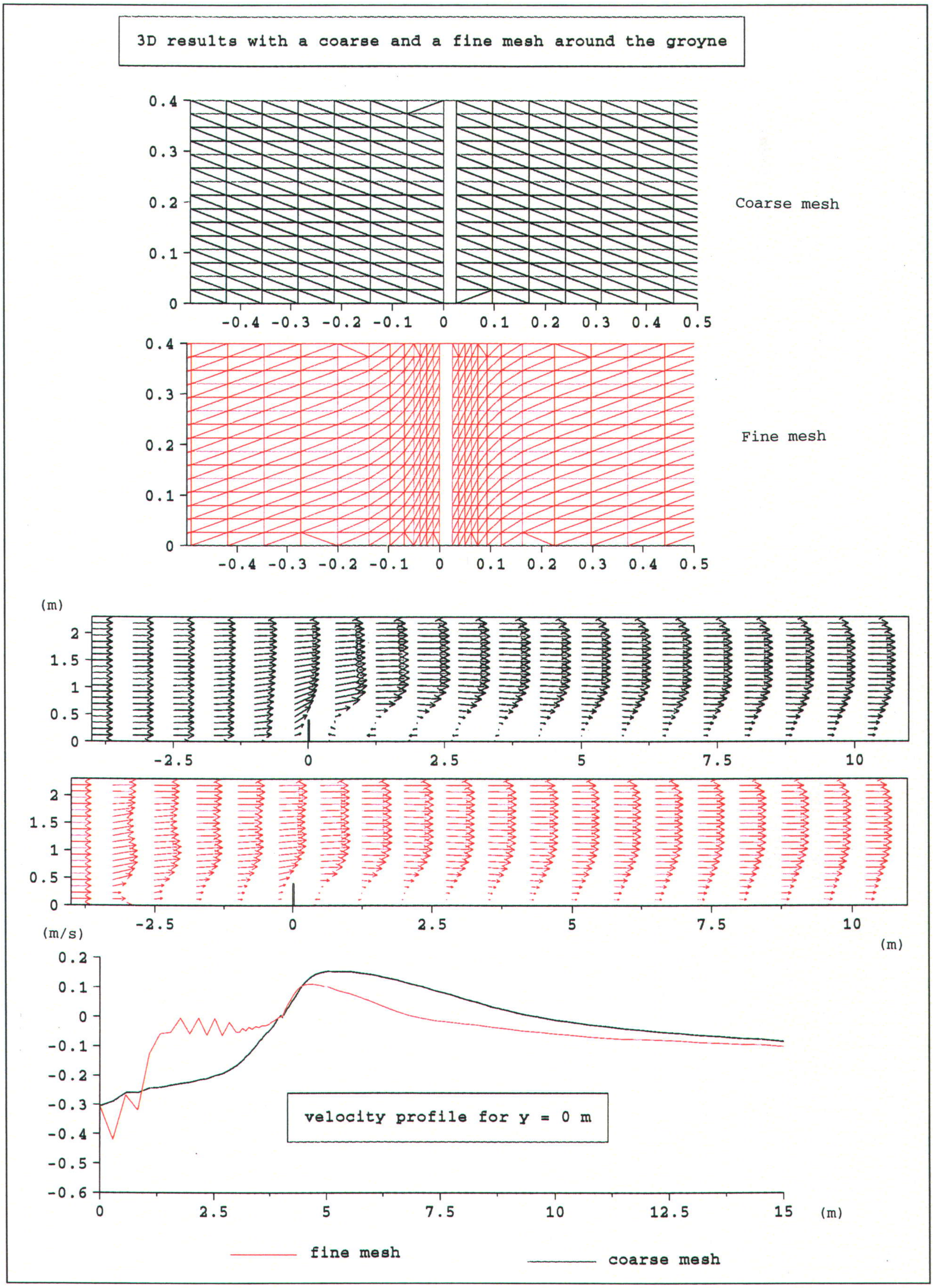

Figure 4.2 Comparison of the currents using different meshes

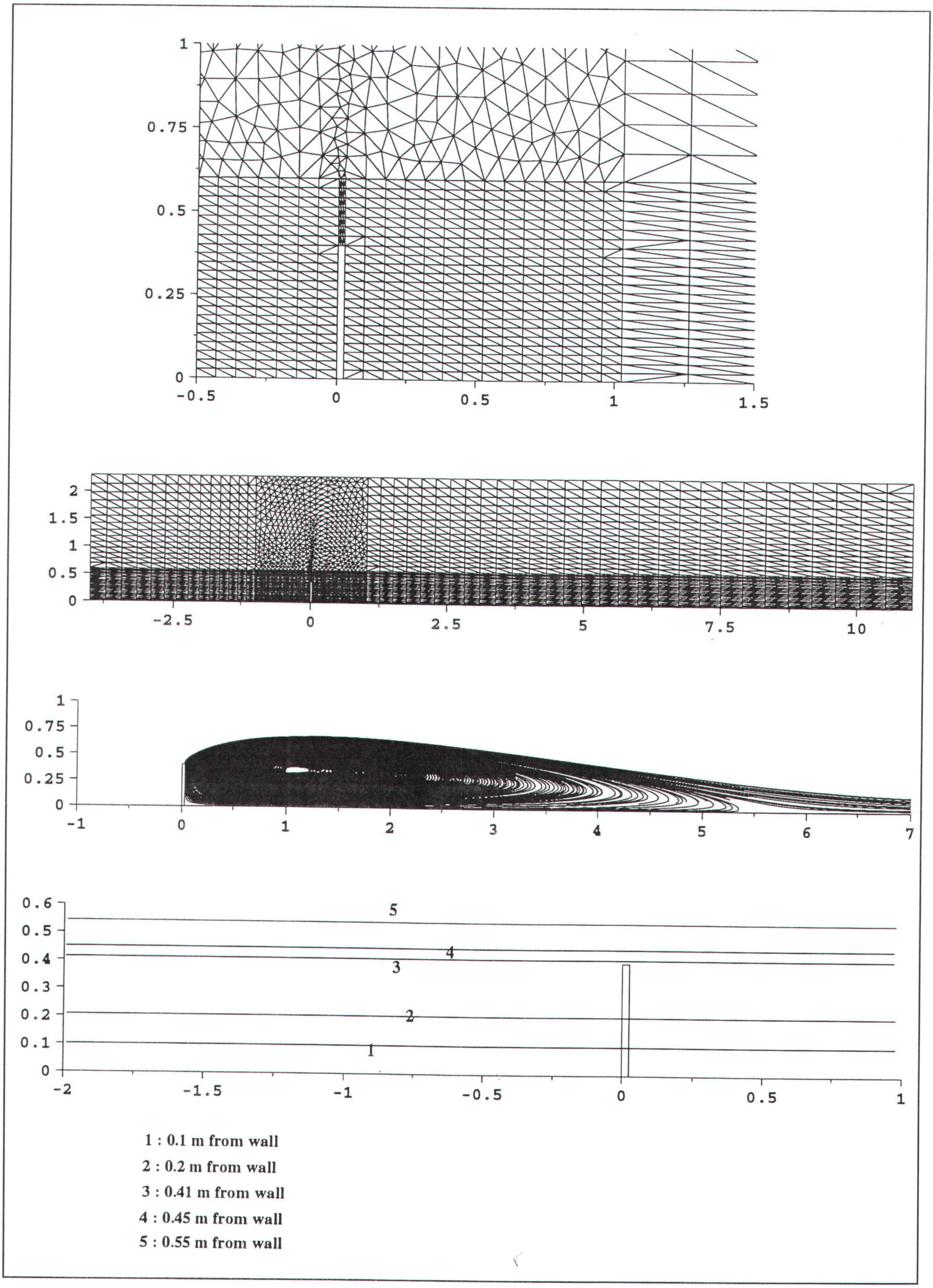

Figure 4.3 Description of the mesh and of the cross-section profiles

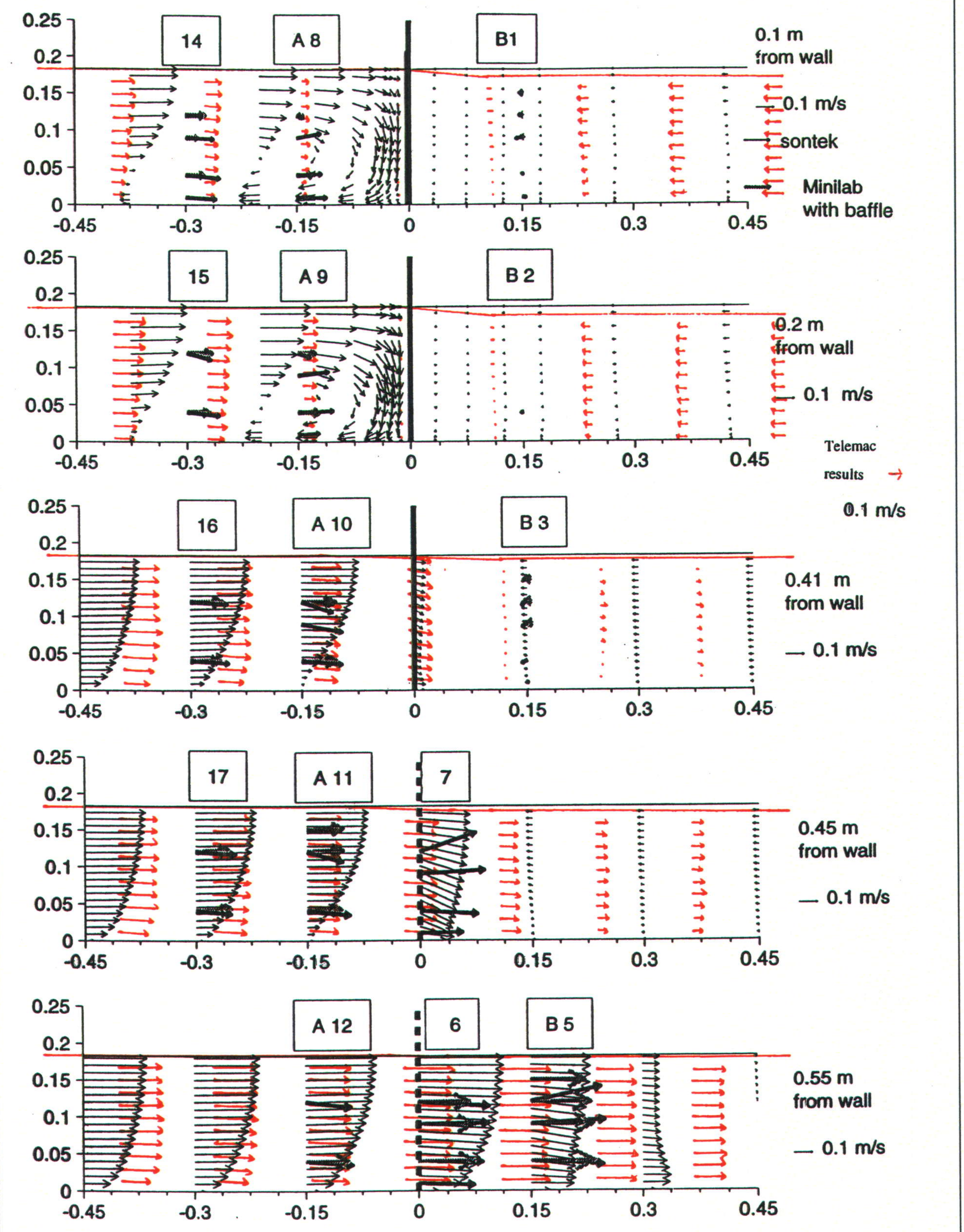

Figure 4.4 Velocity for several cross-sections

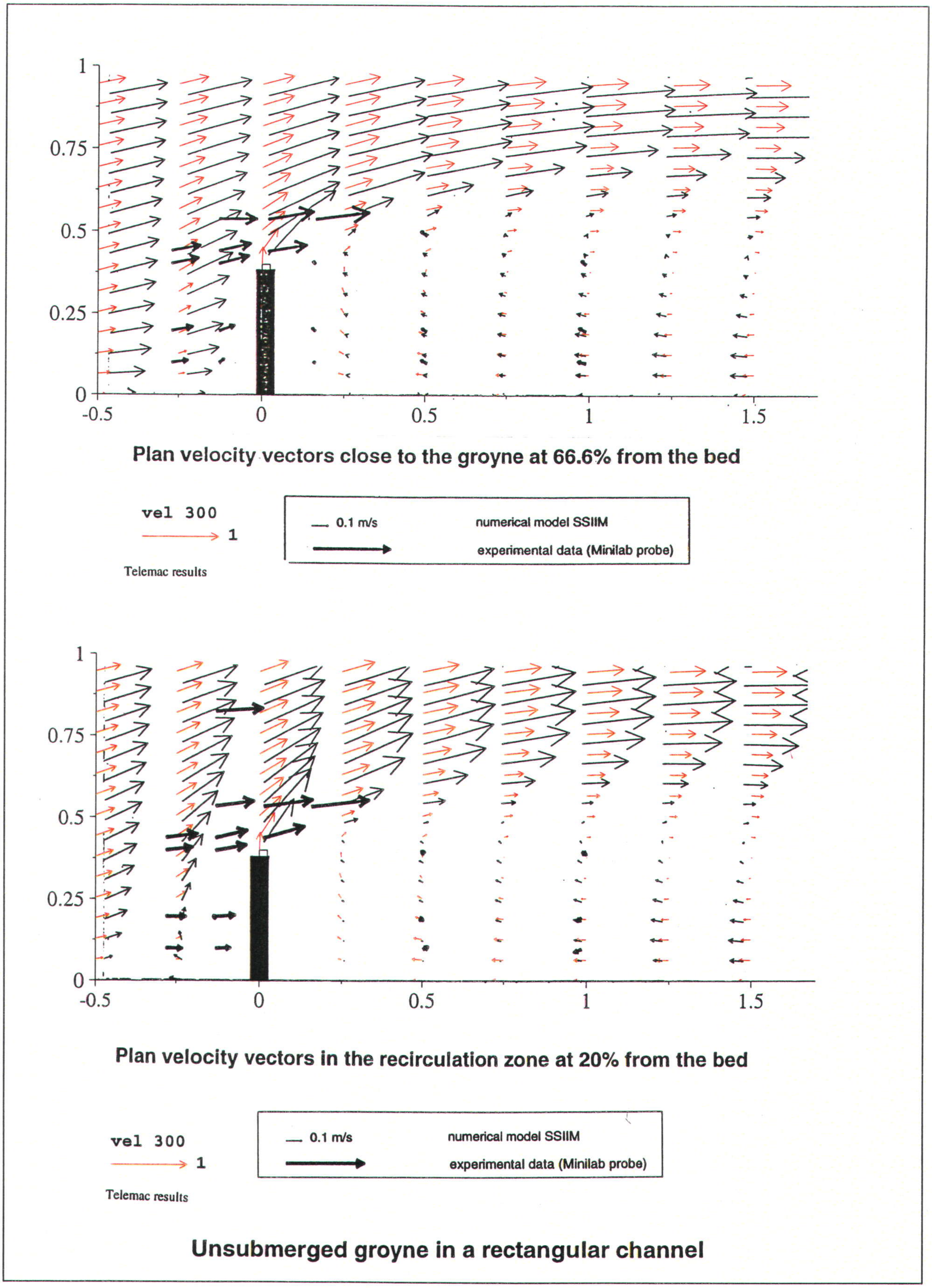

Figure 4.5 Currents for two layers (66.6% and 20 % from the bed)

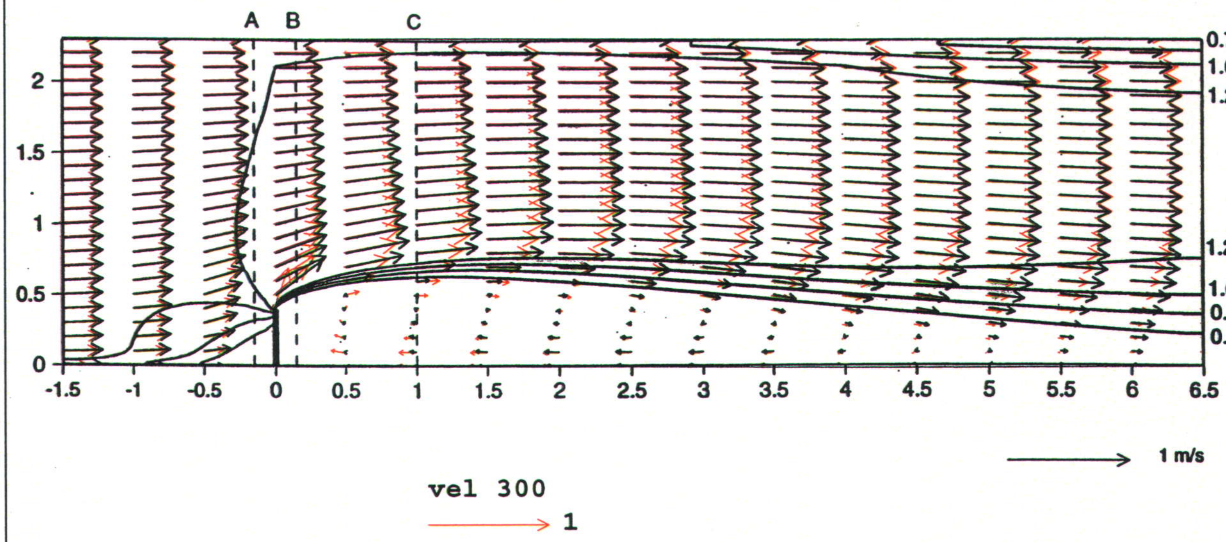

Velocitiy vectors and normalised velocity contours at mid-depth

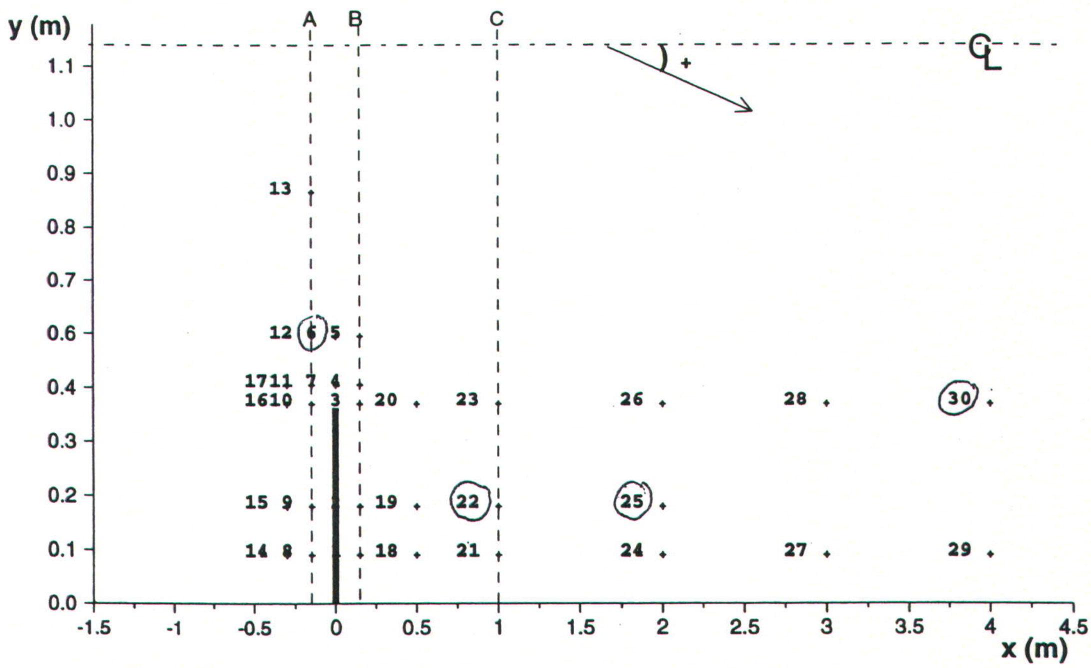

Experimental points and sections

Figure 4.6 **Current at mid-depth and description of the measurements points**

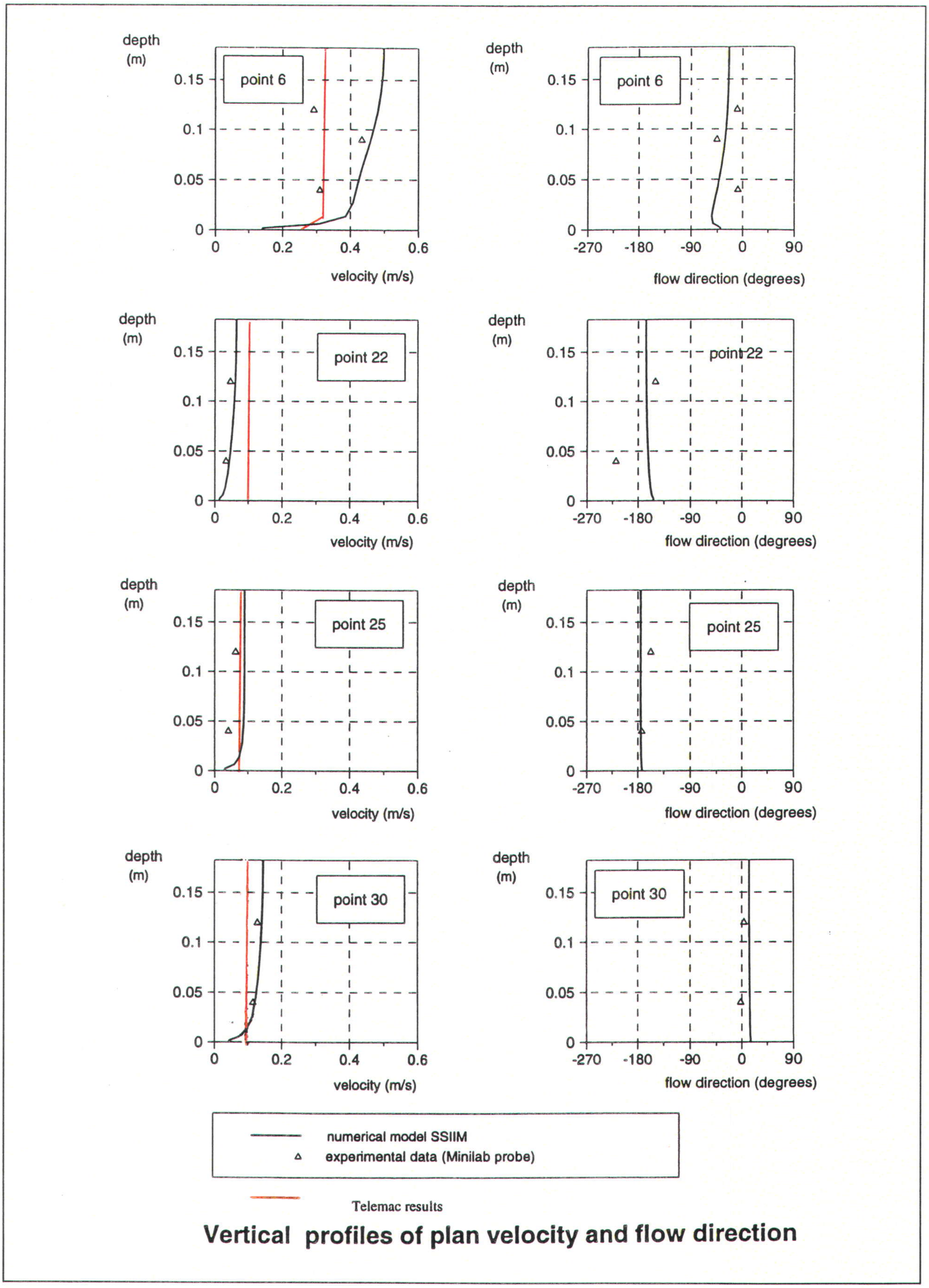

Figure 4.7 Velocity along the vertical for the measurements points

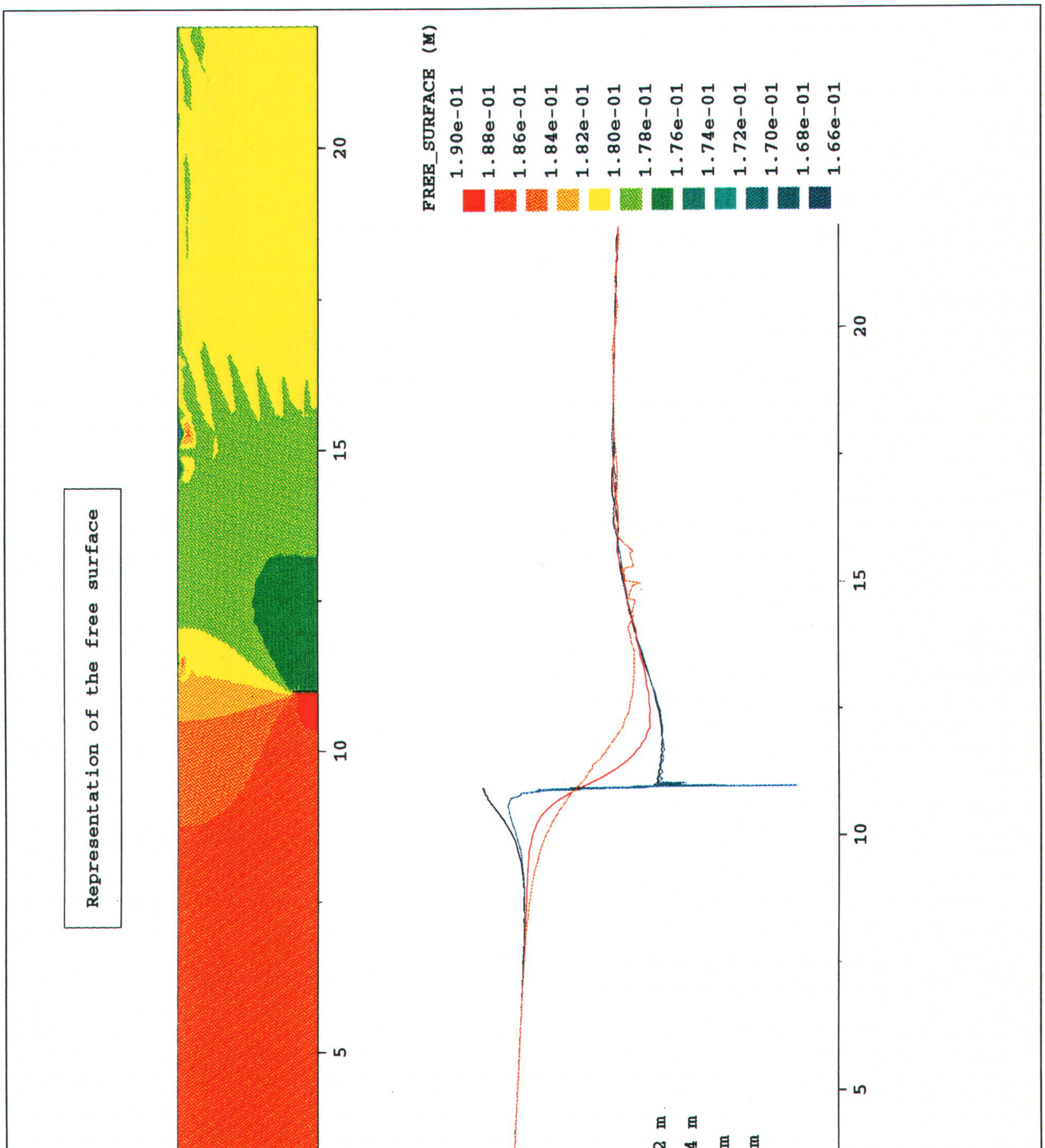

Figure 4.8 **Free surface for the Thompson boundary case**

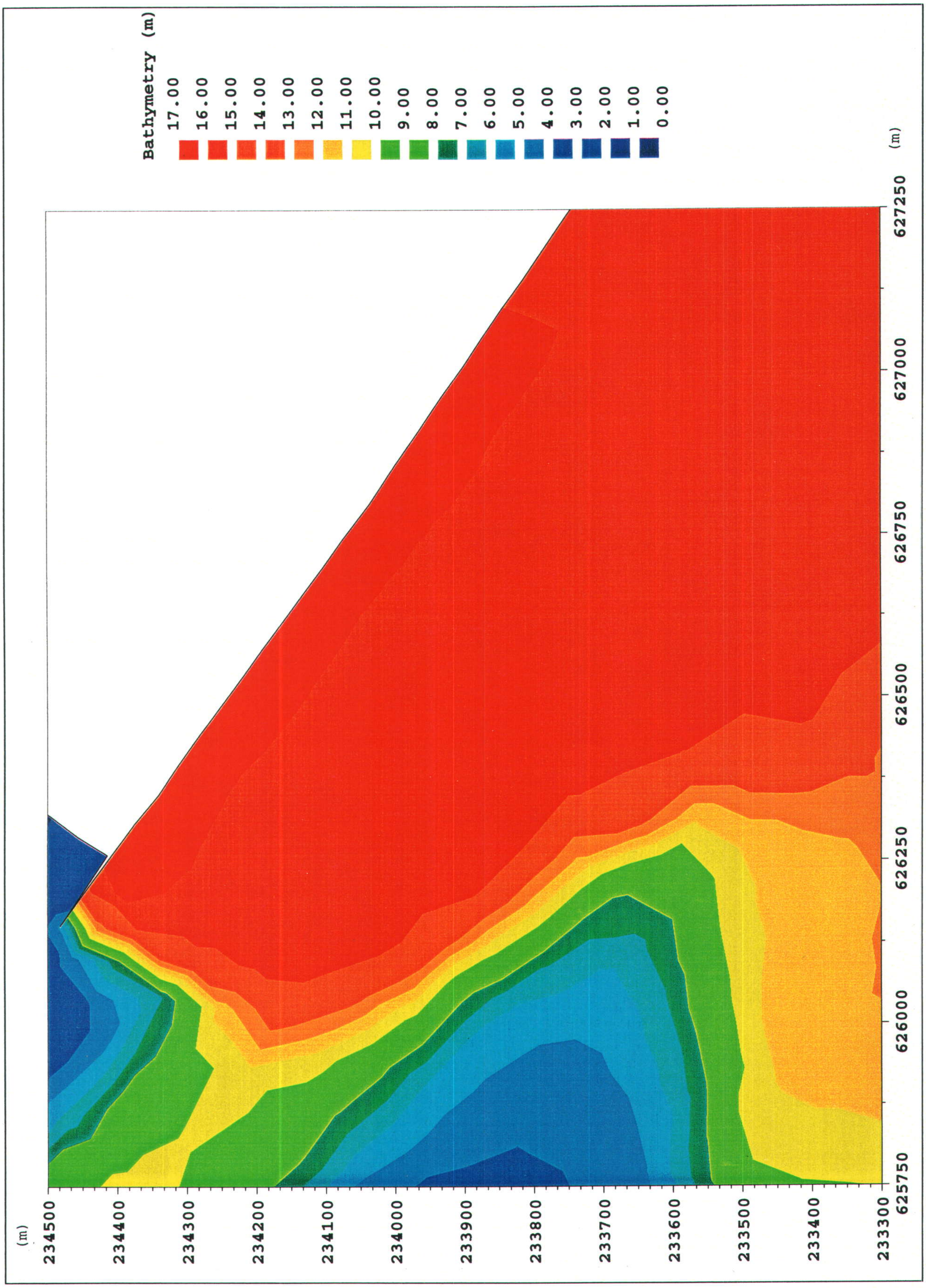

Figure 5.1 Bathymetry in front of the Trinity quay

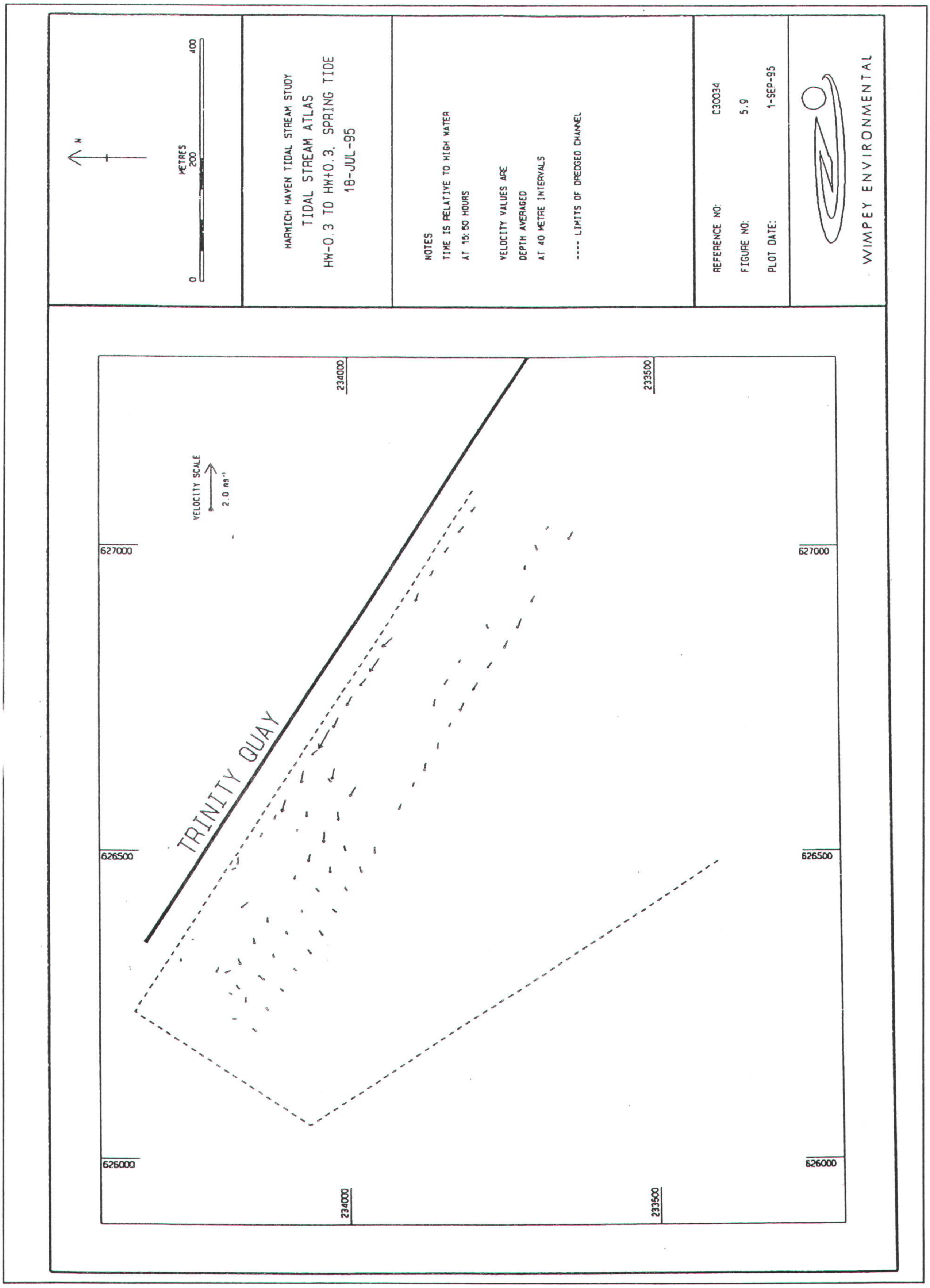

Figure 5.2 Depth averaged current (HWL-0.3,HWL+0.3)

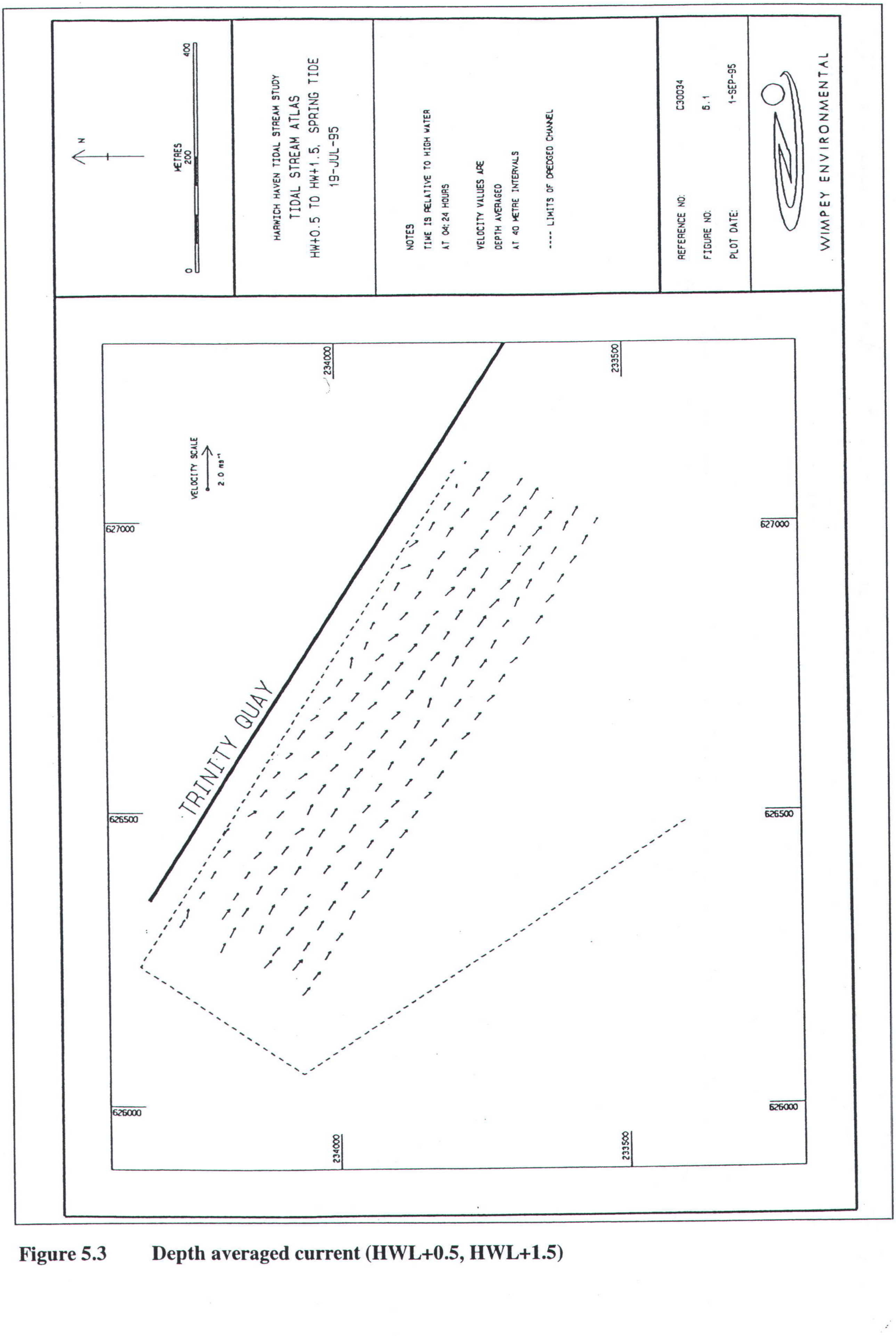

Figure 5.3 Depth averaged current (HWL+0.5, HWL+1.5)

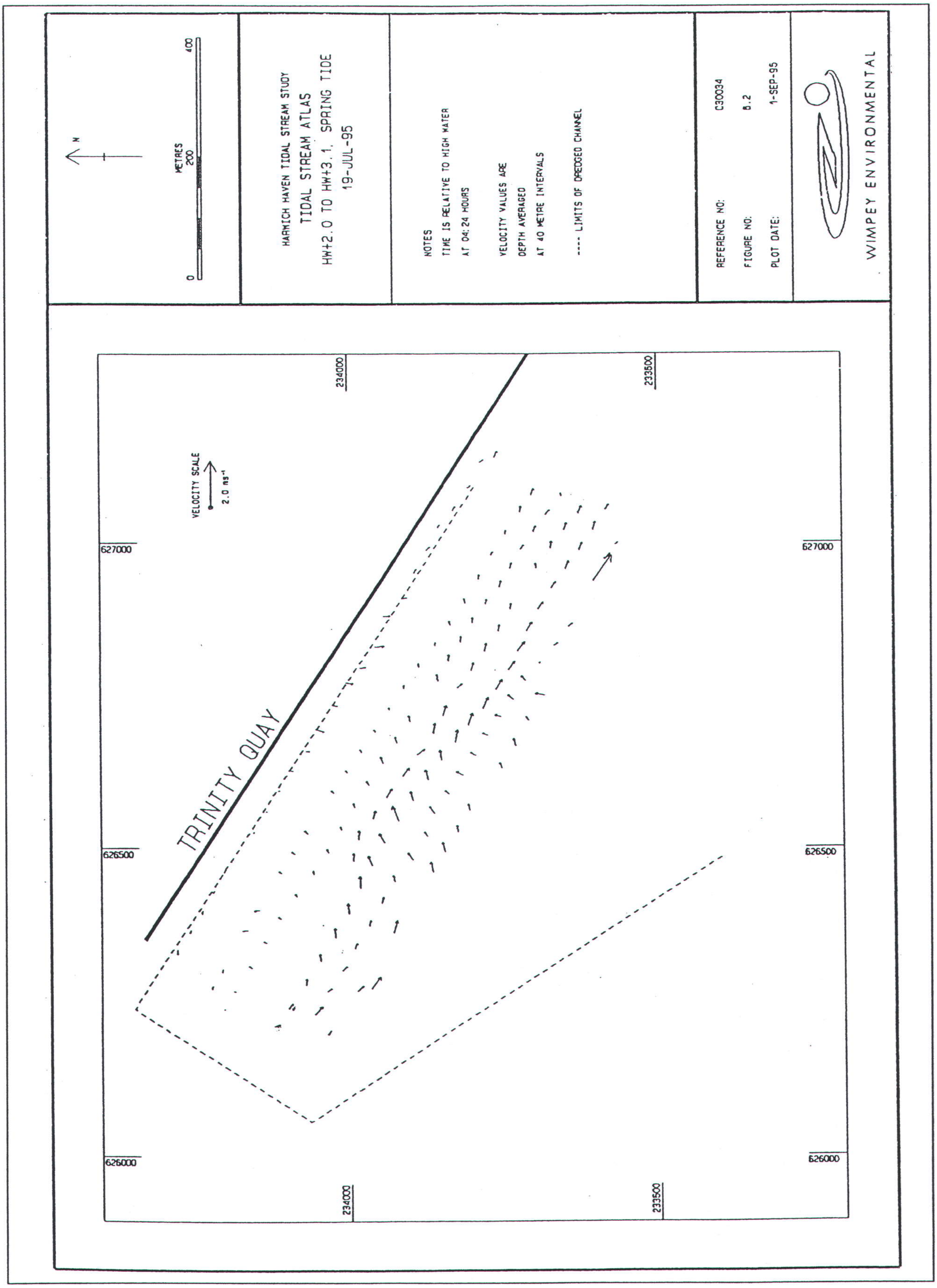

Figure 5.4 Depth averaged current (HWL+2.0, HWL+3.1)

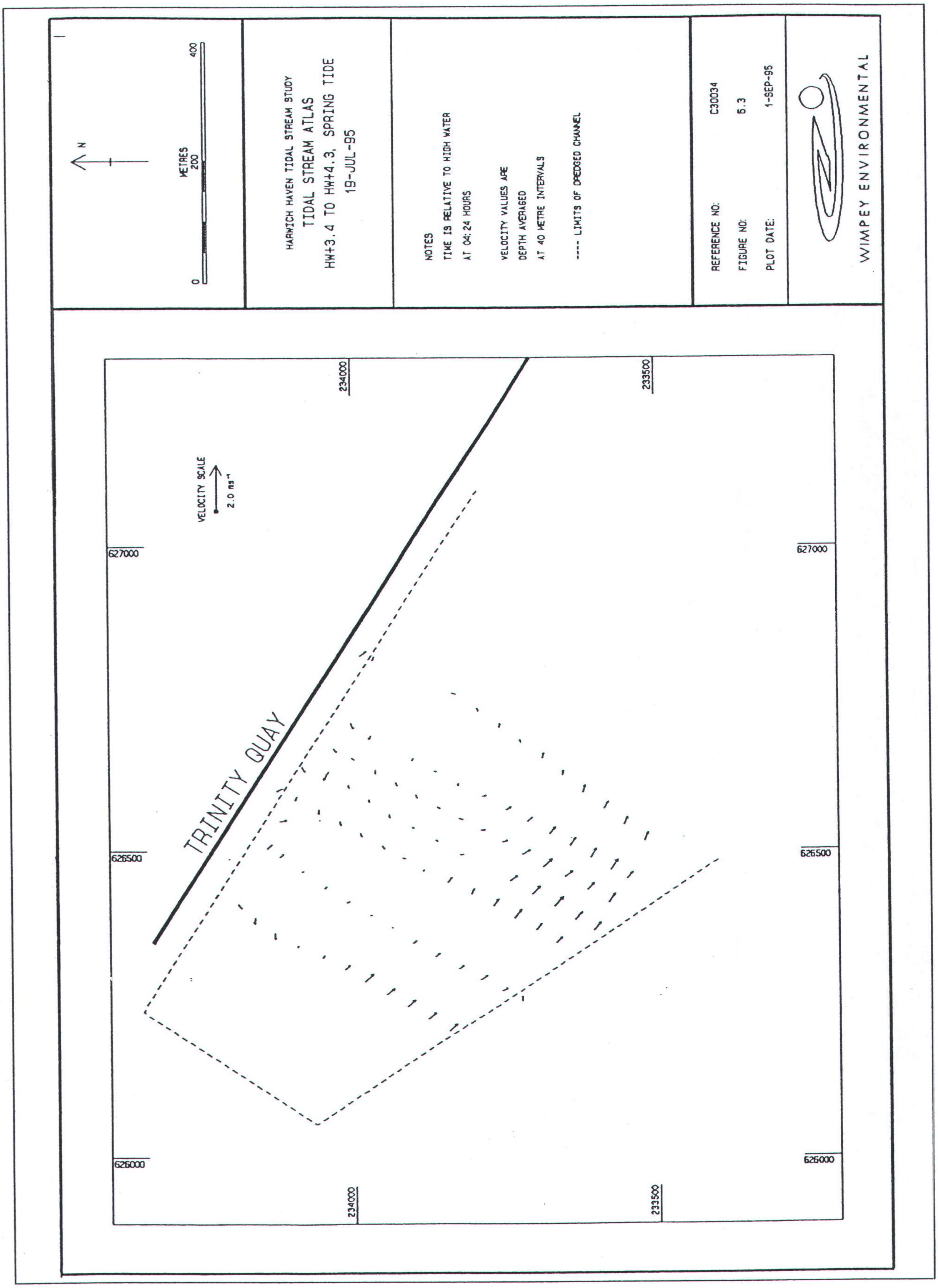

Figure 5.5 Depth averaged current (HWL+3.4, HWL+4.3)

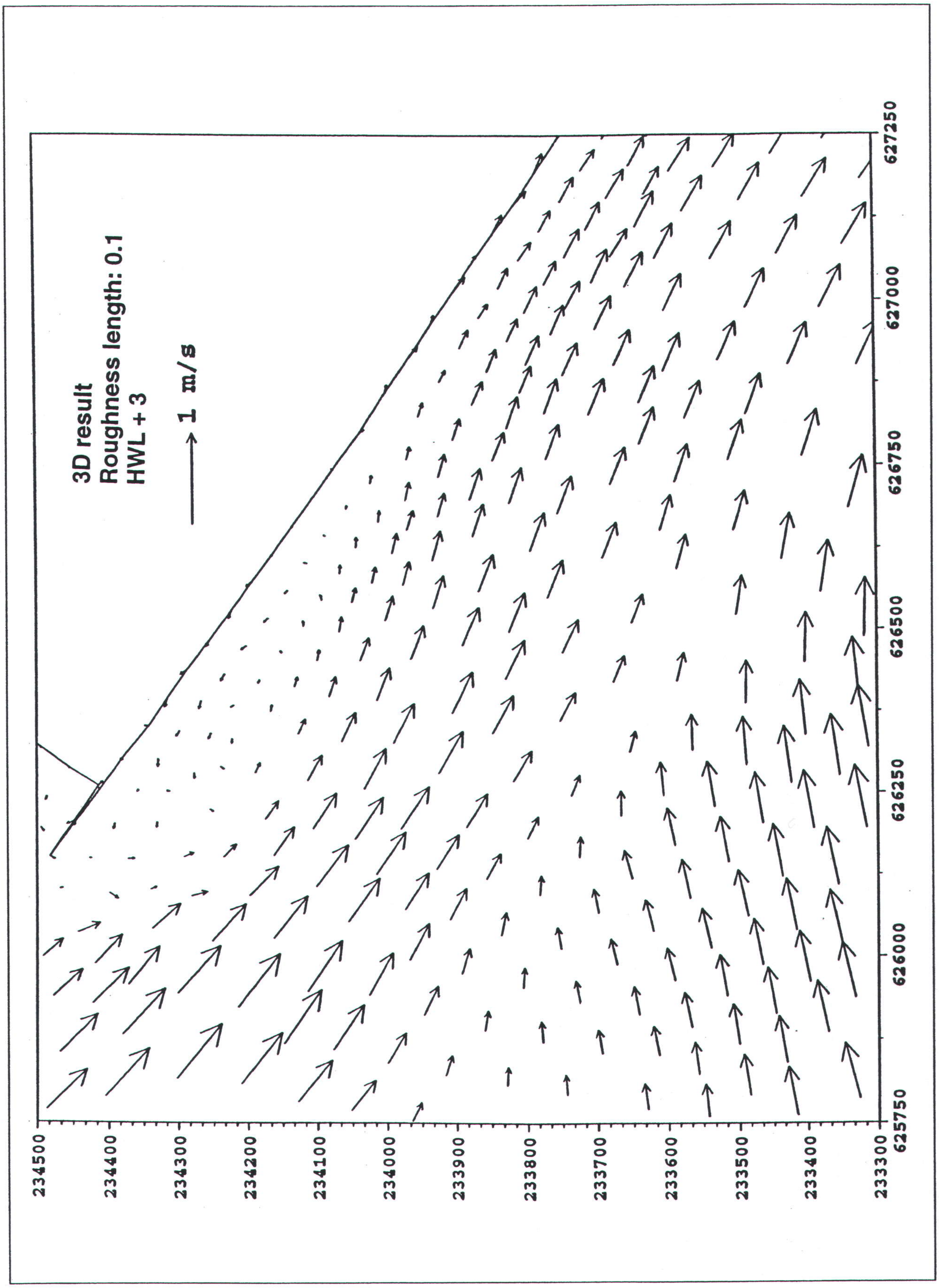

Figure 5.6 **3D model. Roughness length=0.1 (HWL+3)**

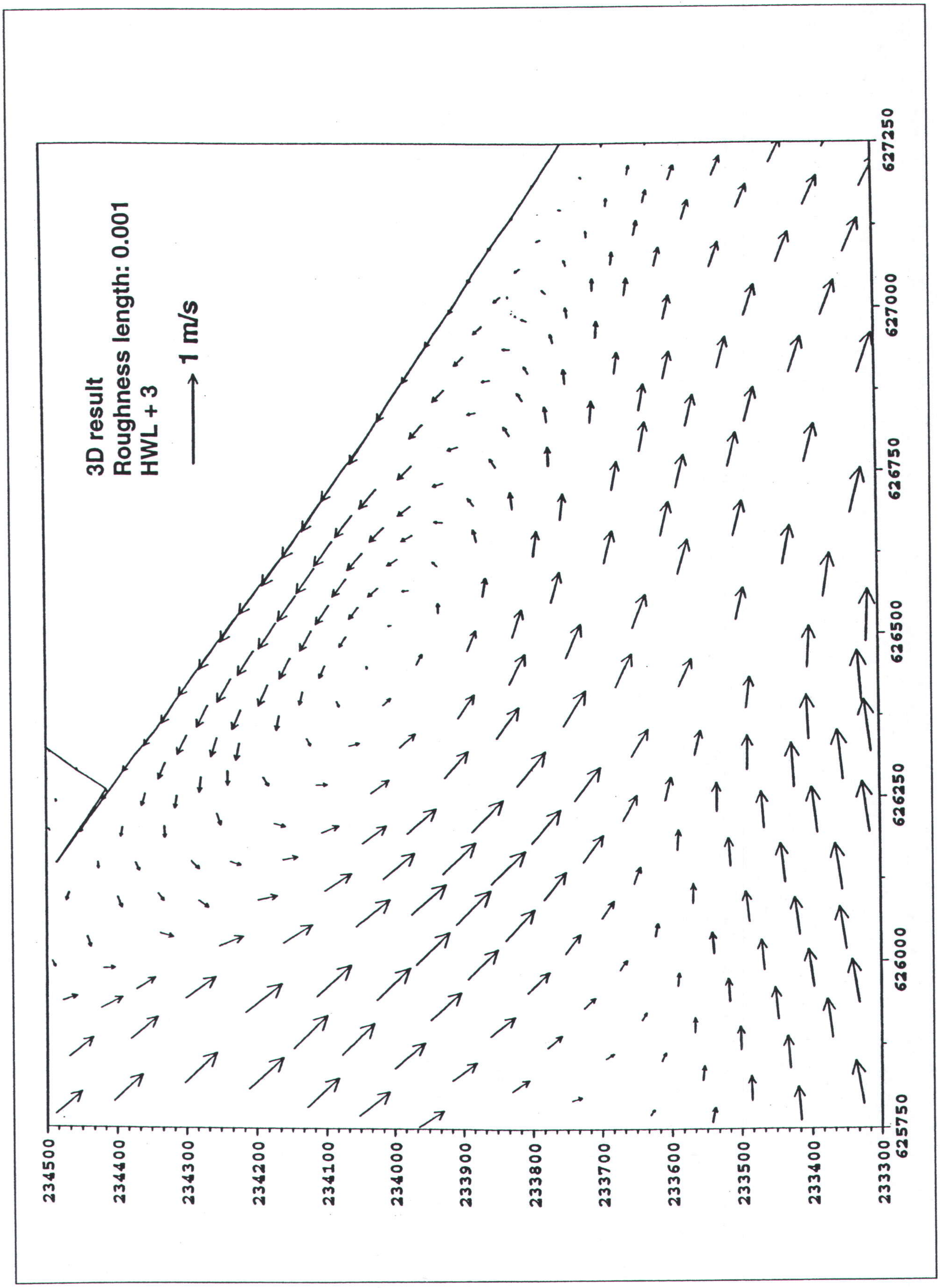

Figure 5.7 **3D model. Roughness length=0.001 (HWL+3)**

Appendix

APPENDIX Description of the numerical models

As explained in Chapter 2, the modelling of flows at structures is carried out by the use of separate models for the flow and wave processes. The details of radiation stress, viscosity and bed stress formulation may be carried through from the wave model to the flow model, in order to simulate the wave-averaged flows.

Flow models

The models TELEMAC and TIDEFLOW were used for flow simulations. These are state-of-the-art models, of which HR Wallingford have long experience and access to the source codes to be able to make amendments.

TELEMAC is a model that is used worldwide and is based on solving the shallow water equations using the finite element method with an unstructured mesh made up of triangles. The finite element method is clearly very useful to obtain a good representation of the boundaries of the domain. TELEMAC was developed by EDF (Paris). Within TELEMAC-2D and TELEMAC-3D it is possible to use different formulations for the turbulence:

- specified eddy-viscosity
- mixing-length model
- k-ε model

as described above in section 2.6.

The TIDEFLOW model also solves the shallow water equations in two dimensions and uses a regular finite difference grid. TIDEFLOW was developed at HR Wallingford and is part of the TIDEWAY suite of modelling software.

For the user the greatest difference between using TIDEFLOW and TELEMAC is that TELEMAC has the advantage of using a very flexible unstructured grid of triangles that allows variable resolution according to the needs of the user and can accurately represent features such as coastlines, channels and structures. TIDEFLOW, however, may be quicker to use as there is no need to have a mesh-generation phase in the model study, the model simply uses a grid made of rectangles and only the orientation, number of cells in each direction and grid size need to be specified by the user.

Wave models

The ARTEMIS code (Agitation and Refraction with TElemac on a Mild Slope) solves the elliptic mild slope equation using finite element techniques inside the TELEMAC modelling system structure. ARTEMIS is a model that solves the mild slope equation with wave breaking included. Most of the known phenomena of wave dynamics are taken into account in the present version of ARTEMIS except wave refraction by current.

FDWAVE (used in the PISCES morphodynamic modelling system) uses a time-independent finite difference marching technique to calculate the wave field along successive rows until the row nearest to the shore is reached. The output quantities are the root-mean-square wave height, significant wave period and mean wave direction at each grid intersection point. The model does not usually require a large number of elements per wavelength, but it also does not accurately model the diffraction process or supply information on the phase of the wave.

A.1 TELEMAC-2D

TELEMAC-2D is a finite element modelling system for flows, waves and other hydraulic processes. The flow models, TELEMAC-2D and TELEMAC-3D are based on the solution of the Navier-Stokes equations under conditions when a hydrostatic pressure approximation can be made (wavelength should exceed 20 times the water depth).

In deriving the following equations the Boussinesq approximation (density variation is ignored except for the buoyancy term) is made in addition to the hydrostatic pressure hypothesis:

Continuity equation:

$$\frac{\partial u}{\partial x}+\frac{\partial v}{\partial y}+\frac{\partial w}{\partial z}=0 \qquad [39]$$

hydrostatic pressure assumption (neglect of vertical accelerations compared with gravity):

$$p = p_{atm} + \rho_0 g(Z_s - z) + \rho_0 g \int_z^{Z_s} \frac{\Delta\rho}{\rho_0} dz'$$

Momentum equations:

$$\frac{\partial u}{\partial t}+u\frac{\partial u}{\partial x}+v\frac{\partial u}{\partial y}+w\frac{\partial u}{\partial z}=-\frac{1}{\rho}\frac{\partial p}{\partial x}+\frac{\partial}{\partial x}\left(\upsilon_H\frac{\partial u}{\partial x}\right)+\frac{\partial}{\partial y}\left(\upsilon_H\frac{\partial u}{\partial y}\right)+\frac{\partial}{\partial z}\left(\upsilon_Z\frac{\partial u}{\partial z}\right)+F_X \qquad [40]$$

$$\frac{\partial v}{\partial t}+u\frac{\partial v}{\partial x}+v\frac{\partial v}{\partial y}+w\frac{\partial v}{\partial z}=-\frac{1}{\rho}\frac{\partial p}{\partial y}+\frac{\partial}{\partial x}\left(\upsilon_H\frac{\partial v}{\partial x}\right)+\frac{\partial}{\partial y}\left(\upsilon_H\frac{\partial v}{\partial y}\right)+\frac{\partial}{\partial z}\left(\upsilon_Z\frac{\partial v}{\partial z}\right)+F_Y \qquad [41]$$

The depth-integrated equations (which are solved in TELEMAC-2D) then become:

$$\frac{\partial h}{\partial t}+\frac{\partial \bar{u}h}{\partial x}+\frac{\partial \bar{v}h}{\partial y}=0 \qquad [42]$$

$$\frac{\partial \bar{u}}{\partial x}=-g\frac{\partial Z_S}{\partial x}+\bar{F}_X+\bar{S}_X \qquad [43]$$

$$\frac{\partial \bar{v}}{\partial y}=-g\frac{\partial Z_S}{\partial y}+\bar{F}_Y+\bar{S}_Y \qquad [44]$$

with:

$$\bar{F}_x=\frac{1}{(Z_s-Z_f)}\int_{Z_f}^{Z_s}\left[-\frac{1}{\rho_0}\left(1-\frac{\Delta\rho}{\rho_0}\right)\frac{\partial p_{atm}}{\partial x}+g\frac{\Delta\rho}{\rho_0}\frac{\partial Z_S}{\partial x}-g\frac{\partial}{\partial x}\left(\int_Z^{Z_s}\frac{\Delta\rho}{\rho_0}dz'\right)\right]dz$$

and

$$\overline{F}_x = \frac{1}{(Z_s - Z_f)} \int_{Z_f}^{Z_s} \left[-\frac{1}{\rho_0} \left(1 - \frac{\Delta\rho}{\rho_0} \right) \frac{\partial p_{atm}}{\partial y} + g \frac{\Delta\rho}{\rho_0} \frac{\partial Z_S}{\partial y} - g \frac{\partial}{\partial y} \left(\int_{z}^{Z_s} \frac{\Delta\rho}{\rho_0} dz' \right) \right] dz$$

where:
x,y,z: co-ordinates
u, v, w: velocity
g: gravity
p: pressure
ρ_0: reference density
$\Delta\rho$: variation in density
h: depth
$\overline{u}, \overline{v}$: depth-averaged velocity
ν_H, ν_Z: velocity diffusion coefficients
Z_S: the free surface elevation
Z_f: the bed elevation
$\overline{S_X}, \overline{S_Y}$: are additional terms such as Coriolis, wind or radiation stress contribution
F_X, F_Y: source terms
$\overline{F}_X, \overline{F}_Y$: depth-averaged buoyancy terms

TELEMAC-2D makes use of an unstructured mesh comprising triangular elements. The mesh in TELEMAC-3D is built on the basis of the TELEMAC-2D mesh by dividing the water height into a specified number of layers. At each of these layers, the same mesh used in the 2D model is applied, which finally leads to a three-dimensional mesh comprising prismatic elements. TELEMAC-3D solves the depth-integrated equations (2D) to determine the depth-averaged values of the unknowns. Then, knowing the water depth, TELEMAC-3D splits the volume in the required number of and uses the finite element method applied to the prismatic 3D elements.

At the boundary:

Two cases are to be distinguished. The first condition is always true for a solid boundary and the others are true alternatively for the velocities.

-Impermeability can be represented by: $\vec{u}.\vec{n} = 0$.

-The slip condition, which is normally written $\frac{\partial(\vec{u}.\vec{t})}{\partial n} = 0$ for all vectors of the tangent plane to the wall, and which is rewritten in TELEMAC as $\frac{\partial u}{\partial n} = \frac{\partial v}{\partial n} = 0$.

-Friction that is written: $\frac{\partial \vec{u}.\vec{t}}{\partial n} = \alpha \vec{u}.\vec{t}$

$\vec{u}$: velocity vector
$\vec{t}$: vector tangential to the wall
$\vec{n}$: vector normal to the wall
α: coefficient given by the turbulence model

The second type of boundary corresponds to the case where the user has to deal with an open boundary. In practise, the flow rate is known and the distribution of the velocity is not. The free surface height may also be imposed at a boundary.

A.2 ARTEMIS

The ARTEMIS computational model (Agitation and **R**efraction with **TE**lemac on a **MI**ld Slope) was also developed by the National Hydraulics Laboratory, (Laboratoire National d'Hydraulique, Paris) of the Research and Development Division of the French Electricity Board (EDF-DER). It is one of the modelling programs included in the TELEMAC modelling suite. Like TELEMAC, the resolution of the equation is based on the finite element method.

The latest version of ARTEMIS was developed in order to include breaking and dissipation. It solves the mild slope equation extended based on the work of Booij (1981):

$$\nabla\left(CC_g\nabla\varphi\right)+CC_g\left(k^2+i\mu k\right)\varphi=0 \qquad [45]$$

where:
- φ is the complex velocity potential
- μ is an initially unknown dissipation coefficient
- k is the wave number
- C is the wave celerity
- C_g is the group celerity

Therefore, ARTEMIS is able to model reflection, refraction, breaking, diffraction of linear waves propagating in an area with a slow varying bed in any case where the non-linear terms can be neglected. ARTEMIS calculates at each node of the mesh the velocity potential and determines afterwards all the physical variables: wave field, wave height, and direction of propagation and phase of the potential. Two options are given to define the characteristics of the incident wave. The user can choose to solve the equation either for random waves or for monochromatic waves.

Boundary conditions

Three kinds of boundary can be imposed in ARTEMIS.

- The first one considers the case of the solid boundaries, which physically means that the waves are propagating towards a wall (dykes, groyne, breakwater...) that can be more or less reflective. In front of the wall, there will be superposition of the incident and reflected waves. The wall might also induce a change in phase and a loss of amplitude (due to loss of energy at the wall) between the incident and the reflected waves. The reflection coefficient $Re^{i\alpha}$ is introduced to reproduce this phenomenon. If this coefficient is complex then we have loss of amplitude and change in the phase. In this case, the condition that has to be imposed can be written as:

$$\vec{u}_{ref}.\vec{n}=-Re^{i\alpha}\vec{u}_{inc}.\vec{n}$$
$$\xi_{ref}=Re^{i\alpha}\xi_{inc}$$
$$\varphi=\varphi_{inc}+\varphi_{ref}$$

which can be rewritten:

$$\frac{\partial\varphi_{ref}}{\partial n}=-Re^{i\alpha}\frac{\partial\varphi_{inc}}{\partial n}$$
$$\varphi_{ref}=Re^{i\alpha}\varphi_{inc}$$

And eventually, using the approximation of progressive waves:

$$\frac{\partial \varphi}{\partial n} - i\frac{1-Re^{i\alpha}}{1+Re^{i\alpha}}k.\cos(\theta)\varphi = 0$$

where θ is the angle between the wave direction and the normal, n, at the wall.
The symbols $_{ref}$ and $_{inc}$ represent reflection and incidence
-The second one is related to an opening on offshore or to another basin where the waves can come and go which corresponds to the case of liquid boundary. In an open boundary, the model has to take into account both the waves going out of the domain and the waves coming in. This is solved by assuming that the potential is the superposition of an incident potential γ that is known at the boundary and of the potential due to the waves reflected out of the domain: ϕ_p.

$$\varphi = \gamma + \varphi_P$$

This can be written as follows: $\frac{\partial \varphi}{\partial n} - ik\varphi\cos\theta = \frac{\partial \gamma}{\partial n} - ik\gamma\cos\theta$

In the special case where the waves can exit the domain freely, the boundary condition will be derived from the previous equation by simply setting γ to zero,
which yields:

$$\frac{\partial \varphi}{\partial n} - ik\varphi\cos(\theta) = 0$$

Another condition on the potential can be set at the boundary. This simply consists of setting the potential to a constant. This condition is not really useful though.

Methodology of resolution

In contrast to the early versions of ARTEMIS, the latest version, which was used for this project, includes the effects of dissipation due to breaking and/or due to bed friction. A dissipation coefficient was introduced in the original mild slope equation in order to do this.

In the case of monochromatic waves, the dissipation can be calculated using either Dally's formula or Battjes and Janssen equation. (see section 2.3.3)

The dissipation can be written as: $D = \frac{1}{8}\rho g C_g H^2 \mu$

With:

in the first case $\mu = \frac{K}{h}\left[1 - \left(\frac{\Gamma h}{H}\right)^2\right]$

and in the second case, $\mu = 2f\frac{H}{hC_g}$

As μ is dependent on the wave height, and thus on the potential, the extended mild slope equation that has to be solved is a non-linear one. This kind of equation is solved by using an iterative method. This method requires an initial guess for μ to get the resolution started.

The method is outlined in the figure below:

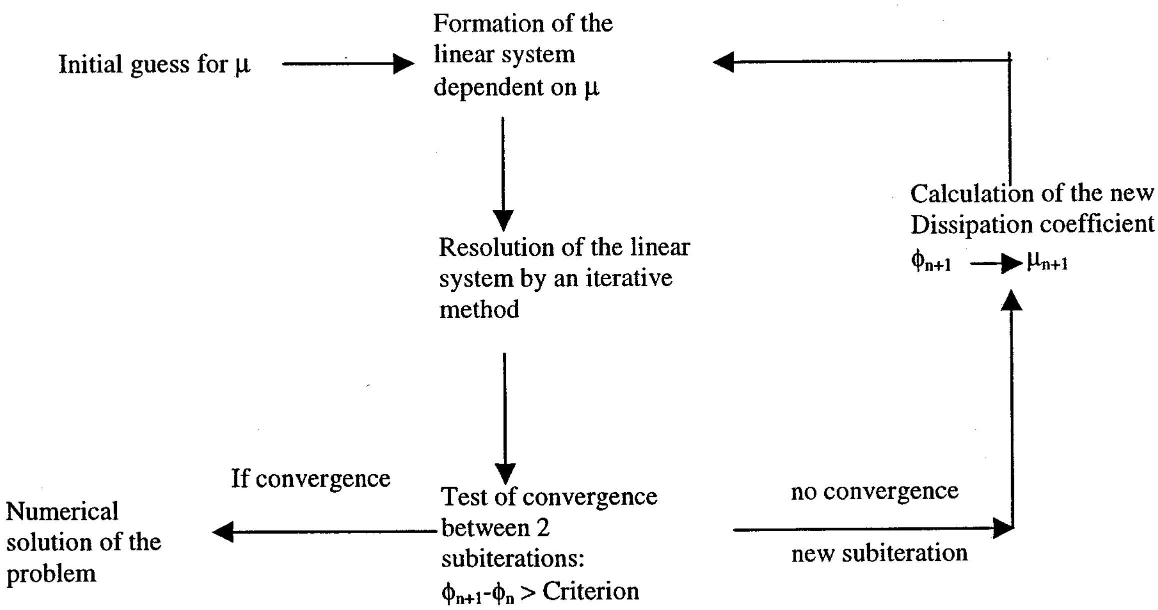

A.3 PISCES (FDWAVE and TIDEFLOW)

PISCES is a 2D depth-integrated model combining a flow module and a wave module to calculate the sediment transport field and then, when run in morphological mode, to update the bathymetry. The use of this type of model in morphological mode for coastal applications is still very much in its infancy, and gives rise to a number of opportunities for developmental research. One such opportunity is the application to beach control structures such as groynes and detached breakwaters, even though PISCES has previously been used to model the combined effect of waves and tides. PISCES was developed by HR Wallingford in 1993.

The framework of PISCES has been developed on the architecture of the HR TIDEWAY modelling suite, an integrated package designed for tidal current modelling and tidal process modelling. Each module can be run as a stand-alone sub-model. For example, a wave propagation and wave-induced currents analysis for a schematic area has been carried out without the need to consider the morphodynamic module of the model.

The overall package is 2D in plan, based on regular gridded geometry, and for each module the numerical solution is obtained by finite difference methods.

Output from the model is in the form of data files referring to each particular element of the model, comprising wave, current and sediment transport fields, and updated bathymetry. The morphodynamic time stepping information is also stored as a means of assessing the development in time of the seabed bathymetry.

The hydrodynamic module of PISCES contains wave propagation equation solver sub-modules, linking the elevation field from the currents sub-module to the waves sub-modules, and radiation stress and wave orbital velocity field from the waves to the current module.

Tidal motion is simulated by explicitly defining a time history of water levels and/or flow velocities at the appropriate boundaries (for large area models it is possible to drive the tidal model with elevation boundaries alone). Wave-driven currents are calculated at each interior model cell by inclusion of wave radiation stresses and orbital velocities in the horizontal momentum equations, and also by estimating the appropriate wave-driven current and water level set-up at the model velocity and elevation boundaries respectively. Combined wave-plus-tidal motion is simulated by combining the contributions from waves and tides at the boundaries.

For general application of the model, the wave fields are passed to the current module, which integrates forward in time for one storage interval of the boundary file (typically 10-15 minutes), linearly interpolating between the boundary values. The elevation field is then passed back to the wave module and the wave fields are re-determined. In this way, the wave fields will be calculated at the true water depths, and if the required offshore wave input conditions change through the tide, this can also be taken into account. The horizontal velocity and elevation fields are typically stored at the same storage interval for later post-processing if required.

The wave module was developed separately from the TIDEWAY format and therefore an interface was required to automatically link the current and wave modules. The wave module determines the transformation of surface waves incorporating the combined effects of refraction and diffraction, and dissipation by bottom friction and breaking. Random wave spectra and current refraction are also included.

The wave module is based on steady-state conditions, and the normal mode of operation is to run for a specific stage of the tide at a particular plane water level. This module was amended for PISCES by the inclusion of the water elevation field from the current module. This factor becomes important in shallow coastal areas where wave set-up and tidal pressure set-up become significant, and the water surface is no longer level. This amendment to the module results in a more accurate representation of the wave-induced current-driving forces.

The computational wave transformation model uses a time-independent finite-difference marching technique. The method is computationally quicker than most alternative refraction-diffraction methods, with the possibility of further increasing computational speed by the ability to use coarser grid sizes. However the absence of the diffraction process from the model means that applications in the presence of surface-piercing structures need to be carried out with extra care.

The model was first designed for wave propagation in the open sea, rather than where structures are present. However, later validations of the model showed it was also possible to achieve a reasonable prediction of the wave field near structures such as offshore breakwaters (Pechon et al, 1996). Wave directions are limited to a certain ranges either side of the forward grid direction, usually about 40° from this forward grid direction, but it depends on the grid being used.

The model is based upon a theoretical approach originally put forward by Battjes and extended by Yoo and O'Connor. The FDWAVE model uses the same theoretical basis as Yoo and O'Connor but adopts a different numerical modelling approach (Yoo and O'Connor used a time-dependent formulation, which can require a considerable number of time steps to reach the steady state).

The sea area under study is represented by a grid composed by rectangular or square elements. The positive y direction is chosen to be in the main propagation direction of the waves (roughly perpendicular to the coastline). The method of solution uses a row-by-row marching technique with a predictor and corrector calculation at each row. The input values of wave height, period and direction are specified at each grid element on the offshore row. The finite-difference representation of the governing equations is then used to make a calculation of these parameters on the second row. This is the predictor step. Using these values, a more accurate estimate of the y-derivatives can be made, and the calculation of parameters on row to row is repeated with these 'corrected' y-derivatives. This corrector step can, in principle, be repeated an indefinite number of times, but in most cases one calculation is found to be sufficient. The whole predictor-corrector process is then repeated for row three, and the process continues until the last row, furthest inshore, is reached.

The appropriate equations for studying water movements in tidal areas are the shallow water equations in a very similar form to those represented above for the TELEMAC system. The equations are obtained by vertically integrating the equations of motion governing mass and momentum and making the following simplifying assumptions:

(i) the flow is incompressible;
(ii) it is well mixed (no variations in density);
(iii) vertical accelerations are negligible;
(iv) the effective lateral stresses associated mainly with shearing in the horizontal, and to a small extent with the averaging of sub-grid scale turbulence, may be approximated by a constant eddy viscosity;
(v) bed stress can be modelled using a quadratic friction law.

The equations then take the following form:

<u>Conservation of mass</u>:

$$\frac{\partial z}{\partial t}+\frac{\partial}{\partial x}(ud)+\frac{\partial}{\partial y}(vd)=0$$

Conservation of momentum:

$$\frac{\partial u}{\partial t}+u\frac{\partial u}{\partial x}+v\frac{\partial u}{\partial y}=-g\frac{\partial z}{\partial x}-\frac{\tau_{bx}}{\rho d}+D\left[\frac{\partial^2 u}{\partial x^2}+\frac{\partial^2 u}{\partial y^2}\right]+\Omega v+\frac{\tau_{wx}}{\rho d} \qquad [46]$$

$$\frac{\partial v}{\partial t}+u\frac{\partial v}{\partial x}+v\frac{\partial v}{\partial y}=-g\frac{\partial z}{\partial y}-\frac{\tau_{by}}{\rho d}+D\left[\frac{\partial^2 v}{\partial x^2}+\frac{\partial^2 v}{\partial y^2}\right]-\Omega u+\frac{\tau_{wy}}{\rho d} \qquad [47]$$

where:

z= elevation above datum (m)
u= depth-averaged component of velocity in x direction (positive eastwards) (m/s)
v= depth-averaged component of velocity in y direction (positive northwards) (m/s)
d= total depth, (z+h), where h is the depth below datum (m)
f= friction coefficient
D= horizontal eddy viscosity coefficient (m^2/s)
Ω= Coriolis parameter (s^{-1}) which is derived from the latitude specified when setting up the model
τ_{wx}= component of wind stress and/or wave radiation stress in the x direction(N/m^2)
τ_{wy}= component of wind stress and/or wave radiation stress in the y direction(N/m^2)
τ_{bx} = bed shear stress components in the x direction (N/m^2)
τ_{by} = bed shear stress components in the y direction (N/m^2)
ρ = density of fluid (kg/m^3)

Estimation of the wave-driven currents at the model lateral boundaries was previously made via a reduction of the appropriate momentum equation, assuming longshore uniformity, negligible cross-shore flow and viscous effects. However, using this approach, an adjustment to the flows near boundaries was observed, giving rise to associated bed level changes.

It was found necessary to include the viscous effects (diffusion terms, D), and this development resulted in homogeneous flows along streamlines near the boundaries with no apparent adjustment. The method is described as follows. Consider an anti-clockwise co-ordinate system with x-axis normal to the coast. The assumptions of steady flow, longshore uniformity and negligible cross-shore mean flow (ignoring Coriolis effects) reduce (1) and (2) to:

$$0=-g\frac{\partial z}{\partial x}+\frac{\tau_{wx}}{\rho d} \qquad [48]$$

$$0=-g\frac{\partial z}{\partial y}+D\left[\frac{\partial^2 v}{\partial x^2}\right]+\frac{\tau_{wy}}{\rho d} \qquad [49]$$

Equation (48) is solved to define the cross-shore mean water level set-up z (by assuming zero set-up offshore). Equation (49) is solved numerically to define the longshore wave-driven current, using a Newton method. Solution to (49) to an acceptable accuracy is very fast, requiring of the order of 10 iterations starting from an initial estimate of v based on the analytical solution to (4) without the diffusion term.

For FDWAVE, an interface has to specify what is the offshore line, for this module has its own grid and origin.